Design and Development of a Regeneratively Cooled N_2O/C_2H_6 Thruster

A Modular Approach to Design of Small-Scale Thrusters

Timo Kramer

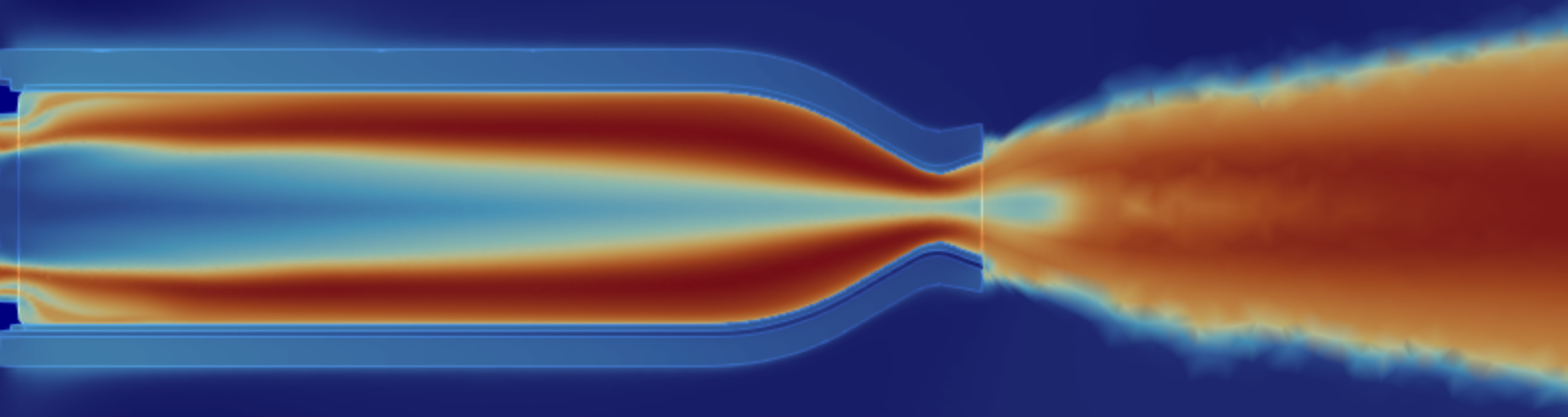

TU Delft

Design and Development of a Regeneratively Cooled N_2O/C_2H_6 Thruster

A Modular Approach to Design of Small-Scale Thrusters

by

Timo Kramer

to obtain the degree of Master of Science
at the Delft University of Technology,
to be defended publicly on Friday, April 15, 2026 at 14:00 PM.

Student number:	5038944	
Project duration:	July 17, 2025 – April 15, 2026	
Thesis committee:	A. Cervone PhD,	TU Delft, supervisor
	F. De Domenico PhD,	TU Delft
	C. Falsetti PhD,	TU Delft
	Ir. F. Valencia Bel,	European Space Agency

An electronic version of this thesis is available at http://repository.tudelft.nl/.

TU Delft

Abstract

In the last few decades, developments within the space industry have led to faster iterations in the design process of space products, where the emphasis has been laid on testing rapidly, rather than perfecting a design first. Especially with thrusters, where the complex combustion and gas dynamics cannot be perfectly simulated, rigorous testing is necessary in order to obtain a good design. Building on this method of engineering, certain components of a thruster need to be changed in order to accommodate for this. One critical component is the propellant. Where previously the objective was selecting a cheap, high performing propellant, a shift has occurred where now, safety, sustainability and reduced complexity are the most critical aspects. In this thesis, together with the European Space Agency (ESA), a new thruster has been developed using nitrous-oxide and ethane as its propellants. Since both propellants are non-toxic, self-pressurizing and easily obtainable, they make for ideal candidates in the NewSpace economy.

Using rocket engine theory, a modular 20 N regeneratively cooled thruster has been developed. CFD and FEM simulations indicate that the thruster is capable of firing in steady-state mode without failure, however physical verification still has to take place in order to fully verify the thruster. In order to demonstrate the modularity of the thruster, three configurations have been developed. While the design of the thrust chamber has been kept constant, the injector and igniter are different across the configurations. At atmospheric conditions, based on numerical analysis, the thruster has a specific impulse of 160 s. For the material of the thruster wall, a recently developed additive manufacturing nickel alloy called ABD900AM is used. Together with seventeen cooling channels of 0.5 mm width and 0.5 mm height, a maximum inner wall temperature of 936 K is reached, well below the temperature after which the properties of ABD900AM start to degrade. Using FEM analysis, a safety factor with respect to the yield strength of 1.5 was found as the lowest value in the thrust chamber. At the corners of the fixed flange to which the thrust chamber was attached, a value of 1.0 was found.

As solely verifying the thruster via computational analysis is not sufficient, a verification plan in line with ECSS guidelines was written. This verification plan lays out the tests that need to be performed in order to fully verify and validate the thruster. It includes tests such as cold flows, actuation tests and hot-fires. These tests have not been performed in this thesis due to time constraints, but will be performed in the future by the European Space Agency. Furthermore, the initial steps of the manufacturing process have also been performed. The CAD models have been developed and are shown in this thesis, as well as the associated technical drawings. Next to that, iterations have been made during the thesis based on feedback given by machinists at ESA as well as external suppliers and manufacturers.

Preface

After finishing my internship at D-Orbit, I was sure I wanted to do my thesis on a topic related to space propulsion. Unfortunately, in the Netherlands the space propulsion industry is very limited. However, I got lucky, and after contacting Olga Motsyk from the European Space Agency, she told me they had a thesis opportunity that was right up my street. So, first of all, I want to thank her and also her colleague Ferran Valencia Bel for giving me the opportunity to do my thesis with the European Space Agency. Furthermore, I would also like to thank them for their bi-weekly feedback and extensive guidance through this project.

Secondly, I would like to thank Angelo Cervone for his patience and great assistance as my supervisor of this thesis, giving me very valuable feedback when it was necessary.

Thirdly, I would like to thank my family and friends who have supported me through the entire thesis, helping me physically, mentally as well as financially.

Last but definitely not least, I would like to thank my amazing girlfriend who took (and takes!) care of me every day, in both the relaxing and stressful moments. Without her, this would all have been a much longer and exhausting period.

Timo Kramer
Delft, March 2026

Contents

Nomenclature

Abbreviations

AM	Additive Manufacturing
CAD	Computer-Aided Design
CEA	Chemical Equilibrium with Applications
CFD	Computational Fluid Dynamics
ECSS	European Cooperation for Space Standardization
ESA	European Space Agency
ESTEC	European Space Research and Technology Centre
FEA	Finite Element Analysis
FEM	Finite Element Method
HTP	High-Test Peroxide
LOX	Liquid Oxygen
MEOP	Maximum Expected Operating Pressure
MIB	Minimum Impulse Bit
MMH	Monomethylhydrazine
NASA	National Aeronautics and Space Administration
NLR	Netherlands Aerospace Centre
NTO	Nitrogen Tetroxide
O/F	Oxidizer-to-Fuel Ratio
PPE	Personal Protective Equipment
RCS	Reaction Control System
RPA	Rocket Propulsion Analysis
TBD	To Be Determined
TRL	Technology Readiness Level
VCM	Verification Control Matrix

Greek Symbols

α	Thermal expansion coefficient / Absorptivity [K^{-1}]
Δ	Difference / Change [-]
ϵ_c	Contraction ratio [-]
η	Efficiency [-]
Γ	Vandenkerckhove function [-]
γ	Specific heat ratio [-]
λ	Thermal conductivity (fluid) [$W{\cdot}m^{-1}{\cdot}K^{-1}$]
λ_e	Velocity coefficient at nozzle exit [-]
μ	Dynamic viscosity [Pa·s]
ϕ	Angle (Contraction/Expansion) [deg]
ρ	Density [kg/m^3]
θ_e	Nozzle exit half-angle [deg]
ξ_r	Reaction efficiency loss factor [-]
ζ_d	Nozzle efficiency [-]
ζ_r	Reaction efficiency [-]

Latin Symbols

$\dot{m}$	Mass flow rate [kg/s]
A	Area [m^2]
a	Thermal expansion coefficient / Empirical constant [K^{-1} or -]
A_e	Nozzle exit area [m^2]
A_t	Nozzle throat area [m^2]
c^*	Characteristic velocity [m/s]
C_D	Discharge coefficient [-]
C_F	Thrust coefficient [-]
C_p	Specific heat capacity at constant pressure [$J{\cdot}kg^{-1}{\cdot}K^{-1}$]
D	Diameter [m]
E	Modulus of elasticity [Pa]
F	Thrust force [N]
g_0	Standard gravity acceleration [m/s^2]
h	Specific enthalpy [J/kg]
H_c	Cooling channel height [m]
h_{coeff}	Heat transfer coefficient [$W{\cdot}m^{-2}{\cdot}K^{-1}$]
I_{sp}	Specific impulse [s]

K	Head-loss coefficient [-]
k	Thermal conductivity [W·m^{-1}·K^{-1}]
L^*	Characteristic chamber length [m]
L_{cyl}	Cylindrical chamber length [m]
M	Mach number [-]
M_A	Bending moment per unit length [N·mm^{-1}]
N	Number of channels / orifices [-]
Nu	Nusselt number [-]
P	Pressure [Pa or bar]
Pr	Prandtl number [-]
q	Heat flux [W/m^2]
R	Specific gas constant [J·kg^{-1}·K^{-1}]
r	Radius [m]
R_A	Universal gas constant [J·mol^{-1}·K^{-1}]
R_n	Nozzle radius / Throat curvature radius [m]
Re	Reynolds number [-]
S_c	Critical buckling stress [Pa]
S_l	Longitudinal (thermal) stress [Pa]
S_t	Tangential (hoop) stress [Pa]
T	Temperature [K]
t	Wall thickness [m]
U	Velocity (flow) [m/s]
v	Velocity (fluid) [m/s]
V_{cc}	Combustion chamber volume [m^3]
w_c	Cooling channel width [m]
x	Characteristic dimension [m]

Subscripts

*	Critical / Throat conditions
amb	Ambient conditions
co	Coolant
cr	Critical (thermodynamic point)
c	Combustion chamber
eq	Equivalent
e	Exit plane
f	Fuel (C_2H_6)
g	Gas / Combustion gas
inj	Injector
in	Inlet
opt	Optimum expansion
ox	Oxidizer (N_2O)
$stag$	Stagnation conditions
$stat$	Static conditions
tot	Total
t	Throat
vac	Vacuum conditions
$wall$	Wall

List of Figures

List of Tables

1 Introduction

100 years ago, the first (liquid-fuelled) rocket was launched by Robert H. Goddard on the 16th of March 1926 (Michael Neufeld, 2016). While it was just a very simple rocket, reaching an altitude of only 12.5 m, it already was using liquid oxygen, an oxidizer that is arguably still the most popular oxidizer in rocketry today. However, liquid oxygen does bring its challenges related to storage, feed system design and (safe) handling. Especially for rockets with military applications, the problems and delays associated with liquid oxygen could be a serious drawback.

During World War II, experiments were performed with other propellants and one of these propellants was called "C-Stoff" developed by the Germans (Clark, 2018). This propellant consisted of methanol, hydrazine-hydrate, water and a catalyst, and was highly toxic to humans, however it was hypergolic with high-test peroxide (HTP), making it an ideal candidate for rockets with a military purpose. In the years after the war, this propellant combination (or other combinations including hydrazine) were more and more used in satellite applications due to its good long-term storability.

However, in more recent years with the upcoming NewSpace industry and the high rate of new in-space propulsion development, different commercial companies and institutions have sought alternatives for these propellants that would make testing and propellant loading safer. In this thesis, an engine has been developed using nitrous-oxide as its oxidizer, and ethane as the fuel. Both of these propellants are non-toxic to humans, have self-pressurizing properties, and can be stored at room temperature. However, despite these benefits, not much public research is available on nitrous based bi-propellant thrusters, if you compare it to research on "conventional" propellants like liquid oxygen, RP-1 and hydrazine (Grubelich and Lindblom, 2013). This makes it a strong candidate for a master thesis.

Figure 1.1: Dawn Aerospace B20 N_2O/C_3H_6 Thruster (Dawn Aerospace, 2025)

Current developments in the space industry show a clear shift to so-called 'green' propellants (Gohardani et al., 2014). A big advantage of these propellants is that they are non-toxic and easy to handle. Furthermore, these propellants provide benefits when testing engines, as they are easily storable for a longer duration at room temperature. This means that they drastically reduce the safety risks compared to propellants like hydrazine and also have other beneficial properties like self-pressurization (Zakirov et al., 2000). As of now, already much research has been performed on these types of propellants. However, certain combinations have not yet been extensively explored, or when they have been explored, not many details regarding the design have been released to the public, as is often the case with innovative R&D within commercial aerospace companies. The goal of this master thesis is to perform the design of a modular 20 N bi-propellant thruster which uses nitrous oxide (N_2O) as the oxidizer and ethane as the fuel. This thruster will then be used by the European Space Agency (ESA) in their new chemical propulsion facility to use as a testing platform, testing different types of fuel, injectors, and igniters.

As said before, one of nitrous-oxide's main benefits is that it's self-pressurizing. This essentially means that the propellant is in a saturated state, where it is both partially in gaseous state and liquid state. For nitrous-oxide, this saturated state at room temperature (20 °C) makes the pressure inside the tank around 52.4 bar (Zakirov et al., 2001).

In the following chapters, the entire design and development process will be shown for three thruster configurations with varying igniter, injector, and manifold. Firstly, in chapter 2 the relevant literature as well as existing thruster

designs will be discussed. Without considering trade-offs, each component of the thruster will be examined, presenting the available options and reviewing past approaches. After exploring the background, chapter 3 presents the stakeholder, design, and verification requirements for the project. Subsequently, in chapter 4 the actual design process will be shown, including trade-offs, software used and the reasoning behind the design configurations. Building on the design methodology, in chapter 5, the complete plan will be shown on how the thruster will be verified, both using analytical and physical testing methods. This includes CFD, FEM and tests performed in the new propulsion lab that is being developed by ESA. For this, a verification plan was made in order to verify the performance, functionality and structural integrity based on European Cooperation for Space Standardization (ECSS) guidelines. Next, in chapter 6, the results of both the design process and the (analytical) verification process will be shown and discussed. Here, the emphasis will be on showing that the simulated thruster performance agrees with the design performance, and that the temperatures within the thruster are minimized, leading to a good structural integrity. Finally, in chapter 7 the thesis will be concluded and recommendations will be given for future research and development of this thruster.

2
Theoretical Background and Current State-of-the-art

In space, small (chemical) thrusters are generally used for controlling the orientation of a spacecraft, but can also be used for changing an orbit, or even interplanetary travel. In 1957, Russia launched the first ever satellite, the Sputnik 1. This satellite did not have any attitude control system, and thus tumbled around freely in orbit. They repeated this with the Sputnik 2, but in the Sputnik 3 they designed a so-called reaction control system (RCS) using cold gas thrusters, such that they could control the spacecraft (Russian Space Web, 2012). However, while effective and rather non-complex, cold gas thrusters are not a very efficient way to achieve a force. This is because in a rocket engine most of the energy comes from combustion, which is not present in a cold gas thruster. In 1959, NASA introduced a different solution. Similar to the Russian approach, a single propellant was used; however, instead of being expelled directly, the propellant was ignited, allowing the energy released during ignition and decomposition to produce a higher efficiency (NASA, 2024). This is what's called a monopropellant. However, while monopropellant systems are still widely used today, there is another system which is more complex, but achieves an even higher efficiency. This is called a bi-propellant thruster. Bi-propellant thrusters are a more complex but highly efficient alternative to monopropellant systems. They use a precise mixture of a fuel and an oxidizer to generate thrust. Bi-propellant thrusters are used in heavy launch vehicles such as the Merlin thrusters on the Falcon-9 launch vehicles of SpaceX (SpaceX, 2025), but also smaller thrusters such as the B20 thruster from Dawn Aerospace as was shown before in Figure 1.1.

2.1. Propellants

This thesis will focus on a bi-propellant thruster, utilizing nitrous oxide as the oxidizer and ethane as the fuel. Current research into nitrous oxide propulsion largely concentrates on its use in small space thrusters, which typically produce between 1 N to 200 N of thrust (Gohardani et al., 2014). However, there is also extensive research being done related to hybrid propulsion, such as the HyNOx utilizing a mixture of nitrous oxide and hydrocarbons. While this thesis will focus on the usage of nitrous oxide and ethane in a bi-propellant non-premixed configuration, using a premixed mixture as a monopropellant has been shown to offer almost identical performance (Janzer et al., 2022). However, this configuration results in high combustion temperatures (3400 K); furthermore, employing a premixed propellant in an engine can result in flashback, where the flame propagates back into the injector or feed lines.

Nitrous oxide presents many advantages when it is used as a propellant for a small space propulsion thruster. It is non-toxic, colorless, non-corrosive, and it can be used with most common materials. It decomposes around 520 °C into oxygen and nitrogen, which makes it also a good option for a monopropellant thruster. Nitrous oxide can be stored as a liquid and has a vapour pressure of 52 bar at 20 °C, as can be seen in Figure 2.1. When compared to hydrogen peroxide (H_2O_2) and hydrazine (N_2H_4) as a monopropellant (Zakirov et al., 2001), nitrous oxide has a specific impulse of 206 s, hydrogen peroxide 179 s and hydrazine 245 s.

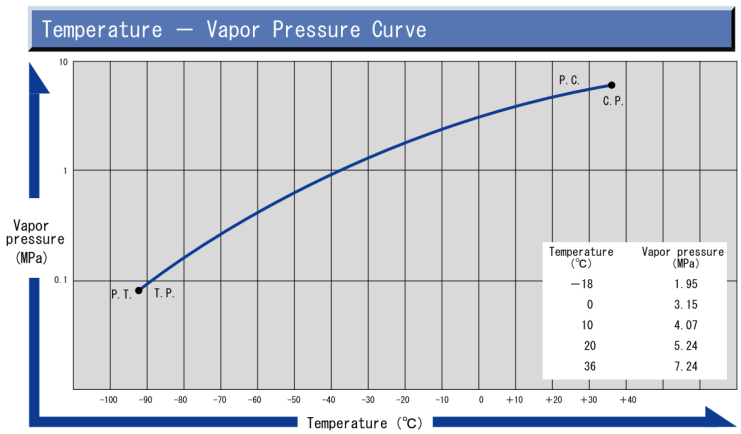

Figure 2.1: Nitrous oxide vapour pressure curve (Showa Denko, 1998)

However, hydrazine is very toxic and both hydrazine and hydrogen peroxide do not have self-pressurizing properties due to the low vapour pressure (0.00345 bar and 0.0214 bar respectively). When comparing nitrous oxide as a bi-propellant with other conventional bi-propellant combinations, the following performance is found, presented in Figure 2.2. Here it can be seen that in a bi-propellant configuration nitrous oxide has a lower specific impulse compared to a more conventional propellant combination like nitrogen tetroxide (NTO) and hydrazine, however it still performs well enough to be used as a non-toxic alternative.

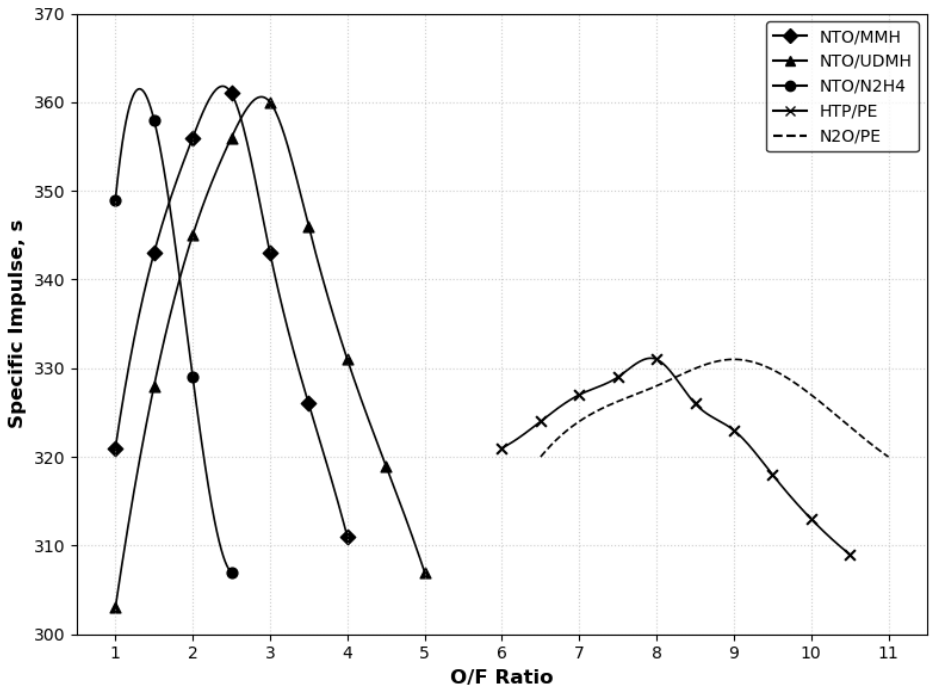

Figure 2.2: Theoretical comparison between different bi-propellant combinations (Re-plotted in python based on data from Zakirov et al., 2001)

For this thruster design, ethane was chosen as the fuel. However, at the start of the project the fuel was still undecided, and a study was performed. With respect to liquid bi-propellant thrusters utilizing nitrous oxide, multiple fuels have been explored. In the coming paragraph, some of these fuels will be elaborated on. For this study, NASA CEA was used to compare the specific impulse of different fuels used with nitrous oxide for different O/F ratios. The simulation was done at sea-level conditions with a chamber pressure of 7.5 bar, and gave the following results, which can be seen in Figure 2.3.

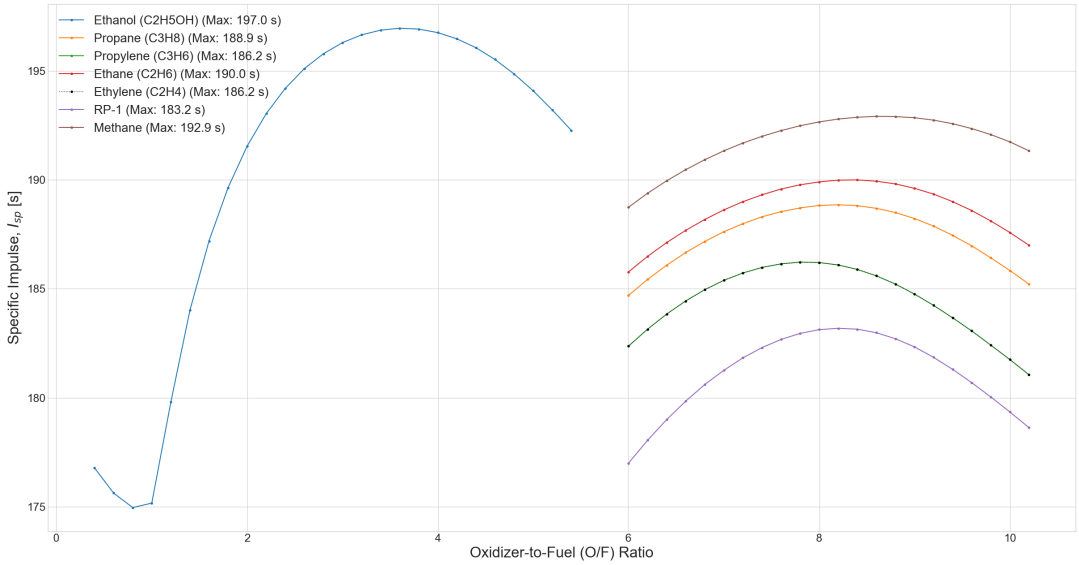

Figure 2.3: Specific impulse comparison for various fuels used with nitrous oxide using NASA CEA

Firstly, ethanol (C_2H_5OH), which has a higher specific impulse (in combination with nitrous oxide) compared to other fuels also has multiple advantages, like simple storage, non-toxicity, and accessible, inexpensive procurement. Ethanol also has good properties for a coolant (specific heat capacity, thermal conductivity), which makes it a good option as a fuel (The Engineering Toolbox, 2024). A downside of ethanol is that during combustion, it first needs to break down into oxygen and hydrocarbons before it can act as a fuel (Millán-Merino et al., 2018). This increases the ignition delay time and thus requires a longer residence time in the combustor, and possibly a longer combustion chamber, such that complete combustion can occur. Furthermore, unlike nitrous oxide, ethanol has no self-pressurizing properties. This makes it necessary that an external pressurizing tank is present to pressurize the ethanol, increasing the complexity and size of the system. Two other fuels that are often used in combination with nitrous oxide are propane (C_3H_8) and propylene (C_3H_6). The benefit of both of these fuels is that they are self-pressurizing, eliminating the need for an external pressurization system, as they have a vapour pressure at room temperature of around 9.4 and 10.2 bar, respectively. Although the two fuels are very similar in thermophysical properties, there are differences which could lead to the choice of one or the other. In the past, propane was used more frequently due to its easy procurement and handling and good properties (Tyll and Herdy, 2001), while nowadays companies opt more for the use of propylene, due to its higher flame temperature and better combustion properties (Dawn Aerospace, 2025). Two other options that are currently being explored by companies developing small thrusters are ethane (C_2H_6) and ethylene (C_2H_4), or mixtures of the two fuels (Janzer et al., 2022). Like propane, propylene, and nitrous oxide, ethane also has self-pressurizing properties where the vapour pressure at room temperature is 38.45 bar (Sigma-Aldrich, 2025). Ethylene is not self-pressurizing, unless it is kept artificially cooled below its critical point at 9.2 °C. Another fuel that is regularly used in the rocket industry is methane (CH_4), often in liquid form. Together with nitrous-oxide, methane has the highest specific impulse of all the hydrocarbons, as can be seen in Figure 2.3. However, the critical temperature of methane is −82.44 °C, making it unsuitable for self-pressurization (The Engineering Toolbox, 2025).

When using a hydrocarbon as fuel, coking should also be taken into account, especially near the injector. Coking creates small carbon deposits during combustion, which could block injector channels or lead to injector misalignment. It is particularly important when the fuel is used as a coolant, since in that case it could lead to blocking of the cooling channels (Zhu et al., 2023). However, the thruster designed in this thesis uses nitrous oxide as its coolant, so it does not present an issue.

This section described the current state-of-the-art in terms of rocket engine propellants. In order to select a propellant a trade-off should be performed and simulations should be done. This will be discussed in chapter 4.

2.2. Thrust Chamber

The main component of any thruster is the thrust chamber, which consists of the combustion chamber, the throat, and the nozzle. Usually these three segments are composed of one single component; however, it could be that the component is split into two or more, for example, when a separate film cooling component is installed somewhere along the length of the combustion chamber. One of the important trade-offs that need to be performed during the design phase is the material of this component. Nowadays, rocket engine designers often prefer to use additive manufacturing methods to design a rocket engine thrust chamber over conventional machining (Kerstens et al., 2021). This is mainly due to the fact that regeneratively cooled chambers are much more common, and are difficult to manufacture with conventional machining methods due to the very small cooling channels.

2.2.1. Material

For nitrous oxide thrusters, there are multiple things that should be considered. Firstly, if nitrous oxide were to be used as the coolant (in the case of regenerative cooling), the material of the thruster should not be affected by oxidation. Furthermore, the material should be able to withstand high temperatures, but also have a good heat conductivity to lead the heat away to the coolant. The risk with nitrous oxide is that if it absorbs too much heat, it will decompose inside the cooling channel, which could release even more heat and cause failure of the material. One of the materials widely used in the rocketry industry is Inconel-718, which is a high-strength, corrosion-resistant, nickel-chromium alloy (SPECIAL METALS, 2007). This material can withstand high temperatures up to almost 1000 K, however it has a low thermal conductivity between 10 and 30 $\mathrm{Wm^{-1}K^{-1}}$, depending on the temperature (Díaz-Álvarez et al., 2017). An improved version of Inconel-718 is ABD900AM, which is age-hardened and as a result can withstand temperatures up to almost 900 °C (see Appendix A.1). Another recently developed material by NASA (specifically for thrust chamber applications) is GRCop-42 (Gradl et al., 2019). This material can withstand high temperatures up to 1033 K and also has a higher thermal conductivity compared to the previous options, namely between 320 and 350 $\mathrm{Wm^{-1}K^{-1}}$, depending on the temperature. Other options generally used in rocket engines are CrCuZr, Ti-6Al-4V, Copper and AlSi10Mg.

2.2.2. Design Theory

In principle, thrust chambers operate in a relatively simple manner. The propellants are initially injected into the chamber at a high pressure. These propellants are then ignited, and due to a combustion process called deflagration[1], the flame becomes "self-sustaining". By combusting the propellants, the chemical energy is converted into thermal energy and added to the flow. By accelerating the flow in a converging section and expanding the flow directly after in a diverging section, a large portion of this thermal energy is converted into kinetic energy, leading to supersonic flow at the outlet.

In an ideal rocket motor this process happens isentropically, meaning that there is no change in entropy, due to the fact that the process is adiabatic (no heat exchange) and reversible. For an initial design, this is a good starting point. However, the design must still be verified using analytical tools and physical testing.

Based on the first law of thermodynamics, which states that the energy entering a system equals the change in stored energy plus the energy leaving the system, a derivation of the flow pattern can be made. Assuming adiabatic conditions and omitting the storage term in the energy balance, the energy balance reduces to:

$$h + \frac{1}{2} \cdot U^2 = h_{tot} \tag{2.1}$$

Here, h [$\mathrm{J\,kg^{-1}}$] is the specific enthalpy (which is the sum of the internal energy and flow work), h_{tot} [$\mathrm{J\,kg^{-1}}$] is the total specific enthalpy, $\frac{1}{2} \cdot U^2$ is specific kinetic energy [$\mathrm{J\,kg^{-1}}$] and U [$\mathrm{m\,s^{-1}}$] is the flow velocity. Assuming ideal gases, the specific enthalpy is equal to the specific heat [$\mathrm{J\,kg^{-1}\,K^{-1}}$] multiplied by the absolute temperature [K] in the combustion chamber ($C_p \cdot T_c$). Since isentropic flow is assumed, the Poisson relations can be used (Zandbergen, 2022):

$$\left(\frac{T}{T_c}\right) = \left(\frac{p}{p_c}\right)^{\left(\frac{\gamma-1}{\gamma}\right)} = \left(\frac{\rho}{\rho_c}\right)^{(\gamma-1)} \tag{2.2}$$

Here, γ is the ratio of specific heats ($\frac{C_p}{C_v}$), T is temperature, P is pressure and ρ is density. The subscript c means the combustion chamber. Now, if we take the relative flow velocity to be zero in the combustion chamber, the energy equation from Equation 2.1 can be simplified to:

[1] Deflagration is a combustion process where the combustion propagates at subsonic speeds. At supersonic speeds this process is called detonation.

$$c_p \cdot T_c = c_p \cdot T + \frac{1}{2} \cdot U^2 \tag{2.3}$$

Rearranging and implementing the trivial equations for the speed of sound, γ and the specific gas constant, the following equation can be found for the flow velocity in the nozzle:

$$U = \sqrt{2 \cdot \frac{\gamma}{\gamma - 1} \cdot \frac{R_A}{M} \cdot T_c \cdot \left(1 - \frac{T}{T_c}\right)} \tag{2.4}$$

Inserting Equation 2.2 into Equation 2.4 gives:

$$U = \sqrt{2 \cdot \frac{\gamma}{\gamma - 1} \cdot \frac{R_A}{M} \cdot T_c \cdot \left(1 - \left(\frac{p}{p_c}\right)^{\left(\frac{\gamma-1}{\gamma}\right)}\right)} \tag{2.5}$$

From this relation the nozzle velocity can be derived from the local pressure, as is illustrated in Figure 2.4. Here, depending on the geometry, the following flow patterns are possible:

(a) Subsonic flow

(b) Choked flow

(c) Shock in nozzle

(d) Shock at exit

(e) Overexpanded

(f) Design condition

(g) Underexpanded

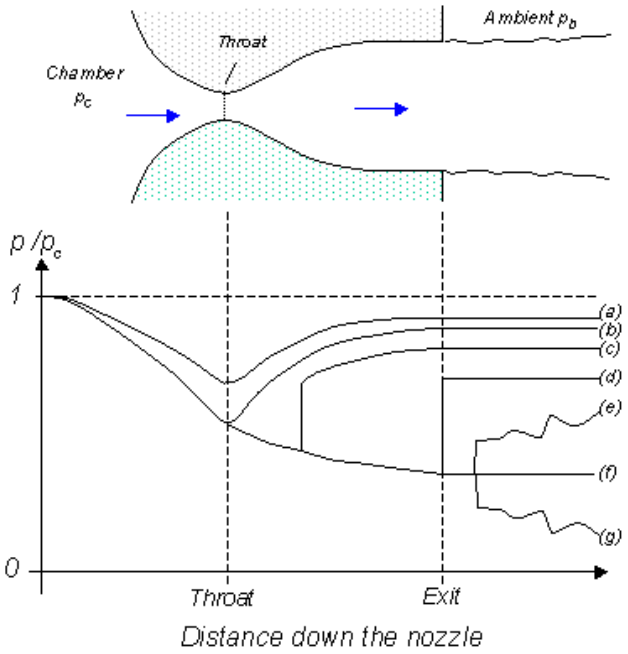

Figure 2.4: Normalized pressure distribution along the nozzle (Devenport, 2001)

This means, that if one would know the design condition pressure at the outlet, using Equation 2.5 the exit velocity can be found. Together with the desired thrust the required mass flow can be found. If the exit pressure is not perfectly expanded, there is also a pressure thrust component.

$$F = \dot{m} \cdot U_e + (p_e - p_0) \cdot A_e \tag{2.6}$$

In order to achieve the design condition (f), choking must occur in the throat. This means that at that point the flow is at M=1 and cannot accelerate any further. This occurs when the ratio between the upstream and downstream pressure is at the “critical pressure ratio”. The value of this ratio is given by Equation 2.7.

$$\left(\frac{p_t}{p_c}\right)_{cr} = \left(\frac{2}{\gamma + 1}\right)^{\left(\frac{\gamma}{\gamma-1}\right)} \tag{2.7}$$

Based on Poisson’s equation, the critical pressure ratio equation and the continuity equation, Equation 2.8 for the critical mass flow can be derived:

$$\dot{m}_{cr} = \frac{\Gamma \cdot p_c \cdot A_t}{\sqrt{R \cdot T_c}} \tag{2.8}$$

Where Γ is the Vandenkerckhove function, which is defined as Equation 2.9:

$$\Gamma = \sqrt{\gamma} \cdot \left(\frac{2}{\gamma + 1}\right)^{\left(\frac{\gamma+1}{2(\gamma-1)}\right)} \tag{2.9}$$

Inserting Equation 2.8 and Equation 2.5 into Equation 2.6 and assuming perfect expansion ($p_e = p_0$), the mass flow rate can be found as well as the chamber pressure, since in adiabatic flow T_c is equal to the adiabatic flame

temperature, which is known if the propellants are known as well as the O/F ratio.

In Figure 2.5 a graph shows the dimensionless mass flow versus the pressure ratio. Here, choking can be observed where the dimensionless mass flow is maximum.

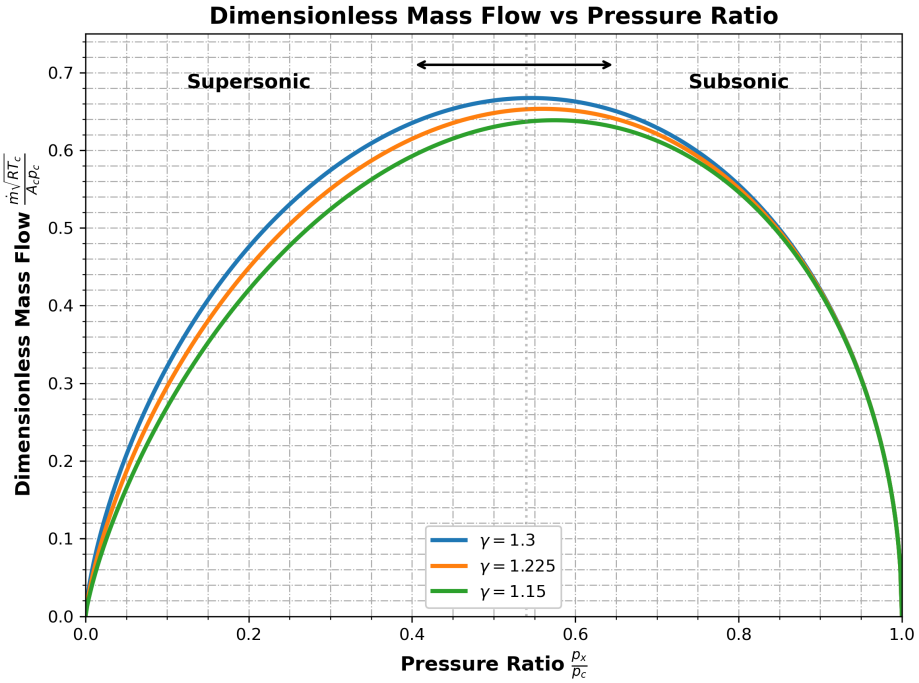

Figure 2.5: Dimensionless mass flow versus pressure ratio with various heat capacity ratios in the case of a converging-diverging nozzle (Adapted from van der Laan and Timnat, 1985).

Based on these known values for chamber pressure, exit pressure, chamber temperature and exit velocity, using Equation 2.2 and the critical ratio's for density and temperature, the nozzle expansion ratio equation, which will not be derived here, can be found:

$$\frac{A_e}{A_t} = \left(\frac{2}{\gamma+1}\right)^{\left(\frac{1}{\gamma-1}\right)} \cdot \left(\frac{2}{\gamma+1}\right)^{\left(\frac{1}{2}\right)} \cdot \left(\frac{p_c}{p_e}\right)^{\left(\frac{1}{\gamma}\right)} \cdot \frac{\sqrt{\gamma \cdot R \cdot T_c}}{U_e} \tag{2.10}$$

It should be noted that as this engine will be optimized for operation in atmospheric conditions, the expansion ratio will be rather small compared to other in-space propulsion thrusters, where the expansion ratio is usually quite large ($\tilde{1}00$ for Dawn Aerospace's B20 thruster (SmallSat Catalog, 2026)).

In rocket propulsion, some characteristic parameters have been developed in order to verify the performance of the engine. These are the characteristic thrust coefficient C_F, which shows the ratio between the thrust due to expansion of the gases compared to the thrust that would exist solely due to the pressure difference between the chamber and the exit. The formula for C_F is given by:

$$C_F = \Gamma \cdot \sqrt{\frac{2\gamma}{\gamma-1} \cdot \left[1 - \left(\frac{p_e}{p_c}\right)^{\left(\frac{\gamma-1}{\gamma}\right)}\right]} + \left(\frac{p_e}{p_c} - \frac{p_a}{p_c}\right) \cdot \frac{A_e}{A_t} \tag{2.11}$$

In the case of perfect expansion ($p_e = p_a$) the right component disappears. Another important quantity is the characteristic velocity c^* [$\mathrm{m\,s^{-1}}$], which is a value that shows how much of the propellant energy can be used for the purpose of propulsion, and is described by the following equation:

$$c^* = \frac{1}{\Gamma} \cdot \sqrt{R \cdot T_c} \tag{2.12}$$

Using Equation 2.8 and rearranging gives:

$$c^* = \frac{p_c \cdot A_t}{\dot{m}} \tag{2.13}$$

These two parameters can then be used to determine another characteristic parameter called the specific impulse (I_{sp} [s]). This is arguably the most important parameter in rocket propulsion if you want to see the performance of your engine. It's in essence a way to see how much thrust is generated per unit mass flow, and is given by the following relation, where U_{eq} [m/s] is the mass-equivalent velocity:

$$I_{sp} = \frac{F}{\dot{m} \cdot g_0} = \frac{U_{eq}}{g_0} = \frac{C_F \cdot c^*}{g_0} \tag{2.14}$$

Another important parameter is the characteristic chamber length L^* [m]. This length is a key performance metric that indicates the mixing length available in the combustion chamber. It is expressed using the following equation:

$$L^* = \frac{V_{cc}}{A_t} \tag{2.15}$$

With the contraction ratio ϵ_c (see Equation 2.16) and the characteristic length specified from previous designs, the combustion-chamber length can be determined, and—using the results from the previous calculations—the chamber diameter can then be obtained.

$$\epsilon_c = \frac{A_c}{A_t} \tag{2.16}$$

There are also certain efficiencies that can be estimated when designing a thrust chamber. For a bell nozzle the following equation can be used (Ponomarenko, 2010):

$$\zeta_d = 1 - \frac{\left(\frac{2}{k+1}\right)^{\frac{1}{k-1}} [z(\lambda_e) - 1] - \bar{P}}{\left(\frac{2}{k+1}\right)^{\frac{1}{k-1}} z(\lambda_e)} \tag{2.17}$$

Where,

ζ_d = Bell nozzle efficiency [−]

k = Ratio of specific heats [−]

λ_e = Velocity coefficient at the nozzle exit [−]

$\bar{P}$ = Normalized pressure [−]

and $z(\lambda_e) = 0.5(\lambda_e + 1/\lambda_e)$ [−]

Alternatively, for a conical nozzle with nozzle exit half-angle θ_e the efficiency caused by divergence losses is (Ponomarenko, 2010),

$$\zeta_d = \frac{1 + \cos\theta_e}{2} \tag{2.18}$$

and the efficiency caused by friction losses is,

$$\zeta_f = 1 - \frac{2\delta_e^{**}}{R_e} \tag{2.19}$$

Where δ_e^{**} is the boundary layer thickness and R_e is the nozzle exit radius. Furthermore, another important efficiency is the reaction efficiency. Since ideal rocket theory assumes infinitely fast chemistry, a reaction efficiency should be introduced to get a more realistic value for the combustion performance:

$$\zeta_r = (1 - \xi_r)(1 - \xi_r') \tag{2.20}$$

The term ξ_r can be estimated using the following empirical relation:

$$\xi_r = \left(\frac{h_0}{r_t}\right)^a \left(\frac{p_{st}}{p_c}\right)^b \log_{10}\left(\frac{r_e}{r_t}\right) \tag{2.21}$$

Where,

p_{st} = Ambient pressure at sea level [Pa]

p_c = Chamber pressure [Pa]

r_t = Nozzle throat radius [m]

r_e = Nozzle exit radius [m]

The parameters h_o, a and b are dependent on the propellants used. The term ξ_r' represents the increase in loss for low-pressure combustion chambers and is given by:

$$\xi_r' = \max\left[0, \frac{2.1 - \ln(p_c/(2\cdot 10^6))}{100}\right] \tag{2.22}$$

2.3. Cooling Methods

One of the preferred objectives of the thruster is to be able to fire in steady-state mode. This means that the thruster can fire indefinitely without any failure. To achieve this, the thruster must be either passively or actively cooled while firing, as the flame temperature of nitrous oxide together with the previously discussed hydrocarbons can be as high as 3100 K, which is far higher than any material can sustain, as explained in the previous paragraph. To cool the engine to an acceptable temperature level, there are multiple methods as per Huzel, 2000. The first, and currently most used method in rocket engines, is regenerative cooling. This method utilizes one of the propellants and feeds it through cooling channels in the thrust chamber wall, which makes it absorb the heat and cool down the wall between the hot gas and the incoming propellant. This can be seen in Figure 2.6. For nitrous-oxide based engines that want to achieve steady-state mode, regenerative cooling is often used (Palej and Palacz, 2018). As small nitrous-oxide bi-propellant engines often operate at a high O/F ratio (in the case of a hydrocarbon fuel), the mass flow of the fuel is usually too low to be able to cool down the thrust chamber sufficiently. Thus, nitrous oxide should be used as the coolant. However, this means that thorough simulations should be performed to ensure that the temperature of the incoming nitrous oxide does not become too high and cause decomposition. Another method which is similar to regenerative cooling is dump cooling. Here, the coolant is also fed through the walls, however after it has gone through the entire length of the chamber, it is dumped overboard.

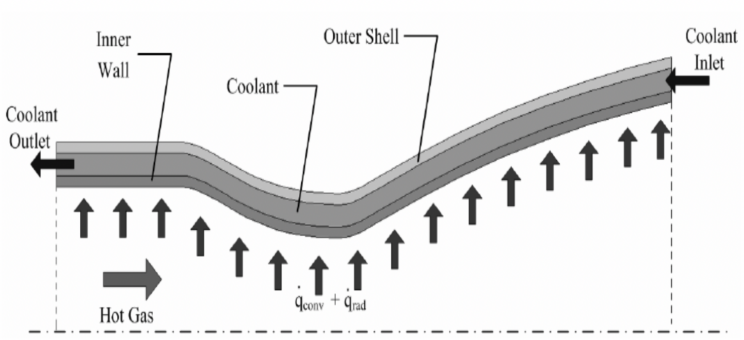

Figure 2.6: Regenerative cooling concept (Alexander Hodge, 2022)

When designing for regenerative cooling with nitrous oxide, one should take into account the effect of being near the critical point, which for nitrous oxide is 72.38 bar (Ohgaki et al., 1990). Thermodynamic quantities like thermal expansion and heat capacity can vary greatly when approaching the critical point compared to its nominal values and gradient with temperature (Greer and Moldover, 1981). This makes designing for a two-phase fluid more complicated and modelling less reliable, unless it is accounted for, but this in turn increases the complexity of the computation and thus the computational time.

Apart from the challenges of nitrous-oxide being a two-phase fluid which brings thermodynamic challenges, it is also often used as a monopropellant due to the high energy it releases upon decomposition, approximately 86.1 kJ/mol (Yamamoto and Tachibana, 2024). However, when it is used as a coolant, decomposition inside the cooling channels should be avoided. In monopropellant thrusters, catalysts are often used in order to stimulate decomposition. Materials like copper and zinc are often mentioned as catalysts for N_2O (Martin-Luengo, 2001). Thus, these materials should be avoided or at least limited in terms of material composition when selecting the components

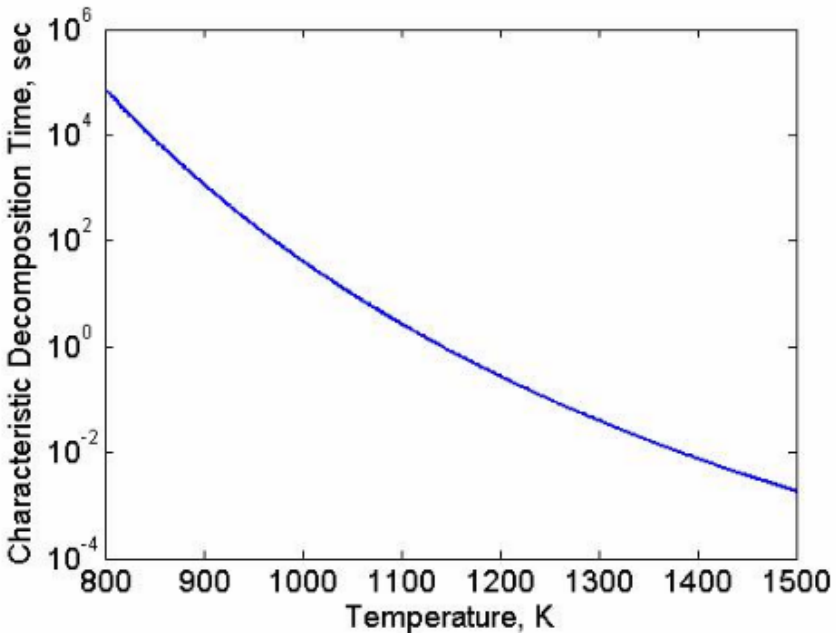

Figure 2.7: Characteristic decomposition time as a function of temperature at pressures larger than 40 atm (Karabeyoglu et al., 2008).

that will be in contact with N_2O. Nevertheless, even with avoiding these materials, the coolant should still be kept under a maximum temperature for an extended period of time. Figure 2.7 shows how long it would take for N_2O to decompose depending on the temperature. As the chamber is fairly small, it should not pose any problems, however it should definitely be taken into account.

The third cooling method is film cooling. This method can be used by itself but is also often used in combination with regenerative cooling. Instead of injecting all the fuel and nitrous oxide through the injector, a percentage of one of these is injected from the chamber wall near the injector, this helps protect the wall from high heat fluxes and also (at a lower efficiency compared to direct injection) contributes with the overall reaction. A fourth method of cooling is called transpiration cooling. This method utilizes very small holes in the wall of the combustion chamber that feed the coolant into the thrust chamber at a sufficient rate to maintain the preferred wall temperature.

Another method which generally is a more simple option in terms of design but rather difficult to achieve in practice is radiation cooling. This cooling method does not use any active cooling, but rather relies on the shape of the thruster outer wall to radiate the heat away from the thruster efficiently. However, this is difficult to achieve and does have its limitations, mainly due to the limited cooling capacity (Zhao et al., 2025). However, it is used in different liquid nitrous oxide-based thrusters, such as the N_2O/C_3H_6 thruster developed by the universities of Trieste and Derby, however after 50 ms of firing the inner wall temperature reaches already 1200K, which is near the maximum temperature for nominal performance of ABD900AM as previously discussed in section 2.2 (Lepore et al., 2025).

A final cooling method, which is commonly used in combination with one of the other cooling methods but is not capable of steady-state firing by itself, is ablative cooling. This cooling method does not actively cool the wall, but rather applies a thin layer of insulation between the inner wall and the flame which burns away slowly during a fire, allowing the thruster to fire longer than it could without this layer. Indian scientists developed an thruster combining liquid film cooling with an ablative layer at the throat (where often the temperature is the highest) and achieved good results, with a maximum wall temperature of 840 K (Navaneethan et al., 2025).

2.3.1. Regenerative Cooling Theory

In order to have an estimation of the regenerative cooling effect and wall temperatures, preliminary calculations must be made using heat transfer theory. In this section, the relevant theory and assumptions that were made during the initial design process will be shortly discussed.

In heat transfer theory, there are three modes of heat transfer:

- Radiation
- Convection
- Conduction

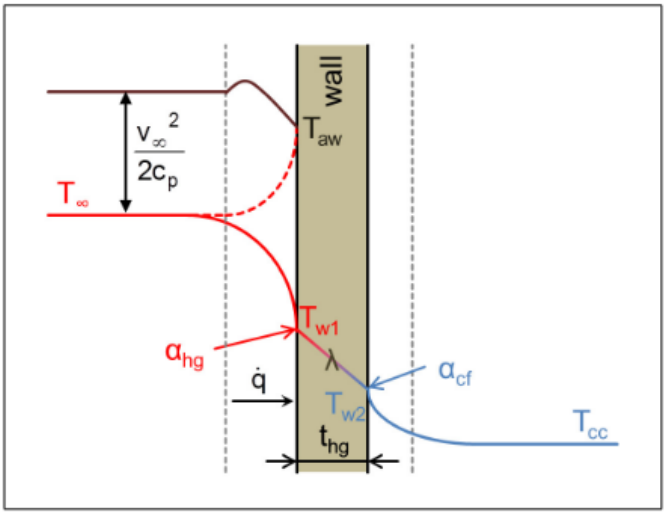

Figure 2.8: Schematic of Regenerative Cooled Wall (Kirchberger, 2014)

In rocket engines radiative heat transfer occurs mainly inside the combustion chamber, where heat radiates away from the hot gasses, but also at the outer combustion chamber wall, where the heat radiates away from the combustion chamber itself. In regenerative cooled thrusters convection happens in two places, namely in the combustion chamber and inside the cooling channels, this mode is usually estimated using the so-called Nusselt number, however this will be discussed later. The last mode, conduction, is the heat transfer inside the walls of the combustion chamber, and thus depends on the material's thermal conductivity.

Radiative heat transfer is the transfer of energy through electromagnetic waves (Kirchberger, 2014). As the wavelength of these waves depend on the molecular structure, it is important to know the species present in the combustion chamber flame in order to derive an approximation of the radiation to the chamber wall. If for now we assume infinitely fast, equilibrium combustion between N_2O and a hydrocarbon (C_nH_m), a relatively good first assumption is that the two main exhaust species are H_2O and CO_2. However naturally there are many more species like intermediate species in combustion, and other exhaust species like C_2H_2, O_2, N_2 etc. During the CFD analysis, a large portion of these species will be covered, but for an initial estimation H_2O and CO_2 are sufficient. For the radiative heat transfer in the model that was used in this thesis, the following equations were used for the heat flux $\dot{q}_{rad}$ (Kirchberger, 2014):

$$\dot{q}_{rad,H_2O}\left[\frac{\mathrm{W}}{\mathrm{m}^2}\right] = 5.74 \cdot (P_{H_2O} \cdot r_c)^{0.3} \cdot \left(\frac{T_{hg}}{100}\right)^{3.5} \tag{2.23}$$

$$\dot{q}_{rad,CO_2}\left[\frac{\mathrm{W}}{\mathrm{m}^2}\right] = 4 \cdot (P_{CO_2} \cdot r_c)^{0.3} \cdot \left(\frac{T_{hg}}{100}\right)^{3.5} \tag{2.24}$$

If the radiative heat flux due to radiation is known, generally using the absorption coefficient, in that case it is calculated how much radiation is actually absorbed by the material. This is given by the following relation:

$$\dot{q}_{abs} = \alpha \cdot \dot{q}_{received} \tag{2.25}$$

However, to assume the worst case scenario where all the heat is absorbed by the material, a black body is assumed, meaning $\alpha = 1$.

The most prominent form of heat transfer in rocket engines however is the convective heat transfer. There are two types of convective heat transfer, namely natural convection and forced convection. Natural convection occurs due to differences in density from temperature variations, which creates buoyancy forces. Forced convection occurs due to a flow moving over a surface, carrying the heat with it. In rocket engines, forced convection takes place in the cooling channels and combustion chamber, while natural convection happens at the outer wall of the thruster, assuming the thruster is firing in atmospheric conditions and the surrounding air is motionless. In general, convective heat transfer can be estimated by using Newton's law of cooling (Zandbergen, 2022):

$$q_\alpha = h_\alpha \cdot (T_s - T_r) \tag{2.26}$$

Here, the heat transfer coefficient is not known and should be derived. This coefficient can be calculated in multiple ways, but one of the most common methods is by using the Nusselt number. This number is a dimensionless value that can be used to calculate the heat transfer coefficient using the following relation, where k is the thermal conductivity and x is a characteristic dimension:

$$h_\alpha = Nu \cdot k/x \tag{2.27}$$

There have been many studies on calculating the Nusselt number and many empirical relations have been derived, however a few have shown good results. Based on results found by Werling and Hörger, 2021, for the hot gas side heat transfer and for combustion near the stoichiometric O/F ratio, both the Cinjarew and Gnielinski relations gives the best approximation, as can be seen in Figure 2.9. Bartz tends to overestimate the heat flux at stoichiometric conditions, but is better for oxygen-rich flames.

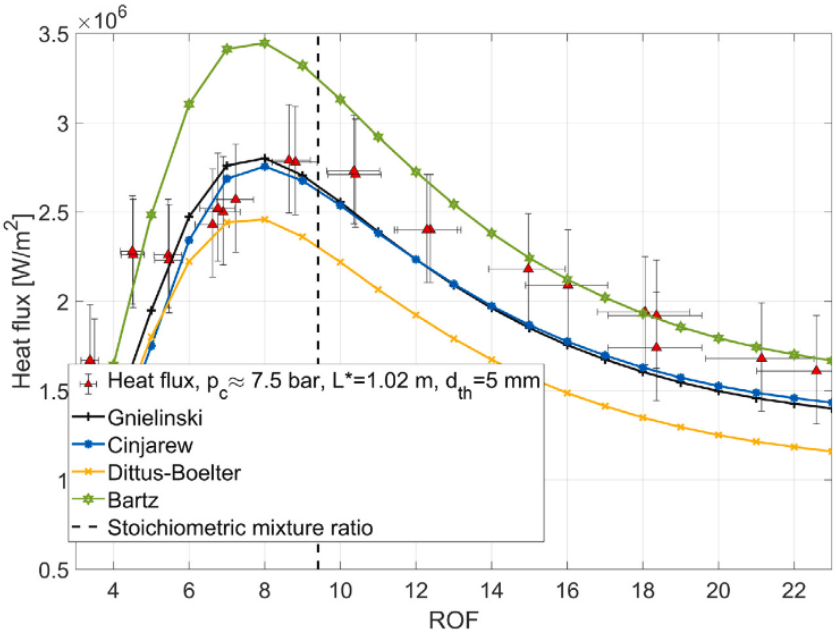

Figure 2.9: Experimental heat flux and heat flux calculated via modified Nusselt correlations (Werling and Hörger, 2021).

The Nusselt number relations for Cinjarew (Equation 2.28) and Gnielinski (Equation 2.29) are the following:

$$Nu_{m,Ci} = 0.0162 \cdot (Re \cdot Pr)^{0.82} \cdot \left(\frac{T_{Stag}}{T_{wall}}\right)^{0.35} \tag{2.28}$$

$$Nu_{m,Gn} = \frac{\frac{\xi}{8}(Re - 1000) \cdot Pr}{1 + 12.7 \cdot \sqrt{\frac{\xi}{8}}\left(Pr^{\frac{2}{3}} - 1\right)} \left[1 + \left(\frac{d_h}{l_{pipe}}\right)^{\frac{2}{3}}\right] \tag{2.29}$$

Here, T_{stag} is the stagnation temperature, defined as:

$$T_{stag} = T_{stat} + r_c \cdot (T_c \cdot \eta_{c^*}^2 - T_{stat}) \tag{2.30}$$

Where T_c is the adiabatic flame temperature, r_c is the recovery factor, an empirical value that is normally between 0.7 and 0.9 (Werling and Hörger, 2021), η_{c^*} is the combustion efficiency and T_{stat} is the static temperature. For both relations it is also necessary to calculate the Reynolds number and Prandtl number, which are given by the following relations:

$$Re = \frac{\rho \cdot v \cdot l}{\mu} \tag{2.31}$$

$$Pr = \frac{\mu \cdot c_p}{\lambda} \tag{2.32}$$

Where,

Re = Reynolds number, −

Pr = Prandtl number, −

ρ = Density of the fluid, $\mathrm{kg\,m^{-3}}$

v = Velocity of the fluid, $\mathrm{m\,s^{-1}}$

l = Characteristic length, m

μ = Dynamic viscosity, Pa s

c_p = Specific heat capacity, $\mathrm{J\,kg^{-1}\,K^{-1}}$

λ = Thermal conductivity, $\mathrm{W\,m^{-1}\,K^{-1}}$

For the thermal conduction in the chamber wall, the following relation can be used:

$$q_x = \frac{k}{L} \cdot \Delta T \tag{2.33}$$

Where k is the thermal conductivity, L is the wall thickness between the coolant and the combustion chamber and ΔT is the difference in temperature.

2.3.2. Thermostructural Theory

In rocket engine thrust chambers, structural integrity is critical. Thus, a thermostructural analysis must be performed both during the design process, and with FEA after the initial design. In a thrust chamber, multiple different types of loading/stresses occur.

The main stresses in a rocket engine thrust chamber are the hoop stress due to the pressure differential between the chamber pressure and coolant pressure, the thermal stress due to the thermal gradient in the combustion chamber wall and the bending moment stress due to discontinuities (bolts, supports). These can be combined into the following equation for the combined tangential tensile stress (Huang and Huzel, 1992):

$$S_t = \frac{(p_{co} - p_g)r}{t} + \frac{E\alpha q t}{2(1-\nu)k} + \frac{6M_A}{t^2} \tag{2.34}$$

Where,

S_t = Combined tangential tensile stress [Pa]

q = Heat flux [$\mathrm{W\,m^{-2}}$]

r = Tube radius [m]

t = Tube wall thickness [m]

p_{co} = Coolant pressure [Pa]

p_g = Combustion gas pressure [Pa]

E = Modulus of elasticity of tube wall material [Pa]

a = Thermal expansion coefficient of tube wall material [$\mathrm{K^{-1}}$]

k = Thermal conductivity of tube wall material [$\mathrm{W\,m^{-1}\,K^{-1}}$]

υ = Poisson's ratio of tube wall material

M_A = Bending moment caused by discontinuity [N m m^{-1}]

In Figure 2.10, a typical chamber cross-section utilizing regenerative cooling can be seen.

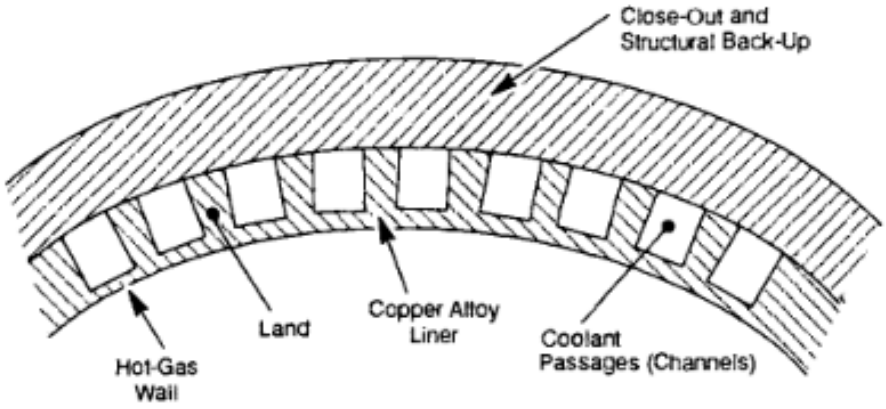

Figure 2.10: Typical chamber wall geometry (Huang and Huzel, 1992)

Because the outer wall thickness is much larger than the inner wall thickness, and due to the fact that there is a thermal gradient, thermal inelastic buckling will be induced, and thus it is necessary to calculate this value in order to make sure it is not too large. This stress in the longitudinal direction can be estimated with the following equation:

$$S_l = E \cdot a \cdot \Delta T \tag{2.35}$$

Where,

S_l = Thermal stress, Pa

E = Modulus of elasticity of tube wall material, Pa

a = Thermal expansion coefficient of tube wall material, K^{-1}

ΔT = Temperature difference across the wall, K

According to Huang and Huzel, 1992, this stress should be kept at a level not higher than 0.9 the critical buckling stress, S_c which is given by:

$$S_c = \frac{4E_t E_c t}{(\sqrt{E_t} + \sqrt{E_c})^2 \sqrt{3(1-\nu^2)}r} \tag{2.36}$$

Where,

S_c = Critical stress for longitudinal inelastic buckling in zone I, Pa

E_t = Tangential modulus of elasticity at wall temperature, Pa

E_c = Tangential modulus of elasticity from compression stress-strain curve, at wall temperature, Pa

t = Tube wall thickness, m

ν = Poisson's ratio of tube wall material

r = Tube radius, m

Finally, the tangential and longitudinal stresses can be combined into the so-called Von Mises equivalent stress, which is given by the following formula:

$$S_{vm} = \sqrt{S_t^2 - S_t S_l + S_l^2} \tag{2.37}$$

Where,

S_{vm} = Von Mises equivalent stress, Pa

S_t = Combined tangential tensile stress, Pa

S_l = Longitudinal thermal stress, Pa

This stress should be directly compared to the yield strength of the material, in order to obtain a good estimation of the structural integrity of the thrust chamber.

2.4. Injector

Another very important component in a thruster is the injector. Over the years, many injector designs have been tried and tested; however, there does not exist any "one size fits all". Injectors, as the name suggests, inject both the fuel and oxidizer into the combustion chamber. This can be done in a pre-mixed manner, where the fuel and oxidizer are thoroughly mixed before injection, or in a non-premixed manner, where the fuel and oxidizer are injected separately. Choosing the right injector and the right injector dimensions is a crucial part of thruster design, and requires many tests and simulations to verify the correct operation. For rocket engines and thrusters, there are a few types of injectors that are used the most. In small thrusters, usually direct impinging injectors are used due to their small size and low residence time, requiring the reaction to happen quickly. Impinging injectors can be both like and unlike-impinging, this means that either the fuel and the oxidizer are directly colliding, or an oxidizer stream is colliding with another oxidizer stream and likewise with the fuel. According to Huzel, 2000, like-impinging elements are more often used for bi-liquid propellants where heat transfer between the unlike-impinging streams is non-preferable. However, mixing is better in unlike-impinging streams. For these configurations, the most usual setup is either doublets or triplets. This means that there is either one or two oxidizer orifices for every fuel orifice. When sizing an orifice, Huzel presents an empirical formula to determine the diameter.

$$\mathrm{d_{orifice}} = \left(\frac{3.627 \mathrm{K\dot{w}^2}}{\rho \Delta \mathrm{PN}^2} \right)^{0.25} \tag{2.38}$$

Where,
$d_{orifice}$ = orifice diameter $[in]$ K = head-loss coefficient [-]
$\dot{w}$ = flow rate $[lb/s]$
ρ = density $[lb/ft^3]$
ΔP = pressure drop $[lb/in^2]$
N = number of orifices [-]

However, unfortunately the orifice diameter is in reality not so easily determined, as usually the amount of orifices is unknown, since it highly depends on manufacturability of the part and combustion stability. To give a good estimation, injection-orifice sizes range from 0.004 inch (0.1 mm) for a small thruster (1 lb (0.45 kg)) to 0.75 inch (1.91 cm) in a pressure fed booster (Huzel, 2000).

Another possible injector that is often used is called a swirl injector. Swirl injectors itself also vary, but a common type used in both big and small thrusters is a coaxial swirl injector (Lee et al., 2020). This injector initially gives both the fuel and oxidizer a tangential speed, which makes both of them come out of in a cone-like shape, improving mixing and thus combustion efficiency. Recently, another type of injector was tested with in a N_2O/C_2H_6 thruster, namely injection through a porous material (Mananssis, 2020). A benefit of this type of injection is that mixing is highly improved due to the turbulence created by the material. A downside is that the material could lead to higher mass flows on one side of the injector compared to another side, leading to combustion instability or heat spots.

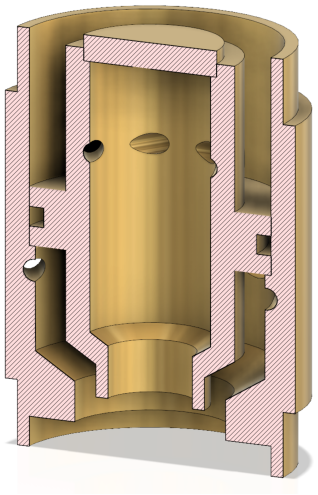

Figure 2.11: Swirl injector developed by Copenhagen Suborbitals (Copenhagen Suborbitals, 2019)

An additional common injector used in rocket engines is a pintle injector, which injects one of the propellants outward (radially) from the center, and the other propellant axially alongside the pintle injector face. This causes mixing

near the pintle head, which generally results in good atomization and mixing characteristics (Kang et al., 2022). Another benefit of pintle injectors is that it can be used for throttling a thruster by varying the orifice size and thus varying the mass flow. It is used in many big recent rocket engines such as SpaceX's Falcon 9 Merlin engine (Fischer, 2010). However, it is less commonly used in small thrusters, as better options exist when throttling is not necessary and residence times are short.

2.5. Igniter

In order to obtain combustion (unless the propellants are hypergolic), an ignition source is required. In small thrusters, there are two common igniters to achieve this, namely a spark plug, or a glow plug. Spark plugs are very often used in small thrusters because of their reliability, size, and fast actuation. Glow plugs are more used in the automotive industry (particularly in diesel engines), but are also making their way into space. A benefit of glow plugs is that they have a long life cycle and are very well able to withstand the high temperatures of the engine. Furthermore, glow plugs are more reliable when used in lower ambient temperatures. The difference between the two is that spark plugs directly provide ignition to the propellants, requiring it to be directly inserted into the combustion chamber, while glow plugs rather "pre-heat" the combustion chamber, ensuring the propellants reach the autoignition temperature when injected. In 2009, NASA tested out different types of glow plugs in a liquid-oxygen/methane thruster, where it found that a ceramic sheathed glow plug performed very well, achieving successful ignition during each fire (Breisacher and Ajmani, 2009). However, the ceramic glow plug required around 7.2s to reach its maximum temperature, which complicates firing in quick pulsed mode. NASA ran tests at multiple different voltage levels for both the metal sheathed and ceramic sheathed glow plugs, and here it was found that the ceramic sheathed glow plugs reached a higher temperature for a lower voltage level, as can be seen in Figure 2.13 and Figure 2.14.

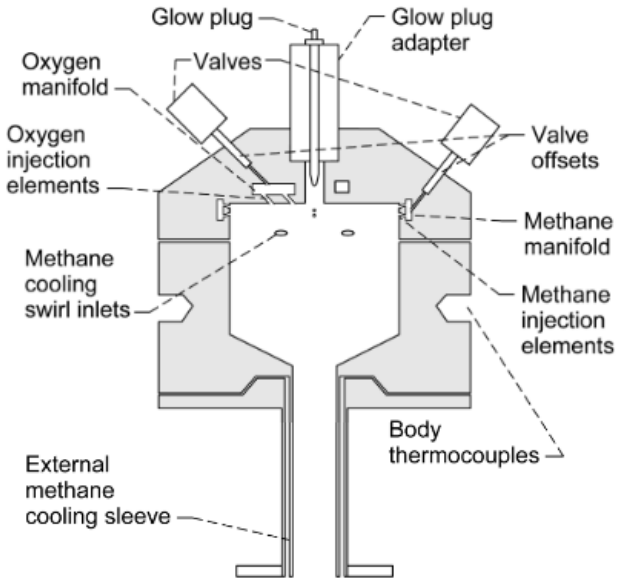

Figure 2.12: Glow plug igniter schematic (Breisacher and Ajmani, 2009)

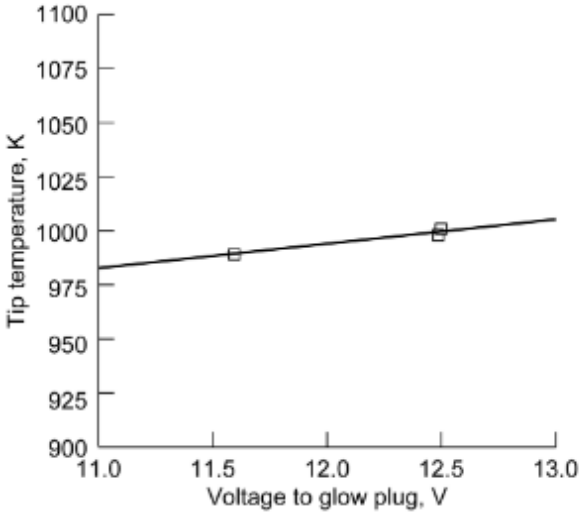

Figure 2.13: The tip temperature obtained for the voltage applied to a metal sheathed glow plug (Breisacher and Ajmani, 2009).

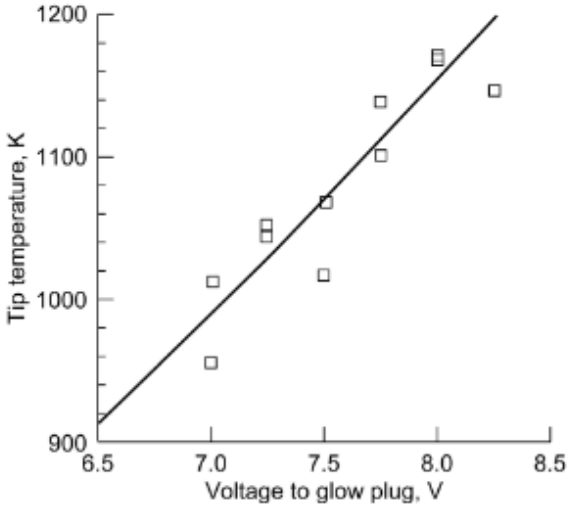

Figure 2.14: The tip temperature obtained for the voltage applied to a ceramic sheathed glow plug (Breisacher and Ajmani, 2009).

NASA also performed firings of both types of glow plugs using an igniter assembly as was previously shown in Figure 2.12, and performed them at different firing conditions. The tests were performed with liquid oxygen and methane, where in a "warm" conditions the propellant lines were unconditioned and around room temperature, and in the "cold" conditions the propellant lines were cooled with liquid nitrogen. The cold igniter was cooled with liquid methane, while the warm igniter was not cooled at all. The nozzle or no nozzle condition depends on the exit of the full igniter assembly, and is not necessarily applicable for this thesis. The firings were performed with a ceramic and metal glow plug, where the metal glow plug was either coated or not coated with a catalyst.

Table 2.1: Summary of Glow Plug Ignition Results (Breisacher and Ajmani, 2009)

Valve Type	**Firing Conditions** (Propellant / Igniter / Nozzle)	**Voltage** (V)	**Tip Temp** (K)	**Ignited** (Y/N)
Ceramic Sheathed	Warm / Warm / No Nozzle	8.0	1174	N
	Warm / Warm / No Nozzle	8.5	1231	Y/N
	Warm / Warm / No Nozzle	9.5	1372	N
Coated Metal Sheathed	Warm / Warm / No Nozzle	11.0	978	Y/N
	Warm / Warm / No Nozzle	11.5	984	N
Metal Sheathed	Warm / Warm / With Nozzle	11.5	984	Y/N
	Warm / Warm / With Nozzle	12.0	989	N
Coated Metal Sheathed	Warm / Warm / With Nozzle	12.25	992	N
	Warm / Warm / With Nozzle	12.5	995	Y
Ceramic Sheathed	Warm / Cold / With Nozzle	8.3	1199	Y
Ceramic Sheathed	Cold / Cold / With Nozzle	8.3	1199	Y
Metal Sheathed	Cold / Cold / With Nozzle	12.5	995	Y/N

From this table it can be seen that the ceramic sheathed in general has a better performance than the metal sheathed glow plug as it consistently achieved ignition. This is likely due to the higher tip temperature.

Another commonly used igniter in larger rocket engines is a torch igniter. However, this type of igniter is generally not used in small engines due to its size and complexity.

2.6. Verification

Once any product of engineering is designed, its design needs to be verified. It depends on what type of product you are verifying, but generally for high-tech engineering products, this is done by rigorous testing, bringing the capabilities of the product to its absolute limit. For structural and material parameters, this is usually done by using high safety factors (depending on the application) and inducing stress into the structure at the critical location. While for performance parameters, often a range is used within which the specific parameters must fall. For rocket engines one might think about parameters like thrust, mass flow, pressure drops and temperature. However, depending on the application, these two might be closely connected, and as such they are usually verified together in a single test. To come up with a structure of testing that is deemed sufficient by the industry, big space organizations such as NASA and ESA have both come up with guidelines on how to verify a product that is to be used in space. This does not only include engines but can be applied to essentially any space engineering product, such as tanks, satellite structures or solar panels. These verification standards are called "Verification Handbook" from NASA (Chubb and McDonough, 1994) and ECSS Space Engineering Verification (ECSS, 2018) from ESA. It should be noted that these are just rough guidelines for performing verification of a space product, and with the fast evolving industry new, more agile guidelines might be developed in order to accelerate development.

In Figure 2.15, a hot-fire can be seen, which is one of the most important tests in the rocket engine verification phase, as this test can verify the structural integrity of the thruster (apart from fatigue, unless the test is repeated many times), as well as the most critical performance parameters. Usually in the case of smaller in-space propulsion thrusters, but sometimes also with bigger engines, the hot-fire verification test is initially performed in atmospheric conditions, but is as a final test also performed in vacuum, in order to almost completely simulate the space environment. The hot-fire in Figure 2.15 shows the LUMEN setup, an upper stage rocket engine demonstrator developed by

DLR, which can be used by companies and institutions to verify different parts of a rocket engine without having to develop the entire system (DLR, 2024).

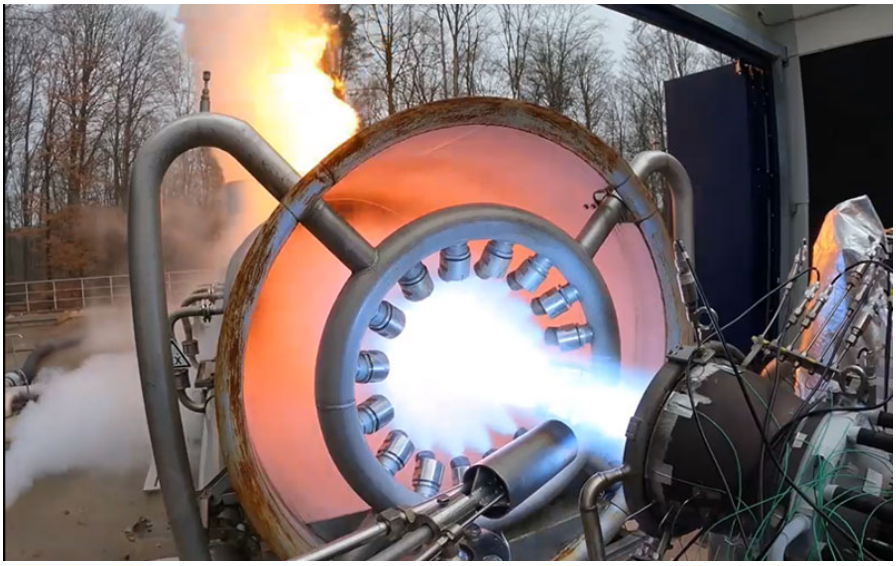

Figure 2.15: Hot-fire of the LUMEN upper stage rocket engine (Parsonson, 2024)

However, these documents and what has been described before just cover one part of the verification of a thruster. Often, due to restrictions caused by high temperatures, manufacturing issues or other problems, physical verification can't always be used to verify these parameters. A safe, and reliable, but time-consuming way to obtain these data points is to perform verification by means of analysis. Usually this type of analysis is done in steps, where during the initial design phase, either a custom code is written, or a simple program is used, that can present rough data and results for critical parameters. In the case of a rocket engine that has the goal of being fired in steady-state mode, this is often the inner wall temperature, and the stresses caused by the thermal gradients inside this wall. As this temperature could lead to rapid failure of the engine, a preliminary verification is absolutely necessary during the initial design phase, and often it is one of the leading design parameters.

In order to have a more accurate verification of the engine by means of analysis, a high-fidelity tool such as Computational Fluid Dynamics (CFD) is often used in combination with Finite Element Analysis (FEA). CFD is generally used to verify performance parameters such as thrust, pressure, mass flow and temperature, while FEA is used to verify the structural integrity of the system by simulating the induced stresses and characterizing the failure modes.

CFD is used in many fields, not only aerospace. If done well, it can be an accurate tool, however, it should also be noted that there is a trade-off to be made between computational time, and accuracy. One should always take into account that the tool will never be 100% accurate, and if possible other means of verification are required in order to completely close a requirement. CFD functions by dividing the fluid domain into many cells. Usually (but not always), the more cells are used in a domain, the more accurate the solutions becomes, at the cost of computational time, which can be seen in Figure 2.16 in the case of a wind turbine farm CFD simulation. Furthermore, in the case of this thesis, one also would want to simulate the complex combustion inside the engine as well as the complicated flow path of the injector and the heat transfer from the flame to the wall and coolant in the case of regenerative cooling. These factors all complicate the CFD simulation and should be taken into account before starting verification using CFD. In order to verify the CFD itself, other previously performed similar CFD simulations and certain key parameters of these simulations should be compared. However, as engines of this type are fairly novel, it is difficult to find a case that matches yours, which should be taken into account during the verification process.

2.7. Literature Study Conclusion

Nitrous-oxide space propulsion is still a fairly novel concept (Grubelich and Lindblom, 2013). However, enough research has been performed on the separate characteristics that come with small bi-propellant thrusters such that

conclusions can be drawn. Regarding the fuels, ethanol seems to have very good cooling properties, however it does lack self-pressurization. Together with the fact that the design has to allow for different fuels, hydrocarbons such as ethylene, ethane, propane, or propylene seem to be a good option, especially also due to their self-pressurizing properties. In that case nitrous-oxide could be used as the coolant due to the high O/F ratio.

For cooling, this is generally difficult to achieve in small engines, however regenerative cooling seems to be the preferred method, with radiation cooling as an alternative. Some engines do utilize film cooling also, however this would make the system more complex, and would make the modularity aspect more difficult as now the design of the manifold would also have an effect on the cooling abilities of the thruster. It should be noted that with N_2O as coolant, having it in gaseous state does reduce its cooling abilities, which should be taken into account during modelling and testing.

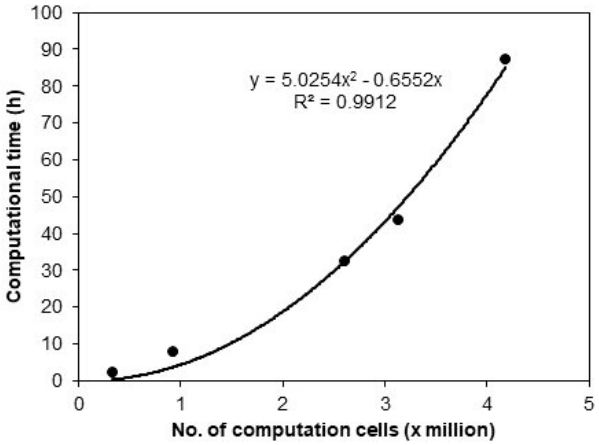

Figure 2.16: Exponential increase of computational time depending on the number of cells (Kim, 2019)

For manufacturing of the different components in more recent engines, additive manufacturing is the norm. This allows for smaller cooling channels and more complex geometries, while retaining the high thermal properties with materials such as ABD900AM or IN718. A trade-off must be made between thermal conductivity and strength/fatigue properties at high temperatures. GRCop-42 offers high thermal conductivity (and thus better cooling) but lower strength properties at high temperature, while ABD900AM and IN718 offer low thermal conductivity but higher strength properties at higher temperatures. It should also be taken into account that when too much heat is transferred to the coolant, it might heat up too much and risk decomposition inside the cooling channels.

In the last decades many injector designs have been developed. While pintle injectors allow for throttling and good atomization/mixing, impinging injectors are suitable for small engines due to its simple geometry and small size. Coaxial swirl injectors are also commonly used in newer engines, showing promising mixing capabilities and fewer combustion instabilities.

In small-scale thrusters, there are generally two igniters that are commonly used. The most common igniter is the spark plug igniter, which creates a small spark at a specific time, leading to a high temperature hotspot, igniting the flow. While a glow plug rather pre-heats the chamber, reaching temperatures up to 1200K, such that when the propellants reach the combustion chamber, they mix and combust almost instantly.

Finally once the design is finalized, it must be verified using both physical methods and analytical methods such as CFD or FEA. This is critical in order to avoid failure during physical testing. During this verification process, generally guidelines such as ECSS are followed in order to verify all the functional, performance and structural requirements. Computational fluid analysis data on nitrous-oxide based thrusters (especially at this scale) is scarce, leading to a gap that must be explored in this thesis. Furthermore, CFD can be used to simulate new injector designs and manifold configurations, such as coaxial swirl injectors.

2.8. Research Questions and Objectives

Before the start of the thesis, a research plan was set up. This document describes the background of the topic, and lays the groundwork for the thesis, describing the timeline, the research question(s) and overall goal of the thesis. This thesis was performed by request of the European Space Agency, which is currently developing a new chemical propulsion laboratory in the Netherlands, which will serve as a platform for institutions and commercial companies to perform small (chemical) thruster testing inside the Netherlands. The thesis has the following as its main objective:

Main Research Objective

To design and manufacture a 20 N nitrous oxide (N_2O) bi-propellant thruster with a modular architecture, allowing for flexibility of fuels, injector configurations, and ignition systems.

Next to the main objective, before the start of the thesis, multiple secondary objectives as well as some preferred objectives were determined.

Secondary Objectives

- The thruster designed during the thesis shall be able to perform pulse-mode operation[2]
- The thruster designed during the thesis shall allow for heat load measurement at the chamber in different axial directions
- The thesis shall include procurement of parts from manufacturers
- The design of the thruster shall be iterated at least once in cooperation with the manufacturing authority
- The thesis shall be performed within the allocated budget of the European Space Agency
- The performance of the thruster shall be verified using both thermal and mechanical analysis as well as simulations
- Preferred objective: The thruster designed during the thesis shall be able to fire in steady-state mode[3]
- Preferred objective: Computational Fluid Dynamics (CFD) shall be performed on the thruster to verify its performance

From these objectives, multiple research questions can be stated on how these objectives can be achieved.

Research Questions

- How can a thruster architecture be designed to allow for the interchange of different fuels, injector concepts, and ignition systems while remaining leak tight, without performance loss and failure-proof?
- What design features are critical to optimizing pulse-mode performance, specifically to achieve a low minimum impulse bit, minimize propellant dribble volumes, and ensure pulse-to-pulse repeatability?
- With what methods can the heat loads on the thruster be measured, and how do they compare to both (other) experimental and analytical values?
- Which combustion chamber material and cooling method would allow for steady-state firing of this thruster?
- How can the thruster design be optimized to be manufacturable and within budget?

[2] "Pulse mode operation" means that the thruster can perform short (hot-)fires of generally a few hundred ms.
[3] "Steady-state mode" means that the thruster shall have sufficient cooling capabilities to be able to remain firing indefinitely without failure

3
Requirements

In this chapter, the requirements for the project will be elaborated on. The main requirements are the stakeholder requirements. From these requirements, design requirements were created as well as verification/test requirements. The requirements are then inserted into a verification control matrix (VCM), where the specific test method to verify the requirement is indicated, this matrix can be found in Appendix D.

In order to determine which test method would be used in order to verify a requirement, a simple procedure was followed. Firstly, the criticality of the requirement needed to be assessed, as well as the required accuracy of the verification. Generally, physical tests (depending on the type of test) are more accurate than simulations. Thus, if for a requirement a high accuracy was required, and it could be verified with both analysis and physical testing, physical testing was preferred. If a slightly lower accuracy is sufficient, analysis would be chosen. Secondly, depending on the test, sometimes multiple requirements can be verified with a single test, like a hot-fire. If this was the case, physical testing would always be preferred. Lastly some requirements either have to be verified by physical testing or by analysis, as the other method is simply not possible.

3.1. Stakeholder requirements

Before the start of the thesis, a list of high-level requirements was set up by the European Space Agency. These requirements consisted of a variety of must-haves and some objectives that were desirable, but not absolutely critical. For the trade-offs, these requirements were the main starting point and key guidelines to follow, however during the design process there was regular contact with the European Space Agency in order to guide the design and make changes where necessary.

[HL-1] The thruster shall allow testing for more than one; fuel, injector, and igniter type

[HL-2] The thruster shall be designed to allow heat load measurement at the chamber at different axial directions

[HL-3] The thruster shall have a minimum impulse bit (MIB) of 250 ms

[HL-4] As a goal, the thruster may be designed to sustain steady-state firing

[HL-5] The thruster shall use nitrous-oxide as the oxidizer

[HL-6] The thruster shall be used in bi-propellant configuration

[HL-7] The thruster shall be manufactured within the budget value of TBD EUR

[HL-8] The thruster shall be optimized for firing in atmospheric conditions

[HL-9] The thruster shall not exceed a thrust of 25 N

3.2. General Requirements

To ensure that the project ran smoothly, some general requirements had to be specified. The requirements are still related to the engine design, however are not specific to one type of requirement category, and rather encompass the entire project as a whole. In this specific project, the general requirements will include safety conditions to ensure that testing can be performed safely. It should be noted that this does not include safety margins, as these are discussed in the respective part structural requirements section. There will also be interface requirments to ensure that the thruster can be used on the ESA test bench.

3.2.1. Safety Conditions

Regardless of testing activities, safety should always be the number one priority, both for the environment and personnel. To perform tests safely, certain precautions can be taken, however there should also be extensive safety procedures in case unexpected system failures occur.

- All testing activities shall be performed by using extensive testing procedures
- Applicable Personal Protective Equipment (PPE) shall be used during all testing activities
- The propellant feed system shall not have any sections where high pressure gases could be trapped
- If testing is performed outside, once the system is pressurized, all personnel shall maintain a distance of at least 10 meter
- If testing is performed inside, once the system is pressurized, all personnel shall be inside the control room
- Each test shall be preceded by a documented Test Readiness Review (TRR) and an approved test procedure defining hazards, mitigations, and go/no-go criteria
- The test setup shall include an emergency shutdown capability (so-called E-stop) that places the system in a safe state (e.g. closing propellant valves and venting where applicable) from the control room

3.2.2. Interface Requirements

As this project only includes the engine, and it's main components, interface requirements should be defined such that the testing setup developed by ESA and the engine components are compatible. Furthermore, sensor requirements are also included in this section.

[3.2.2-1] The thruster shall have propellant connections compatible with 1/8" NPT fittings

[3.2.2-2] The thruster shall include eight thermocouples and pressure sensor ports at the thrust chamber, manifold and both propellant valve interfaces

[3.2.2-3] The thruster assembly shall mechanically interface with the thrust plate

[3.2.2-4] All measurement equipment used for acceptance testing (pressure, temperature, thrust, mass flow) shall be calibrated

[3.2.2-5] All test tolerances values shall be according to the guidelines from the ECSS-E-10-03A standard

[3.2.2-6] The combustion chamber shall accommodate a high-frequency pressure transducer

3.3. Thrust Chamber Requirements

While every part of a liquid rocket engine is important, the thrust chamber has the biggest impact on performance, and due to the high combustion temperature, it is also the most common source of destructive failure.

3.3.1. Functional Requirements

[3.3.1-1] The combustion chamber inner wall shall withstand a temperature of maximum 1100 K

[3.3.1-2] The engine shall be designed in such a way so that the temperature will not exceed 900 K during steady-state operations.

[3.3.1-3] The thrust chamber material shall be compatible with nitrous-oxide, ethane, propylene, propane, ethylene, and methane

[3.3.1-4] The thrust chamber material shall not be reactive with a catalyst for nitrous-oxide decomposition

[3.3.1-5] The thruster shall be fired for 60 seconds or longer at least once without failure

[3.3.1-6] The thruster shall deliver a total impulse across its lifetime of at least 20 000 N s

[3.3.1-7] The thruster shall be fired at least 10000 times across its lifetime

3.3.2. Performance Requirements

[3.3.2-1] The combustion chamber MEOP shall be 7.5 ± 0.5 bar

[3.3.2-2] The thruster shall have a specific impulse at sea-level of at least 170 ± 5 s

[3.3.2-3] Steady state thrust (or chamber pressure) oscillations shall not exceed more than 5% (3% as a goal) of the local average thrust (or chamber pressure) at all frequencies at the trim point

[3.3.2-4] For the whole pressure box, the steady state thrust (or chamber pressure) oscillations shall not exceed more than 12% at all frequencies

[3.3.2-5] The thrust shall be 20 ± 1 N at sea-level conditions

[3.3.2-6] The thrust chamber shall be designed such that the combustion gases expand into atmospheric pressure (101 325 Pa)

3.3.3. Structural Requirements

[3.3.3-1] The thrust chamber shall meet the requirements of this document after being subjected to a proof pressure of 1.5 times the maximum expected operating pressure (MEOP)

[3.3.3-2] The thrust chamber shall withstand a pressure of 2.5xMEOP without rupture

[3.3.3-3] The thrust chamber shall be manufacturable by means of additive manufacturing methods

[3.3.3-4] The combustion chamber contraction ratio shall be in the range 1:4 to 1:11

[3.3.3-5] The thrust chamber shall have a non-permanent interface connection with the injector plate

[3.3.3-6] The maximum hoop stress in the thrust chamber shall be less than half of the yield strength of the thrust chamber material at the location of maximum wall temperature

[3.3.3-7] The thrust chamber shall not exceed the maximum amount of cycles specified by the material supplier corresponding to the maximum wall stress

[3.3.3-8] The thrust chamber roughness inside the cooling channels shall be less than 20 µm

3.4. Injector and Manifold Requirements

The design of the thruster has multiple configurations, and due to the modularity the injector can be configured in almost any way. However, these requirements will specifically be applicable to three configurations. Namely the configuration with a central coaxial swirl injector and a glow plug, the configuration with an off-center coaxial swirl injector and an off-center glow plug and finally the configuration with triplet injection and a spark plug.

3.4.1. Functional Requirements

[3.4.1-1] The injector material shall be compatible with nitrous-oxide (N2O)

[3.4.1-2] The injector material shall be compatible with various hydrocarbons (C2H6, CH4, C3H8, C2H4 and C3H6)

[3.4.1-3] The external leak rate (before and after operation) shall not exceed $1 \times 10^{-6}\,\mathrm{scc\,s^{-1}}$ with the propellant equipment pressurised at MEOP1 with Helium

[3.4.1-4] The manifold/injector shall either have an M10 or M8 female thread to house a glow plug or a 1/4x32 thread to house a spark plug

3.4.2. Performance Requirements

[3.4.2-1] The injector shall allow for an oxidizer mass flow rate[1] of $0.010\,42\,\mathrm{kg\,s^{-1}}$

[3.4.2-2] The injector shall allow for a fuel mass flow rate[1] of $0.001\,16\,\mathrm{kg\,s^{-1}}$

[3.4.2-3] The injector shall allow for a minimum pressure drop of 1 ± 0.5 bar

[3.4.2-4] The igniter shall demonstrate repeatable ignition over the defined operating envelope, with a minimum ignition success rate to be agreed for acceptance testing

[1] In the case of ethane as fuel

3.4.3. Structural Requirements

[3.4.3-1] The material of the injector shall stay below a temperature of 1000 K

[3.4.3-2] The injector shall be manufacturable using conventional machining methods or additive manufacturing

[3.4.3-3] The injector shall interface with the injector manifold

3.5. Igniter Requirements

Since it is desired for this engine to perform hot-fires and not only cold-flows, and furthermore the propellants used in this engine are not hypergolic, an igniter is necessary to be installed. This igniter will either be a glow plug or a spark plug, depending on the configuration.

3.5.1. Functional Requirements

[3.5.1-1] The igniter shall cause auto-ignition of the two propellants when initiated at operational pressure and temperature

[3.5.1-2] The igniter shall not cause decomposition and ignition of the propellants in their separate injector zones

[3.5.1-3] The external leak rate (before and after operation) shall not exceed 1×10^{-6} scc s^{-1} with the propellant equipment pressurised at MEOP1 with Helium

3.5.2. Performance Requirements

[3.5.2-1] The igniter shall heat up to a temperature of at least 1200 K

[3.5.2-2] The igniter shall have a thread compatible with the injector/manifold

[3.5.2-3] The diameter of the igniter tip (heating element) shall not be more than 5.5 mm

3.5.3. Structural Requirements

[3.5.3-1] The igniter body shall stay below its melting temperature

3.6. Valve Requirements

The engine will have two valves, one valve for the oxidizer side and one valve for the fuel side. Since this engine will not be used in space and only be fired on a test setup, it was deemed acceptable to have one main valve per propellant instead of the industry standard of having both an isolation valve and a main valve for redundancy. The valves are fast-acting poppet valves supplied by Gevasol.

3.6.1. Functional Requirements

[3.6.1-1] The external leak rate (before and after operation) shall not exceed 1×10^{-6} scc s^{-1} with the propellant equipment pressurized at MEOP1 with Helium

[3.6.1-2] The internal leak rate (before and after operation) shall not exceed 1×10^{-4} scc s^{-1} with the propellant equipment pressurized at MEOP1 with Helium

[3.6.1-3] The proof pressure (1.5xMEOP) shall be sustained for a min. period of time of 5 minutes

[3.6.1-4] The burst pressure (4xMEOP) shall be sustained for a min. period of time of 1 minute

[3.6.1-5] The valve shall either open or close within 15 ms

3.6.2. Performance Requirements

[3.6.2-1] The ethane valve shall allow for a mass flow of 0.001 16 kg s^{-1}

[3.6.2-2] The nitrous oxide valve shall allow for a mass flow of 0.010 42 kg s^{-1}

[3.6.2-3] The pressure drop of the valve at a mass flow rate of 0.010 42 kg s^{-1} of nitrous oxide shall not exceed 0.5 bar

4
Design Methodology

In the following chapter, the full design process of the thruster will be elaborated on, including all the relevant components. This is the first version of the design, which has been verified using analysis, however physical tests might show that changes need to be made in order to improve either the functionality, performance or structural integrity. Furthermore, the design is modular, so this chapter will show three different configurations, however many more configurations with a different fuel, injector, or igniter are possible. Technical drawings for all the designs, without dimensions for the additively manufactured parts, can be found in the appendix. It should be noted that trade-off results are shown in the design methodology instead of in the results section. This is done, as often the subsequent design steps were dependent on the results of the trade-off that was performed before.

4.1. Propellants

As nitrous-oxide already was fixed as the oxidizer when the project started, only a fuel still had to be selected in order to perform the design. However, it should be noted that the design is modular, and should thus allow for multiple different fuels.

When selecting a fuel, multiple criteria are important. Firstly, it should be safe and relatively easy to handle the fuel when performing tests or filling operations. As this is one of the advantages why nitrous-oxide is used, it would be unadvisable to use a fuel that is toxic or unsafe like for example hydrazine. Secondly, it is preferable that the propellant is able to self-pressurize, as this would reduce the need for a pressurizing tank and make the feed system less complex. Thirdly, the specific impulse of the fuel when used with nitrous-oxide is a very important criteria in order to have good performance of the engine. For this, Figure 2.3 was used as a comparison guideline. Fourthly, either the cooling capability (only important in the case of regenerative cooling, which will be discussed in the next section) of the fuel, or the O/F ratio if N_2O is used as coolant, as a higher O/F ratio means a higher N_2O mass flow. Fifthly, cost/procurability is also an important criterion.

With these criteria in mind, a quantitative trade-off was performed between a range of different fuels that can be seen in Table 4.1. For this trade-off, the criteria were weighted as follows: handling (20%), self-pressurization (25%), specific impulse (25%), O/F (20%) and cost (10%). Self-pressurization and specific impulse were rated the highest as those are the most critical to the design. As the feed system and tank design is separate from this thesis, a non-self-pressurized propellant would result in a more complex systems engineering tasks where the feed system (designed by ESA) and the thruster are more intertwined. The total score is then calculated by multiplying the rating with the corresponding weight and taking the sum of all those values. Specific impulse is critical as it directly relates to the performance, which is desired to be maximum. The scores range from -2 to 2, where -2 is very unfavourable and 2 is very favourable. The scores in this trade-off and the next trade-offs are determined based on general knowledge, analyses, and literature. The scores are also based on the comparison with another option. For example, propylene and ethane both have self-pressurizing properties at room temperature, however the pressure (at the same temperature) of ethane is higher, and is thus given a score of 2 instead of 1. This method is also applied in the other trade-offs.

Table 4.1: Fuel trade-off for a modular 20 N N_2O-oxidized thruster (gaseous injection; room-temperature storage; regen-cooled; N_2O as coolant).

Fuel	Handling	Self-press.	I_{sp}	Cooling / O/F	Cost / proc.	Total
Weight	*0.20*	*0.25*	*0.25*	*0.20*	*0.10*	—
Propylene	2	1	1	1	1	**1.20**
Ethane	2	2	1	1	1	**1.45**
Ethylene	1	-1	2	1	0	**0.65**
Propane	2	1	1	1	1	**1.20**
Methane	1	-2	2	2	0	**0.50**
RP-1	1	-2	0	0	0	**-0.30**
Ethanol	2	-2	2	2	2	**1**

Rating legend: 2 very favourable, 1 favourable, 0 depends, -1 unfavourable, -2 very unfavourable.

In the following paragraphs below a justification will be presented for each criterion.

Handling scores reflect toxicity, cryogenic requirements, and the amount of safety precautions needed in a test environment. A score of 2 is assigned to fuels that are non-toxic, non-cryogenic, and handleable with standard laboratory PPE (propylene, ethane, propane, ethanol). A score of 1 is assigned to fuels with mild additional hazards such as flammability or asphyxiation risk requiring extra precautions (ethylene, RP-1). Methane can be used at cryogenic temperatures making it harder to handle, but when used as a gas handling is on the same level as propylene. To account for both cases, it has been given a score of 1.

Self-pressurization scores are based on the saturation vapour pressure at room temperature (~293 K) relative to the required feed pressure. A score of 2 is assigned when the saturation pressure is well above the feed pressure, allowing firing without external pressurization (ethane, ~42 bar at 293 K). A score of 1 is assigned when the saturation pressure is sufficient but leaves a low margin (propylene, ~10 bar; propane, ~8.4 bar). A score of −1 is assigned when the critical point is close to room temperature, making self-pressurization unreliable (ethylene, T_c = 282.4 K, The Engineering Toolbox, 2025). A score of −2 is assigned when the critical point is well below room temperature and self-pressurization is entirely impossible (methane, T_c = 190.56 K, The Engineering Toolbox, 2025; RP-1; ethanol).

Specific impulse scores are assigned relative to the theoretical sea-level I_{sp} at the optimum mixture ratio with N_2O, using Figure 2.3 as the reference. A score of 2 is assigned to the best performing fuels. A score of 1 is assigned to fuels with good but not peak performance. A score of 0 is assigned to fuels with comparatively moderate performance (RP-1 with N_2O).

Cooling / O/F scores reflect the suitability for regenerative cooling when N_2O is used as the coolant. Since a higher O/F ratio increases the N_2O mass flow through the cooling channels, a higher O/F is preferred. A score of 2 is assigned to fuels with a high O/F ratio with N_2O (methane, O/F ≈ 7–9) or fuels with a high heat capacity and thermal conductivity (ethanol). A score of 1 is assigned to fuels with moderate O/F ratios (propylene, ethane, ethylene, propane). A score of 0 is assigned to fuels with a lower O/F ratio and average cooling properties (RP-1).

Cost / Procurability scores reflect availability and unit cost. A score of 2 is assigned to chemicals available off-the-shelf or from industrial suppliers at low cost (ethanol). A score of 1 is assigned to fuels available from industrial gas suppliers at moderate cost (propylene, ethane, propane). A score of 0 is assigned to fuels requiring more specialized suppliers and thus a higher cost (ethylene, methane, RP-1).

From this trade-off it was concluded that propylene, propane, and ethane were the best options, however ethane was selected as the fuel for this design, due to the higher vapour pressure than propylene and propane. Furthermore, there were also some concerns regarding coking of ethylene due to its double bonds (Badawy et al., 2018), which made ethane the best choice. What is not visible in the trade-off table but what was also considered is that modularity of fuel is a top-level requirement, meaning that if a fuel (such as ethanol) would be used as the coolant, the geometry of the cooling channels would need to be changed if the fuel is changed to another type. Thus, it was decided that it would be easier to have a hydrocarbon as a fuel, and using nitrous oxide as the coolant, resulting in better interchangeability between (hydrocarbon) fuels, without having to change the thrust chamber geometry.

4.1.1. Sensitivity Analysis

In order to ensure that the weights are properly assigned and that the results do not significantly shift upon a change in weighting, a sensitivity analysis should be performed. This is done by having each weight increased and decreased by 100% and comparing the results with the median current result, observing if a slight change in weight would have a big impact on the result. For the propellant trade-off the following is found in Figure 4.1.

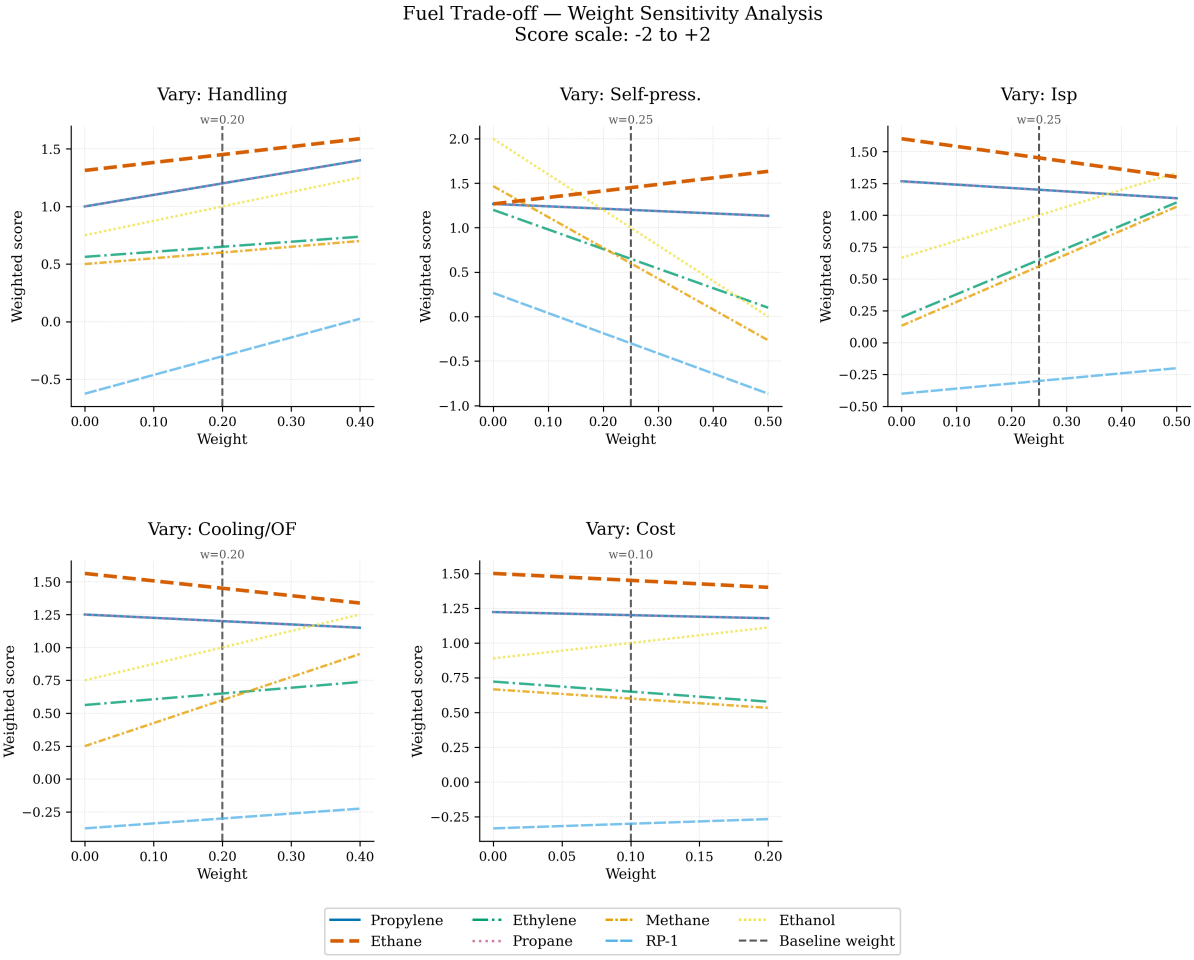

Figure 4.1: Fuel sensitivity analysis

From this analysis it can be seen that even with varying weights, ethane is still the best option. Only at a weight of 0.1 for self-pressurization, ethanol obtains a higher score. However as self-pressurization is a critical criterion, a weight of 0.1 is not realistic. Nonetheless, this shows that if in the future ESA decides to include a pressurization system, ethanol would be a good candidate.

4.2. Thrust Chamber

The main objective of this thesis is to design a modular bi-propellant thruster, by creating the architecture such that the injector, the igniter, and the fuel can be changed without drastically having to alter the design of the thruster. This means that as long as the oxidizer (which remains N_2O) is chosen as the coolant, the thrust chamber geometry can remain constant across all the different configurations, and is thus a good starting point for the design. In order to design a thrust chamber, first the theory has to be reviewed, the different key parameters have to be set, and an optimization based on geometry, material, and propellants has to be performed.

4.2.1. Design

The design of the geometry of the thrust chamber was performed by using the Rocket Propulsion Analysis (RPA) software (Ponomarenko, 2010). This software utilizes the ideal rocket motor theory described in the previous chapter

together with propellant thermodynamic data and empirical relations to optimize the main chamber geometry. RPA also has a built-in regenerative cooling model, however this model was not used in this thesis. Another open-source regenerative cooling python model was used, since it was found that the RPA model would occasionally give errors. This model, called Pyrocket (Neeser, 2026), is a transient simulation, while the RPA model is steady-state.

Cooling Method Trade-off

As it was an objective to achieve long duration steady-state firing, choosing a cooling method is one of the most crucial components. Thus, initially a trade-off was performed between the cooling methods specified in section 2.3, and after this trade-off, simulations were performed using the cooling method. The ratings for the criteria have been give qualitatively, as the cooling methods do not always have to be seen separately, but can be combined with other cooling methods. The trade-off is rather a starting point in the initial design rather than a definitive cooling method selection.

Table 4.2: Cooling method trade-off for a 20 N $N_2O-C_2H_6$ thruster (qualitative).

Method	**Steady-state capability**	**Complexity**	**Manufacturability**	**Perf. impact**	**Life/ reuse**	**Notes/Scoring Justification**
Regenerative	++	0	-	+	++	Regenerative cooling can be done with N_2O or the chosen fuel. With additive manufacturing being more readily available and less costly, the manufacturability is not very unfavourable. For steady-state firing, this is one of the most common options in recent propulsion developments. Also, highly reusable and negligible performance impact, apart from the hot gas injection into the combustion chamber.
Radiation	0	++	+	++	+	Another very common method for engines that do not necessarily want to achieve steady-state, but rather prolong its lifetime. Complexity is low and manufacturability is relatively easy. No performance impact. Can be used in combination with regenerative cooling.
Heat-sink	- -	++	+	++	+	The most basic option, essentially no cooling, but using a material with a high thermal conductivity can allow for short pulses, leaving time in between for the material to cool down.
Ablative	++	++	++	+/-	- -	Good for long fires, but needs to be reapplied after a specific number of firings, making it not a good option for space propulsion. However, for sea-level firings it could be used. But does bring extra verification steps and has some impact on performance.
Film cooling	+	+	+	-	+	Usually used in combination with another cooling method, film cooling on its own is not sufficient for steady-state firing. Also fairly complex to implement and has less cooling impact when the coolant is already in gaseous state.

Table 4.2: Cooling method trade-off (continued)

Method	Steady-state capability	Complexity	Manufacturability	Perf. impact	Life/ reuse	Notes
Transpiration	++	- -	- -	0	+	Could be used for steady-state firing however very complex and hard to manufacture. Performance impact depends on the desired O/F distribution.

Rating legend: ++ very favourable, + favourable, 0 neutral/depends, - unfavourable, – very unfavourable.

From this trade-off there are multiple cooling methods that provide good options. However, apart from regenerative cooling, radiation cooling and film cooling, the other methods each have (at least) one major downside that makes them not suitable for this thruster. Heat-sink cooling could not survive a steady-state fire, and is thus unsuitable as this is an objective in this thesis. Ablative cooling is not reusable (at least not for pulse-mode firing) and as this is a main objective, it is also unsuitable. Transpiration cooling is discarded due to its high complexity. Radiation cooling could also be explored, however with a small thruster, achieving thermal steady-state would be very difficult. Film cooling is an option, however as a standalone method it would most likely be very difficult to obtain steady-state firing. Thus, while regenerative cooling is not necessarily clearly the best option, it at least scores sufficiently in each area to proceed with the design. Furthermore, if simulations and/or firings with the first design would result in less than favourable results, a method like film cooling or ablative cooling could still be used at a later point, especially since the design is modular.

Material Trade-off

Following from the cooling method, a material must be chosen that allows for regenerative cooling, is compatible with the coolant, can withstand high (thermal) loads, is manufacturable and not too costly. To achieve regenerative cooling, a few material properties are important. These are, thermal conductivity k [$\mathrm{W m^{-1} K^{-1}}$], heat capacity C_p [$\mathrm{J kg^{-1} K^{-1}}$] and emissivity ϵ [-]. Similar to the cooling method trade-off, the trade-off for the thrust chamber material is rather a guideline than a definitive material selection, as simulations of the thruster with different materials will give a more explicit comparison of which material performs the best using regenerative cooling.

Table 4.3: Material trade-off for regeneratively cooled 20 N N_2O/C_2H_6 thruster (N_2O as coolant).

Material	Thermal cond.	High-T strength	N_2O compat.	AM cap.	Life	Cost
ABD900AM	0	++	++	++	++	-
IN718	0	++	++	+	++	0
GRCop-42	++	+	++	++	+	-
CrCuZr	++	+	-	+	+	0
Ti-6Al-4V	-	+	0/+	++	0	+
Copper	++	-	- -	0	-	++
AlSi10Mg	-	-	0	++	-	++

Rating legend: ++ very favourable, + favourable, 0 depends, - unfavourable, – very unfavourable.

This table shows that there are a couple of good options for the material choice. In the following initial design calculations and simulations, the following materials were selected and compared:

- ABD900AM
- IN718
- GRCop-42

These materials are all compatible with N2O, and have either good strength at high temperature, or high thermal conductivity.

Initial Design Process

The initial design of the thrust chamber was done using a specific iterative design process. First, a chamber geometry was generated with RPA using the values in Table 4.4 as fixed inputs. These values were based on stakeholder requirements, general engineering knowledge and online resources/literature. Regarding the selected geometries, firstly the contraction angle was determined based on Huang and Huzel, 1992, which specify a contraction angle between 20 and 45. According to Sutton and Biblarz, 2016 a optimum value for the conical nozzle half angle is 15. However this was slightly increased to 20 in order to make the nozzle shorter and improve cooling. For the convergent radius ratio Huang and Huzel, 1992 was consulted. The divergent entrance ratio is a value set by RPA itself, and can be considered optimum (Ponomarenko, 2010). The throat downstream radius ratio was chosen based on the rao optimum nozzle method (Rao, 1958). The dimension locations can be seen in Figure 4.2.

Table 4.4: Fixed design values

Parameter	Value	Unit
Thrust (F)	20	N
Exit pressure (p_e)	1	atm
Oxidizer	N_2O	-
Contraction Angle (b)	30	°
Conical nozzle half angle (T_e)	20	°
Convergent Radius Ratio (R_1/R_t)	1.5	-
Divergent Entrance Ratio (R_2/R_{2max})	0.500	-
Throat Downstream Radius Ratio (R_n/R_t)	0.382	-

It was decided to have a conical nozzle, as this would improve manufacturability and modelling. Also, it was found that for very small engine such as this one, there is very limited improvement between a bell nozzle and a conical nozzle (Arrington et al., 1996). Furthermore, as this engine does not need to be weight optimized, a bell nozzle is not necessary.

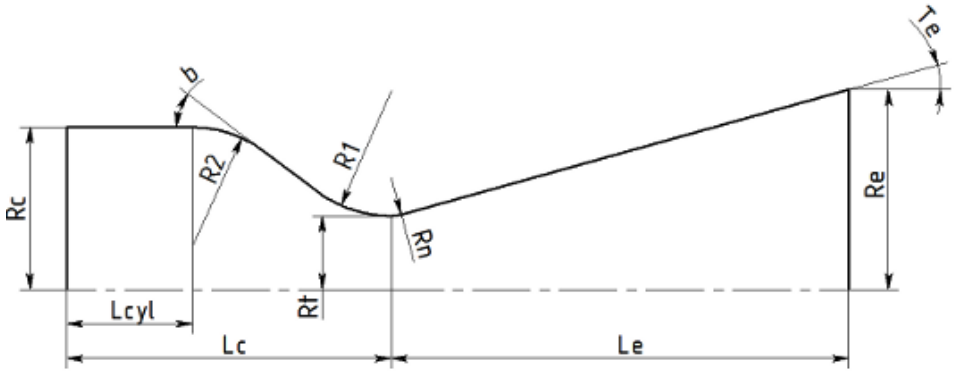

Figure 4.2: Rocket Propulsion Analysis general geometry

With these fixed inputs, a geometry was generated using initial values for chamber pressure, contraction area ratio, fuel (from the fuel trade-off) and O/F ratio. This geometry together with generated parameters like mass flow, O/F, chamber pressure, one of the materials from the material trade-off, and most importantly the cooling channel geometry, were then inserted into the PyRocket regenerative cooling simulation tool, which showed various outputs. The two key objectives were minimizing the maximum inner wall temperature, to avoid structural failure and minimizing the maximum coolant temperature, to avoid decomposition in the cooling channels. This optimization process will be discussed in the next section.

If an optimized geometry was found for a given material, fuel, O/F, chamber pressure and mass flow, another custom-made python tool would be used to estimate the stress in the wall. This tool uses the pressures of the coolant channel and combustion chamber pressure with the chamber geometry to give a rough estimation of the hoop stress as well as the thermal stress, using the highest ΔT in the simulation as input as well as the material properties.

If after these two steps the design showed sufficiently low temperatures and stresses, a CAD model was made, and the design was further verified using CFD and FEM, which will be discussed in section 6.3. A full illustration of the design process/cycle can be seen in Figure 4.3.

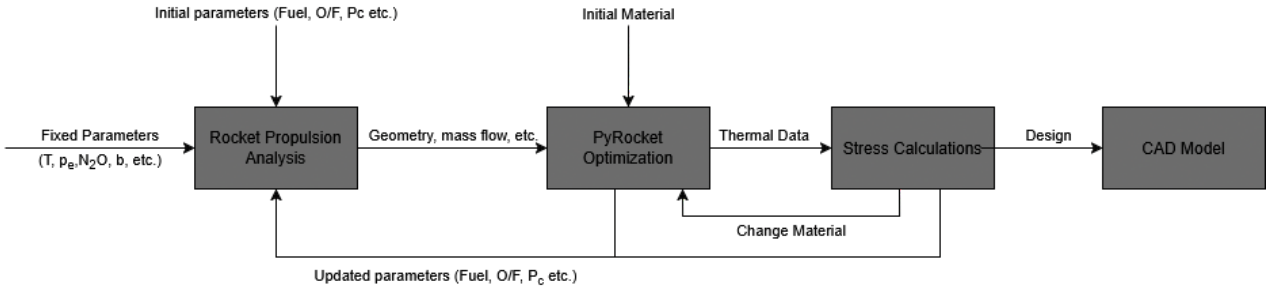

Figure 4.3: Design optimization cycle

PyRocket Optimization

As was stated before, an open-source python software tool called PyRocket was used during the design process in order to optimize the chamber geometry. PyRocket is a thermal simulation tool that can be used for regeneratively cooled liquid rocket engine thrust chambers. It utilizes emperical relations for heat transfer based on the Nusselt number (which were shown in subsection 2.3.1) to determine the chamber wall temperature distribution. This is done by creating a 2D transient thermal simulation that is based on a finite volume method. This 2D simulation is then repeated for a specific number of sections along the axial length of the chamber. The simulation then creates multiple outputs, namely a distribution of the temperature along the section geometry for each section along the axial length, and other parameters like the heat transfer coefficient for the coolant and the flame, the heat flux due to convection and radiation, the coolant pressure, the Reynolds number and the temperature, all plotted along the axial length of the combustion chamber. PyRocket has been validated using existing experimental data from 22 N N_2O/hydrocarbon thrusters (Neeser, 2026).

PyRocket by itself does not have any optimization feature, and rather simply takes a single geometry as an input, together with other parameters, which can be seen in Table 4.5.

Table 4.5: PyRocket Input Parameters

Parameter	Symbol	Unit
CEA & Operating Point		
Fuel Selection	-	N.A.
Oxidizer Selection	-	N.A.
Hot Gas Method	-	N.A.
C* Efficiency	η_{c^*}	N.A.
Mixture Ratio	MR	N.A.
Total Mass Flow	$\dot{m}$	kgs^{-1}
Fuel Mass Flow	$\dot{m}_f$	kgs^{-1}
Oxidizer Mass Flow	$\dot{m}_{ox}$	kgs^{-1}
Chamber Pressure	P_c	Pa
Coolant Input		
Cooling Fluid	-	N.A.
Fluid Mass Fraction	w_i	N.A.
Coolant Mass Flow	$\dot{m}_{cool}$	kgs^{-1}
Inlet Temperature	T_{in}	K
Inlet Pressure	P_{in}	Pa
Cooling Method	-	N.A.
Ambient Temperature	T_{amb}	K

Parameter	Symbol	Unit
Chamber Geometry		
Chamber Diameter	D_c	m
Throat Diameter	D_t	m
Exit Diameter	D_e	m
Cylindrical Length	L_{cyl}	m
Conv. Section Radius	R_1	m
Throat Conv. Radius	R_2	m
Throat Div. Radius	R_n	m
Convergence Angle	ϕ_{conv}	°
Divergence Angle	ϕ_{div}	°
Exit Angle	ϕ_e	°
Step Size	Δx	m
Wall Material	-	N.A.
Cooling Channel Geometry		
Number of Channels	N	N.A.
Channel Height	H_c	m
Fill Factor	ψ	N.A.
Inner Wall Thickness	$t_{w,i}$	m
Outer Wall Thickness	$t_{w,o}$	m

In Figure 4.4, the section of the thrust chamber wall and cooling channels can be seen. It should be noted that,

as can be seen in the drawing, PyRocket only calculates the heat transfer and resulting temperature in half of the cooling channel and combustion chamber wall (between cooling channels) in order to reduce computational time. It then assumes symmetry in order to obtain the other half. This is then multiplied with the amount of cooling channels, resulting in a full chamber 2D thermal simulation. This method does bring a disadvantage that injection is not simulated, and this tool does not take into account local hot spots which can occur for some injector types. That is why it is crucial to verify the design further using a 3D CFD simulation.

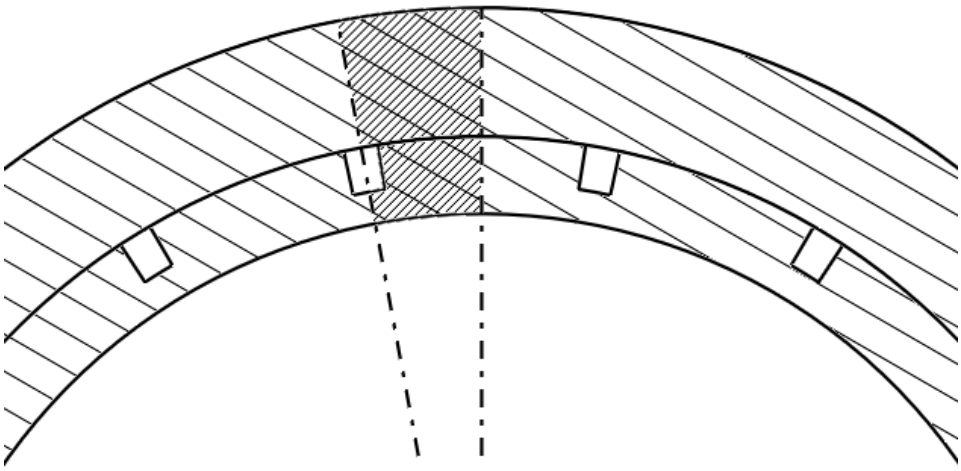

Figure 4.4: PyRocket 2D section

Furthermore, PyRocket uses an adaptive timestep method in order to solve the transient simulation. To improve convergence, the following settings could be adjusted:

Table 4.6: 2D Section Simulation Settings

Parameter	**Default Value / Expression**
Cell Size	$0.15 \cdot t_{w,i}$
Time Step	$(\text{cell\_size})^2/(\text{material}.\alpha)$
Adaptive Time Step Factor (Up)	1.4
Convergence Tolerance	1×10^{-2}
Maximum Iterations	300

To perform the optimization, a custom wrapper code was developed which allowed for variable inputs of the parameters in Table 4.7. Also, certain necessary changes were made in the original code in order for the code to allow having variable inputs during the run. Furthermore, as the code is a transient simulation and thus has a runtime per configuration of at least a few minutes (sometimes longer depending on the configuration settings), a python multiprocessing module was implemented in order to run multiple configurations at the same time.

Table 4.7: Variable Parameter Inputs

Parameter	**Symbol**	**Unit**	**Range**
Cooling Channel Height	H_c	m	0.5 mm - 1.5 mm (0.25 mm steps)
Number of Cooling Channels	N	-	13 - 17 (steps of 1)
Material Selection	-	-	ABD900AM, GRCop42, IN718
Cooling Channel Width	w_c	m	0.5 mm - 1 mm (0.25 mm steps)
Mixture Ratio	MR	-	7.5 - 9 (0.5 steps)

For each of these variables inputs, a range was specified as can be seen in Table 4.7. This range was decided by means of propellant selection in the trade-off and optimum mixture ratio for the propellants. Furthermore, the

cooling channel dimensions were decided based on results from previously performed test runs, where the range was made as large as possible while still retaining a relatively short runtime. When the code was run, the wrapper would (in parallel if specified) run the PyRocket simulation for each of the different possible configurations. Once all the configurations finished running, the code would save the results to a specific folder, and present the following outputs for each run in a csv file; average heat flux, average wall temperature, maximum coolant temperature, maximum wall temperature and the minimum Reynolds number. Also, the graphs and figures specified before are generated in a separate folder for each different configuration. Finally, the output in the terminal can be seen in Listing 4.1. In this version of the wrapper, the "best configuration" was solely based on which configurations has the lowest maximum wall temperature, as this was deemed the most important factor. However, a recommendation would be to include other parameters as well for a more accurate result.

Listing 4.1: Example terminal output of single configuration inside an optimization run.

```
Starting parametric sweep with 1 combinations...
Using 6 processes
Parameters: ['h_c', 'n_channels', 'material', 'propellant', 'w_channel', 'MR', 'L_cyl']
Isp: 239.03 s, for fuel: ethane, at MR: 9, with material: ABD900AM
Running simulation with parameters: {'h_c': 0.001, 'n_channels': 17, 'material': 'ABD900AM', 'propellant': '
    ethane', 'w_channel': 0.00025, 'MR': 9, 'L_cyl': 0.05428}
Completed 1/1
Parametric sweep completed in 126.10 seconds
Savng results...
Saving parametric sweep results to optimization_results//run_71\parametric_sweep_20260205_092254.csv...
Parametric sweep results saved to: optimization_results//run_71\parametric_sweep_20260205_092254.csv
Results saved in 0.00 seconds
Best configuration found:
  Channel height: 1.00 mm
  Number of channels: 17
  Max. wall temperature: 977.6 K
  Material: ABD900AM
  Propellant: ethane
  Channel width: 0.5 mm
  Oxidizer-to-fuel ratio: 9
```

After the optimization was performed and a final geometry was selected, some simple thermostructural calculations were performed in order to have an estimation of the structural integrity of the thruster. These calculations were performed using python, where a short code was written that implemented the structural theory from subsection 2.3.2. The stress outputs of these calculations were then compared with the yield strength of the material at the specific temperature. In order to find the point of the highest stress in the combustion chamber, the location with the highest temperature gradient in the wall needs to be found. Fortunately, the thermal analysis code also generates thermal cross-sections of the wall from each chamber section, as well as a temperature graph along the chamber wall. These can then both be used to find the highest temperature gradient in the thrust chamber. The full list of inputs can be found in Table 4.8.

Table 4.8: Parameter Inputs (including ABD-900AM Properties)

Notation	Name	Unit
P_{co}	Coolant pressure	Pa
P_g	Chamber (gas) pressure	Pa
r	Chamber radius	m
t	Wall thickness	m
q	Heat flux	$\mathrm{W\,m^{-2}}$
T_{firewall}	Firewall temperature	°C
$T_{\text{coolant\_side}}$	Coolant-side wall temperature	°C
M_A	Discontinuity bending moment	$\mathrm{N\,m\,m^{-1}}$
ρ	Material density	$\mathrm{kg\,m^{-3}}$
k	Material thermal conductivity	$\mathrm{W\,m^{-1}\,K^{-1}}$
α	Material coeff. of thermal expansion	$\mathrm{K^{-1}}$
E	Material Young's modulus	Pa
ν	Material Poisson's ratio	-
S_y	Material yield strength	Pa
S_u	Material ultimate tensile strength	Pa

When the code is run, the following generic results can be seen. The results for the selected configuration will be shown in section 6.1.

Listing 4.2: Generic terminal output of stress calculations.

```
======================================================================
COOLING CHANNEL STRESS ANALYSIS RESULTS
Material: ABD-900AM Nickel Superalloy
======================================================================

STRESSES:
  Tangential Stress (Hoop):        387.26 MPa
  Longitudinal Stress (Thermal):   44.06 MPa
  Von Mises Equivalent Stress:     595.83 MPa
  Critical Buckling Stress:        8149.32 MPa

MATERIAL PROPERTIES AT WALL TEMPERATURE:
  Yield Strength:                  932.26 MPa
  Young's Modulus:                 116.00 GPa
  Thermal Conductivity:            21.57 W/(m C)
  Thermal Expansion Coefficient:   1.56e-05 1/C
  Average Wall Temperature:        675.0 C

SAFETY MARGINS:
  Tangential Stress:               2.41
  Longitudinal Stress:             21.16
  Von Mises Stress:                1.56
  UTS (Longitudinal Stress):       27.64

 Safety margins are acceptable.
======================================================================
```

4.3. Injector

Once a design for the thrust chamber was found, the next key component was the injector. As one of the thesis objectives was to have a modular injector design, multiple injector designs were selected based on the trade-off that was performed. In contrast to some of the previous trade-offs, since this time the trade-off is not a guideline but a definitive injector type selection, a quantitative trade-off was performed. Based on the literature study that was done, different injector types were considered for the trade-off. One of the main challenges found with a small-scale thruster is that the combustion chamber diameter is very small. Thus, when deciding on an injector, not all configurations were viable, since it would not be able to fit inside the chamber. Also, since the propellants are not hypergolic, an igniter would also be placed inside the manifold, reducing the available space for the injectors (depending on the

igniter type and size).

For the trade-off, there were a few criteria that were deemed most important. Firstly the manufacturability, if the injector has complex shapes or would need to be made out of multiple parts, this was scored lower. Secondly, the mixing or atomization, if previous designs and injectors design handbooks (like Gill and Nurick, 1976) showed that the required residence time (so a short L*) was sufficient for proper mixing and combustion, this was scored higher. For the stability injector design, handbooks were also used. A higher stability score meant the injector is less likely to cause instabilities, such as chugging. The complexity criterion was mainly related to what was mentioned before, that the injector should be able to fit in the combustion chamber together with the igniter. If complexity scored lower, this was deemed to be more difficult to achieve. The heritage criterion showed how much research was performed on the injector type, and how much (public) knowledge was available to assist with the design process.

Table 4.9: Injector Trade-off

Injector Type	**Manuf.**	**Mixing/ Atom.**	**Stability**	**Complexity**	**Heritage**	**Weighted Total**
Weight	*0.20*	*0.25*	*0.15*	*0.15*	*0.25*	—
Coaxial Swirl	6	9	8	6	6	**7.05**
Unlike Impinging	7	8	5	7	9	**7.45**
Like Impinging	7	6	6	8	8	**7.00**
Pintle	5	8	9	4	5	**6.20**
Showerhead	9	3	4	9	7	**6.25**
Porous Injector	7	9	5	6	2	**5.80**

Rating legend: 0 (worst) – 10 (best). Weighted total = $\sum w_i \cdot s_i$ (max 10).

Below the justification is presented for each criterion.

Manufacturability shows machining complexity and number of parts. Simple designs with straight drilled orifices score highest (showerhead: 9). Designs requiring angled orifices and complex manifolds score 7 (unlike/like impinging, porous injector), those requiring internal passages score 6 (coaxial swirl), and designs requiring high grade materials and low-tolerance machining score lowest (pintle: 5).

Mixing / Atomization shows expected propellant mixing quality at the operating conditions, based on injector design handbooks (Gill and Nurick, 1976) and the short L^* requirement of this combustion chamber. Swirl-based and distributed injection designs that produce fine droplets contact score 9 (coaxial swirl, porous injector). Direct unlike-propellant impingement scores 8 (unlike impinging, pintle). Like-impingement, which relies on spray fans merging downstream (difficult in small combustion chambers), scores 6. Showerhead injection, which depends almost entirely on diffusion inside the chamber, scores 3.

Stability shows sensitivity to combustion instabilities based on known characteristics in the literature. The pintle scores 9 for its well-documented damping. Coaxial swirl scores 8 due to its tangential momentum stabilizing the combustion. Like impinging scores 6 for moderate stability, while unlike impinging and porous injectors score 5 due to the possibility of having feed-system coupling if not properly sized. Showerhead scores 4 as there is no atomization or momentum coupling to reduce oscillations.

Complexity shows compatibility with the small chamber diameter and available space while keeping the igniter in mind. Flat-plate designs are concise and the design is flexible, meaning an igniter can fit in the middle (showerhead: 9), doublet configurations without a central element score 8 (like impinging) to 7 (unlike impinging), swirl and porous designs that reduce usable area near the igniter score 6, and the pintle's central element, which directly clashes with igniter placement, scores 4.

Heritage shows the volume of publicly available design data and demonstrated performance. Unlike impinging injectors are the most extensively documented in open literature and handbooks (9), followed by like impinging (8), showerhead (7), coaxial swirl with limited small-scale thruster usage (6), pintle with limited public data using small-scale thrusters (5), and porous injectors which are still experimental (2).

From this trade-off, it could be concluded that unlike impinging would be the best injector type. However, to show the modularity of the system, it was also decided to have a configuration with the coaxial swirl injector, since this type also showed promising results in terms of mixing and stability. In the next subsections, the design process of both injectors will be elaborated on.

4.3.1. Sensitivity Analysis

Similarly to the fuel trade-off, a sensitivity analysis should be performed on the quantitative injector trade-off. The method is exactly the same, and with this the following results were found.

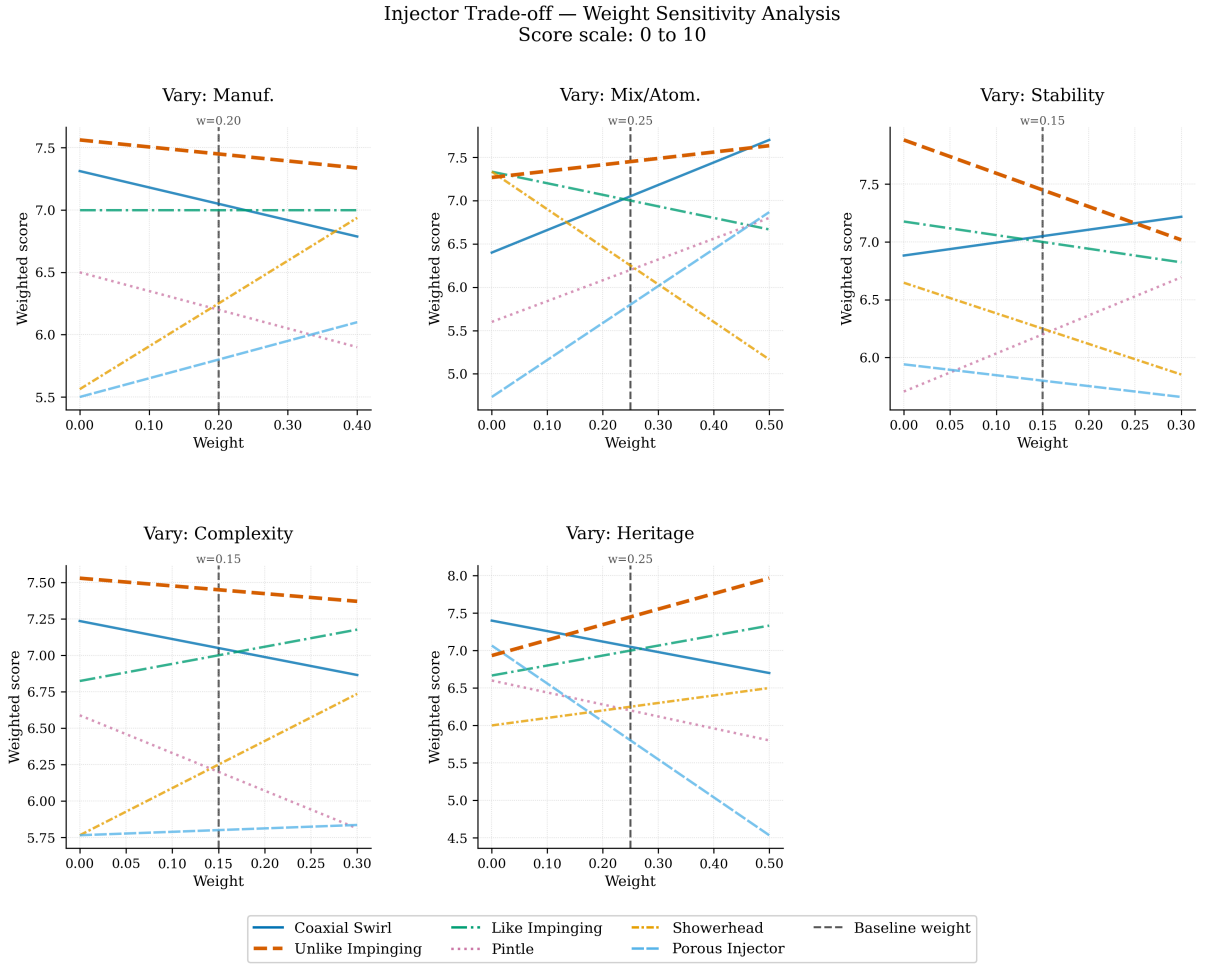

Figure 4.5: Injector sensitivity analysis

From this analysis, it can be seen that in most cases the unlike impinging injector is the best option. In some cases the coaxial swirl injector obtains a higher score, however as this design will also be explored in this thesis, it is not a point of concern.

4.3.2. Unlike Impinging Injector

For unlike impinging injectors, generally two types are considered, namely triplets and doublets. As the stoichiometric oxidizer-to-fuel ratio for combustion of nitrous-oxide with a hydrocarbon is generally high (8-9 as could be seen in Figure 2.3), triplets are desired for better mixing. A typical layout of a single triplet injector element can be seen in Figure 4.6.

First of all, the central fuel injector is considered completely vertical, and thus the flow has no angular momentum. The total angle between the two oxidizer streams is a design input, and according to Gill and Nurick, 1976, the most optimal range lies between 45° and 90°. Going lower than 45° would make the impinging point too much forward,

resulting in bad mixing and a long residence time. For a small thruster this would be a major issue. However, it is also not advisable to have an angle of more than 90° as this would result in very high heat fluxes near the injector face. In the end, a collision angle of 60° was chosen.

After selecting the injector collision angle, the size of the orifices and the amount of elements needs to be calculated and decided. In general, the rule-of-thumb is that the more orifices, the better. As such, the design process included calculating the orifice sizes for a specific amount of elements, checking the manifold configuration (if it would fit) and redoing the process if this was not the case, with the goal of trying to fit in as many elements as possible, while keeping the injector manifold manufacturable. The size of the orifices was calculated with the following equation:

$$R_{orifice} = \sqrt{\frac{\dot{m}_{elem}}{\pi C_D \sqrt{2\rho\Delta P}}} \tag{4.1}$$

Where,

$R_{orifice}$ = Orifice radius [m]
$\dot{m}_{elem}$ = Mass flow rate per element [kgs^{-1}]
C_D = Discharge coefficient [−]
ρ = Propellant density [kgm^{-3}]
ΔP = Pressure drop [Pa]

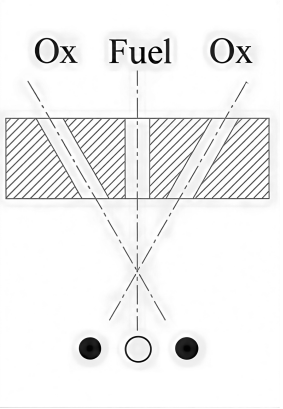

Figure 4.6: Triplet injector (Xie et al., 2024)

However, to solve this equation, the discharge coefficient, the pressure drop and the density need to be either calculated or estimated based on previous designs and design handbooks. For the discharge coefficient, Figure 4.7 was used for an estimation. Here, depending on the smoothness of the orifice, an estimation of the discharge coefficient is given.

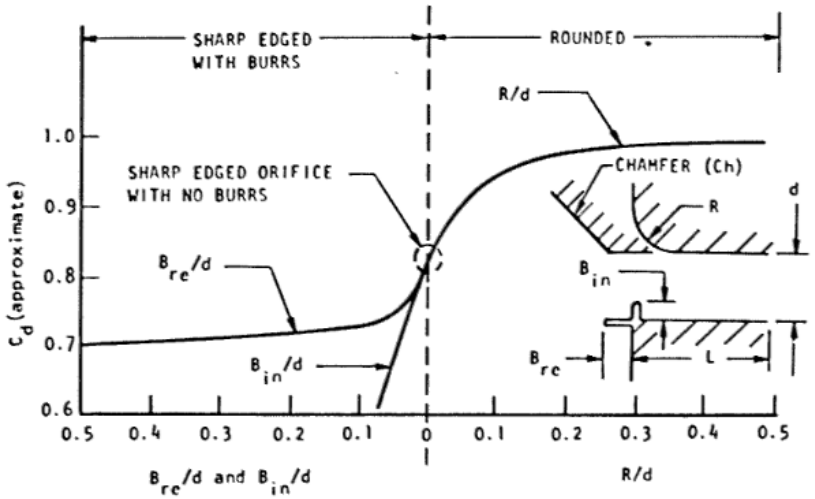

Figure 4.7: Discharge coefficient as a function of orifice inlet geometry (Gill and Nurick, 1976)

As it was opted for additively manufacturing the triplet injector integrated into the manifold, a conservative estimation would put the C_d between 0.7 and 0.8. This is the case as additive manufacturing will never create a perfectly smooth rounded surface, and post-processing (especially internally) is difficult.

As a good estimate of the pressure drop, it is generally advised to keep the value between 10 and 20 percent of the chamber pressure, in order to avoid stability issues (Tucker et al., 2000). For this design 20 percent was used. To determine the density, the ideal gas law can be used for the initial design. Here, it should be noted that for the density of (gaseous) nitrous-oxide the temperature at the exit of the cooling channels should be used.

$$p = \rho RT \tag{4.2}$$

Where,

p = Absolute pressure [Pa]

ρ = Density [kg m^{-3}]

R = Specific gas constant [J kg^{-1} K^{-1}]

T = Absolute temperature [K]

Lastly, the position of the elements should be chosen. For the distance between the elements, this is dependent on the ratio of the so-called free-stream jet length L_{fs} and the orifice diameter d_{or}. Generally a L_{fs}/d_{or} between five and seven would give the best mixing results and the least misimpingement (Gill and Nurick, 1976). Based on the chosen value and the chosen impingement angle, the distance between the elements could be calculated.

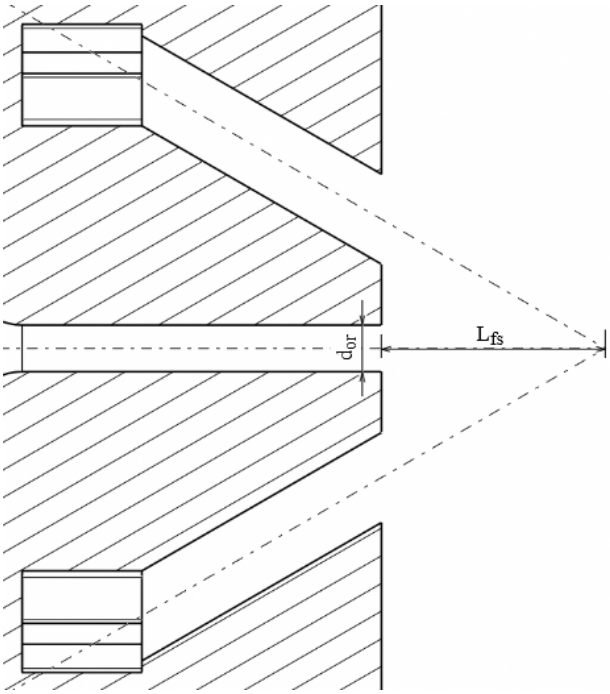

Figure 4.8: Free stream jet length and orifice ratio dimensions

4.3.3. Coaxial Swirl Injector

The design of the coaxial swirl injector has been performed with two different configurations in mind. As generally the size of a coaxial swirl injector (relative to the chamber diameter of a 20 N thruster) is quite big, it is crucial to involve the size of the igniter into the design of the coaxial swirl injector. That is why it was decided to have two configurations, in order to see the difference between these configurations. The first configuration consists of a single “regular” coaxial swirl injector that is off-center, in order to have space for the igniter. The second configuration is a central bigger coaxial swirl injector, with an igniter in the middle. For illustration purposes both injector types/configurations can be seen in Figure 4.9 and Figure 4.10.

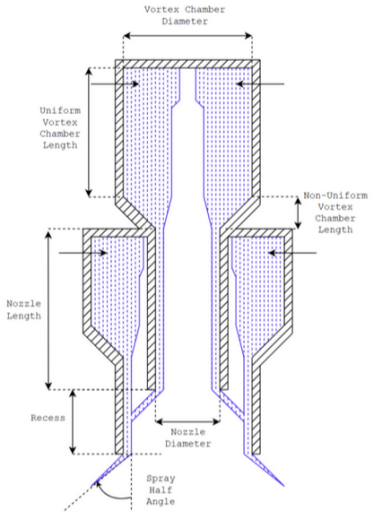

Figure 4.9: Regular coaxial swirl injector.

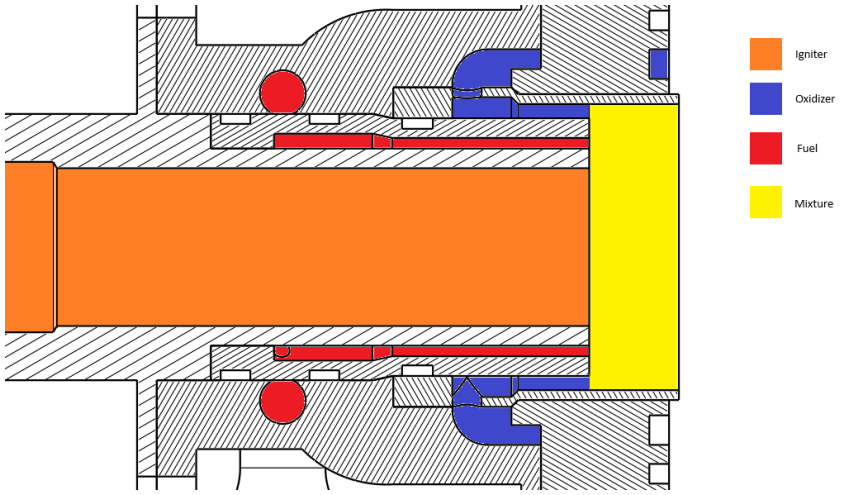

Figure 4.10: Coaxial swirl injector with integrated igniter

Figure 4.11: Side-by-side comparison of the injector assembly schematic and colorized cross-section views.

For the design of the swirl injector elements, the book Design and Dynamics of Jet and Swirl Injectors was used (Bazarov et al., 2004). Before the start of the design, the following parameters are known:

- Mass flow $\dot{m}$ for both stages
- Desired pressure drop Δp (typically between 15-20 percent of p_c (Ahn and Lee, 2019)
- Propellant properties (viscosity, molar mass etc.)

A swirl injector has two stages, one for each propellant. Both stages can be either open-ended or close-ended. In general, close-ended stages allow for better swirling and mixing, while open-ended stages have a higher axial momentum (Kumar et al., 2025). An illustration of all three versions can be seen in Figure 4.12.

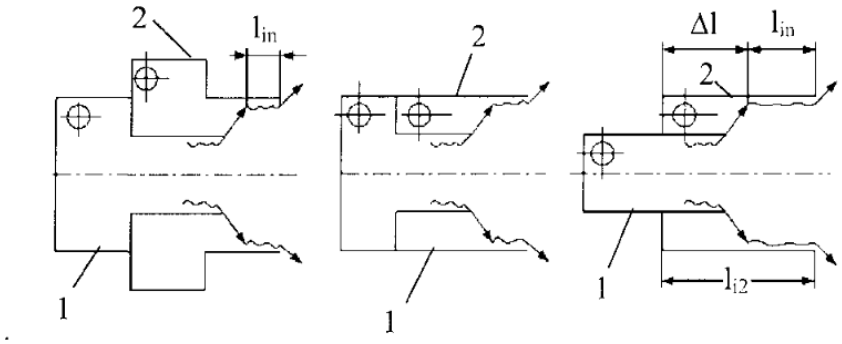

Figure 4.12: Versions of bi-propellant swirl injectors with internal mixing (Bazarov et al., 2004).
From left to right: both stages close-ended – stage 1 closed/stage 2 open – both stages open-ended

As the thruster is small, good mixing is desired above a higher axial velocity. Thus, it was decided to use a coaxial swirl injector with both stages close-ended. In addition to the known incoming flow properties, the following parameters should be chosen:

Table 4.10: Design Parameters for bi-propellant swirl injectors

No.	Parameter	Symbol	Recommended Value / Range (Bazarov et al., 2004)
1	Coefficients of nozzle opening	$\bar{R}_{in1}, \bar{R}_{in2}$	3 (closed); 0.7–0.8 (open)
2	Relative nozzle lengths	$\bar{l}_{n1}, \bar{l}_{n2}$	1.0
3	Number of inlet passages	n_1, n_2	2–6
4	Spray cone angle of stage 1	$2\alpha_1$	60°–80°

For these parameters the following values were decided on. For the coefficients of nozzle opening the value of 3 was taken, as is the recommended value for a closed-ended swirl injector. For the relative nozzle lengths a value of one is taken. For the inlet passages, four inlet passages were used for the central fuel element, and six inlet passages for the oxidizer element. This was done as the oxidizer mass flow is significantly higher. After a design iteration based on manufacturability, for the off-center coaxial swirl injector design the amount of inlet passages of the outer oxidizer element was changed to five. For all designs a spray cone angle of 70° was used. After the design parameters were set, the geometric characteristic parameter A was determined from Figure 4.13.

The coefficient of passage fullness is the ratio of the area filled by fluid to the total area, and with A known, it can be determined with the following equation:

$$A \equiv \frac{R_N(R_V - R_T)}{nR_T^2} = \frac{(1-\varphi)\sqrt{2}}{\varphi\sqrt{\varphi}} \tag{4.3}$$

Following from that, the flow coefficient or discharge coefficient can be determined:

$$\mu = \sqrt{\frac{\varphi^3}{2-\varphi}} \tag{4.4}$$

After this, calculate the nozzle radius for stage 1:

$$R_{n1} = 0.475\sqrt{\dot{m}_1/(C_D\sqrt{\rho_1 \Delta p_{i1}})} \tag{4.5}$$

And the inlet radius:

$$r_{in1} = \sqrt{R_{in1}R_{n1}/(n_1 A_i)} \tag{4.6}$$

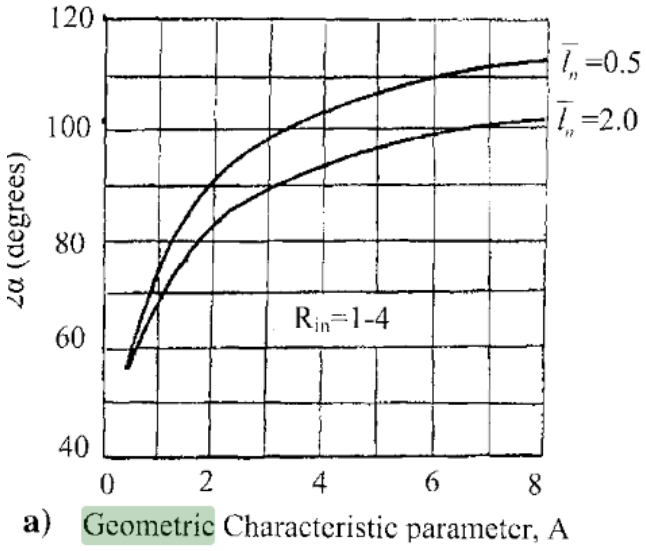

Figure 4.13: Experimental plots of spray cone angle 2α (Bazarov et al., 2004)

Where,

R_{n1} = Nozzle radius [m]

$\dot{m}_1$ = Mass flow rate [kg s^{-1}]

C_D = Discharge coefficient [−]

Following this, the lengths of the tangential passages should be calculated using the following equations:

$$l_{in1} = (3\text{–}4)\,r_{in1}, \quad l_{n1} = 2R_{n1}, \quad l_{s1} = (2\text{–}3)\,R_{in1} \tag{4.7}$$

Where,

l_{in1} = Length of the tangential passages [m]

r_{in1} = Radius of the tangential inlet ports [m]

l_{n1} = Length of the nozzle [m]

l_{s1} = Length of the vortex chamber [m]

R_{in1} = Radius of the vortex chamber [m]

Finally, the external radius of the nozzle should be calculated:

$$R_1 = R_{n1} + \delta_w \tag{4.8}$$

For determining the dimensions of stage 2 the following steps have to be taken.
First, the permitted gas-vortex radius r_{m2} has to be calculated:

$$r_{m2} = R_1 + 0.3mm \tag{4.9}$$

Then the assumption is made that $R_{n2} = r_{m2}$ and the discharge coefficient is calculated using:

$$C_D = \frac{0.225\dot{m}_{i2}}{(R_{n2})^2\sqrt{\rho_2 \Delta p_{i2}}} \tag{4.10}$$

After this, A can be determined again using Figure 4.13. After this, a new r_m can be determined from Figure 4.14

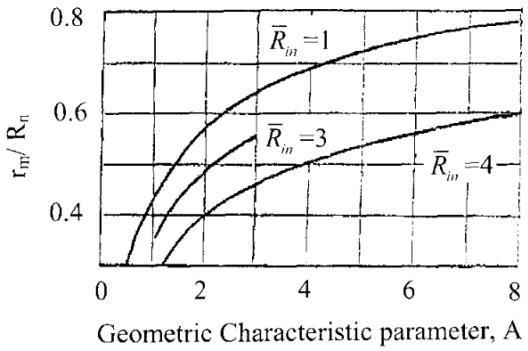

Figure 4.14: Experimental plot of relative liquid vortex radius in vortex chamber as function of geometric parameter of swirl injector (Bazarov et al., 2004).

With this new, r_m a new value of R_{n2} can be determined using $R_{n2} = \frac{r_{m2}}{r_{m2}^{(1)}}$, and as such, a new value for the discharge coefficient. These steps should be repeated until R_{n2} converges. Then, R_{in2} and r_{in2} can be determined:

$$R_{\text{in}2} = \bar{R}_{\text{in}2} R_{n2} \tag{4.11}$$

$$R_{\text{in}2} = \bar{R}_{\text{in}2} R_{n2}, \quad r_{\text{in}2} = \sqrt{R_{\text{in}2} R_{n2}/(n_2 A_2)} \tag{4.12}$$

All the calculations before were for a “regular” coaxial swirl injector. For the design of the coaxial swirl injector with a central igniter, the calculations were kept the same, but the nozzle and vortex chamber radii were increased in such a way that the outlet area of the respective stages were kept unchanged.

4.4. Igniter

Regarding the igniter itself, not much design work had to be performed, since this component would be bought off-the-shelf. As such, simply a trade-off had to be performed in order to decide which igniter would be used. In order to show the modularity of the system, two types of igniters would be selected and used. For the weighting the restart/pulse-mode capability was weighted the highest, as it is a stakeholder requirement. Furthermore, complexity/cost and compatibility with N_2O and C_2H_6 are also considered very important criteria. Reliability, volume efficiency and TRL are also important however are weighted lower as a slightly lower value in one of these criteria does not have to be a critical issue. However, reliability is still very significant so it is weighted slightly higher than the other two criteria.

Table 4.11: Igniter Trade-off (Weighted)

Igniter Type	Reliability	Restart	Complexity	Vol. Eff.	N_2O/C_2H_6 Compat.	TRL	Weighted Total
Weight	*0.15*	*0.25*	*0.20*	*0.10*	*0.20*	*0.10*	—
Spark Plug	7	8	9	9	8	9	**8.25**
Spark Torch	9	9	3	4	9	9	**7.30**
Catalytic Torch	6	8	3	4	1	3	**4.40**
Glow Plug	7	7	7	8	6	7	**6.90**
Pyrotechnic	9	0	8	9	9	9	**6.55**
Laser (LIP)	7	8	4	3	8	5	**6.25**

Rating legend: 0 (worst) – 10 (best).

In the following paragraphs the justifications for the scores of each criterion are presented.

Reliability shows the consistency with respect to ignition and durability of the igniter. Spark torches and pyrotechnic igniters, which deliver a high-energy ignition, score highest (9). Spark plugs and glow plugs score 7, as they are reliable but more sensitive to mixture ratio and timing. Catalytic torches and laser igniters score 6/7, being reliable in principle but dependent on specific operating conditions.

Restart / Pulse-mode capability shows the ability to re-ignite on demand, which is a top-level stakeholder requirement. Igniters that can be actuated electrically score highest: spark torch (9), spark plug (8), laser (8), catalytic torch (8), and glow plug (7). The pyrotechnic igniter scores 0, as it is a single use igniter that cannot support pulse-mode operation.

Complexity / Cost shows the easiness of integration, number of components, and unit cost. The spark plug scores 9 as it is a single-part component with no external propellant supply. The pyrotechnic igniter scores 8 due to its simple design, however it requires replacement after each use. The glow plug scores 7, requiring only an electrical supply, but it is usually a longer igniter. The spark torch and catalytic torch both score 3, as they require a dedicated propellant feed system, and additional integration effort outside the scope of this thesis and unsuitable for small thrusters.

Volume Efficiency shows the required volume inside the manifold. Compact single-element igniters that occupy minimal volume score highest: spark plug and pyrotechnic (9), glow plug (8). Designs requiring a torch cavity reduce available space significantly: spark torch and catalytic torch score 4, and the laser igniter, which requires optical access, scores 3.

N_2O/C_2H_6 Compatibility shows chemical compatibility with nitrous oxide and ethane at operating conditions. Purely electrical igniters with no metallic catalysts score 8–9 (spark plug, spark torch, pyrotechnic, laser). The glow plug scores 6 due to uncertainty over the resistance of the heating element sheath to long term flame exposure. The catalytic torch scores 1, as it is designed for monopropellant decomposition and is incompatible with the N_2O/C_2H_6 propellant combination.

TRL shows the maturity of the technology and availability of published performance data. Spark plugs, spark torches, and pyrotechnic igniters are mature, widely used technologies with a TRL of 9. Glow plugs score 7, being commercially available but with limited rocket ignition heritage. Laser igniters score 5, as they remain largely at the research and demonstration stage. Catalytic torches score 3, being largely undeveloped for this specific propellant combination.

From Table 4.11 it can be concluded that there are four options, namely the spark plug, spark torch, glow plug and pyrotechnic igniter. However, the pyrotechnic igniter automatically is discarded as it does not allow for pulse-mode, which is a top-level requirement. Furthermore, the spark torch has good reliability and restart properties, however the complexity and volume efficiency would make it too difficult to implement this igniter into the system, as it would require also a lot of work from the feed system side, which is not in the scope of this thesis. Thus, the spark plug and glow plug igniters were selected for this design. Following this the igniters were selected commercially off the shelf, mainly based on size and availability, but also voltage. The chosen igniters can be found in section 6.1.

4.4.1. Sensitivity Analysis

Similarly to the fuel and injector trade-offs, a sensitivity analysis should be performed for the igniter. Using the same methods as before, the following results can be found:

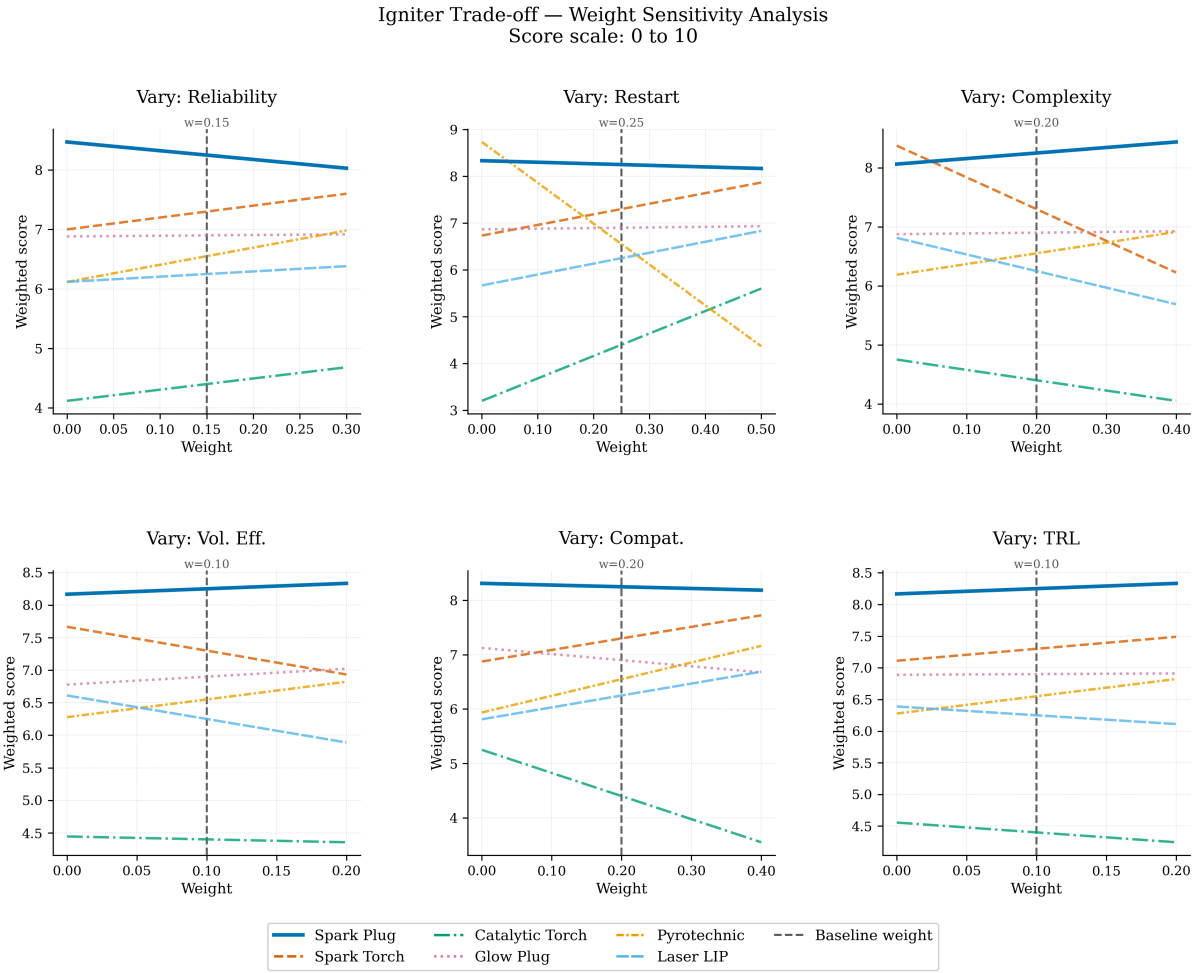

Figure 4.15: Igniter sensitivity analysis

From these results it can be observed that the spark plug is the best option even with varying weighing. Only the pyrotechnic igniter is slightly better if restart capability is not important, and a spark torch if complexity is not an issue.

4.5. Manifold

The manifold is the structural component connecting all the different components (thrust chamber, igniter, injector, and valves) together. This is almost always a custom-made component, and is usually based on structural, manufacturing and fluidic considerations rather than design theory. In this design, the manifold has the following requirements:

[4.5-1] The manifold shall have either a built-in injector or an interface for an external injector component.

[4.5-2] The manifold shall allow for igniter insertion if the (external) injector doesn't allow for it.

[4.5-3] The manifold shall provide an interface for the fuel valve.

[4.5-4] The manifold shall have an interface with the thrust chamber by means of fasteners.

[4.5-5] The manifold shall have internal fluid channels for both the fuel and oxidizer.

[4.5-6] The manifold shall have O-ring grooves wherever sealing is required.

These requirements are additional to the requirements stated in chapter 3. However, as these requirements are not quantitive and solely used during the design process, they are not in the verification control matrix.

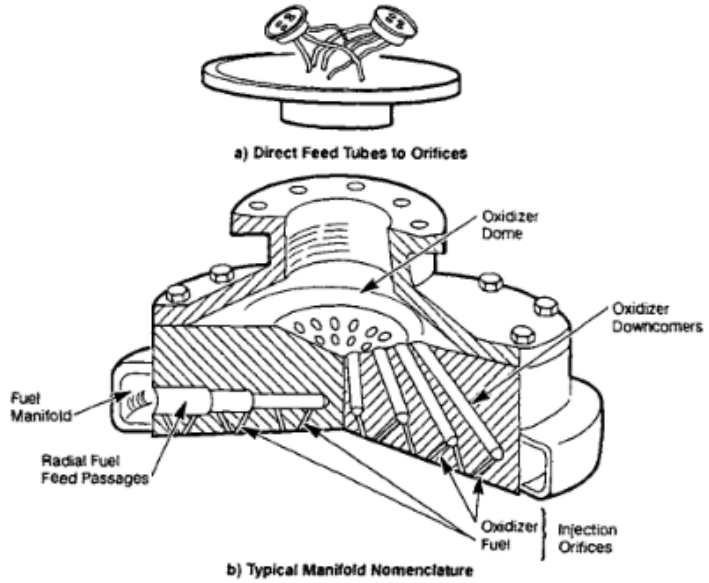

Figure 4.16: Typical manifold (Huang and Huzel, 1992)

4.6. Valves

As the engine will only be used for testing purposes at sea-level, it was decided to use only one valve per propellant instead of two, as redundancy is not absolutely necessary in that case. Furthermore, it was also decided that the valve would be externally sourced, with the means of a specification document. For the valves, there were some crucial criteria that must be met. Firstly, the valve and all of its components had to be compatible with the propellants (N_2O and various hydrocarbons). Secondly, the valves must be able to operate in pulse-mode, with a short actuation response time. Thirdly, the valve had to be leak-tight, and withstand high pressures (MEOP, proof and burst). The exact values and tests that will be performed can be seen in section 5.3. Furthermore, the manufacturing company was provided with a specification document highlighting the main requirements of the valve. This document can be seen in Appendix A.2.

Figure 4.17: Typical pulse valve (Parker, 2016)

As one of the main requirements for this project was the pulse mode capability of the thruster, the valve requirements were tailored to account for this. This includes a response time of 15 ms, and high rate cycling of the valve, both with propellants and without propellants. In order to connect the valves with the thruster assembly, a valve block needed to be designed. Using 4 M2 screws the valve is connected to the valve block, where there are two holes sealed with o-rings, one for the inflow and one for the outflow. Next to these holes there are two threaded connections, namely a 1/8 BSP male thread for the connection with the thruster and the manifold, and a 1/8 BSP male thread to connect with the feed lines from the test bench. A CAD model of the valve block can be seen in Figure 4.18. As the valves are not yet fully designed before the thesis is finalized, the valve block dimensions can still be changed. Thus, no drawing has yet been made.

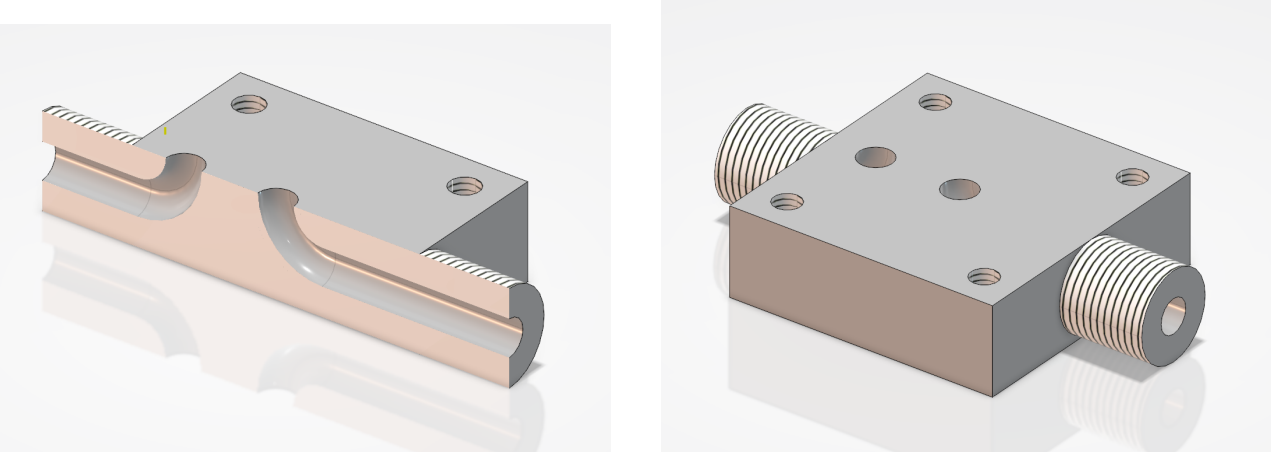

(a) Cross-section view

(b) Isometric full view

Figure 4.18: Valve block

4.7. Design Configurations

For all design configurations, ethane was assumed to be the fuel. However, the design allows for different fuels, if some small changes are made to the injector. In the following sections, the different configurations will first be discussed. Each design uses the same thrust chamber, however the injector, igniter, and manifold differed. In the following sections, the configurations will be shortly discussed, including the reasoning behind them. Furthermore, the CAD models will be shown. As the igniters and valves are outsourced, the CAD models for these components are not included in the assembly.

4.7.1. Off-center Coaxial Swirl Injector and Glow Plug Igniter

The first design configuration includes a coaxial swirl injector and a glow plug igniter, both off-center. This configuration uses a single coaxial swirl injector element. Multiple elements were considered, but due to the size of the engine, and to avoid making the elements too small making them difficult to manufacture, it was opted to use a single element. A 3D model of this configuration can be seen in Figure 4.19.

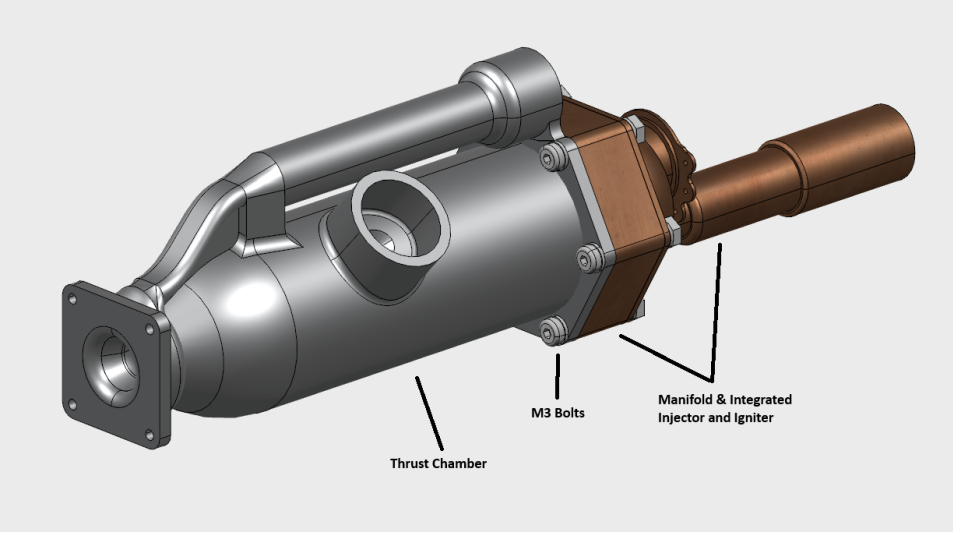

Figure 4.19: Off-center coaxial swirl injector and glow plug igniter configuration CAD model

A downside of using a single element, of which the effect will need to be seen in testing, is that the flow does not

impinge with the flow of any other element, reducing the atomization and mixing across the chamber. Furthermore, an off-center element with a cone shaped outflow could cause a hotspot on the chamber wall location where the propellants mix. Another potential issue that was brought up is that the glow plug and the injector both being off-center could result in an uneven heating of the propellants, reducing the combustion efficiency. For these reasons, a second version of his same configuration was developed. However, to quantify the differences between the two versions, this version will still be developed and tested.

4.7.2. Central Coaxial Swirl Injector and Glow Plug Igniter

The second configuration is identical to the first configuration in terms of components, however the arrangement of the components (specifically the injector and the igniter), is different. Due to the limitations of the uneven propellant heating and potential hot spot of the first configuration as discussed in the previous section, a second configuration was developed which includes a single central coaxial swirl injector element, with an internal glow plug igniter. A 3D model of this configuration can be seen in Figure 4.20.

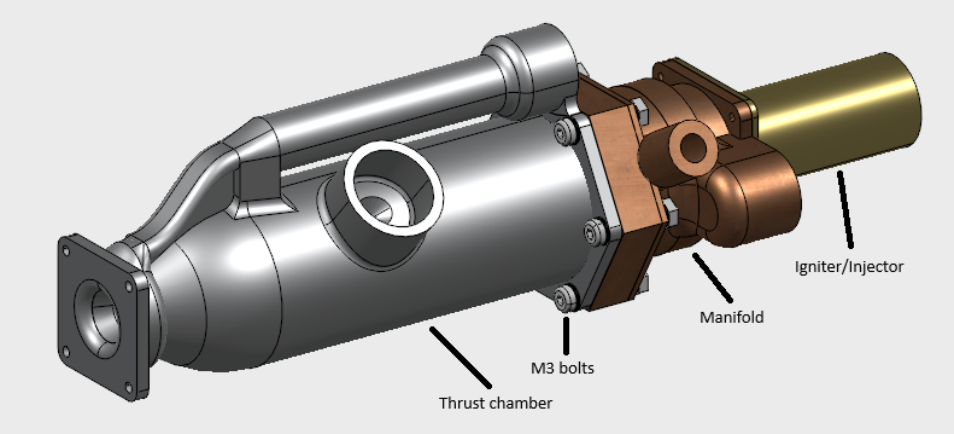

Figure 4.20: Central coaxial swirl injector and glow plug igniter configuration CAD model

While no (publicly known) engine exists that has this type of configuration, the concept is theoretically and physically sound. This assumes that the glow plug does not heat up the injector element excessively and the coaxial swirl injector performs well with an internal element. As the coaxial swirl injector design handbook from Bazarov et al., 2004 does not include this specific configuration or any configuration with an internal element, some design considerations and changes had to be made based on the original coaxial swirl element design. The design was largely kept the same, with the only major difference being the radius. To allow for the coaxial swirl injector element to have an internal element, the original outlet area for each propellant was calculated, and the radius was increased such that the area was kept identical. Since this thruster configuration could be seen as the most experimental or unverified as no data exists on a thruster with a central coaxial swirl element and internal igniter, it was decided to do a full CFD and FEM analysis on this configuration. Not only would this indicate how the inner element affects the swirl injector's performance, it would also verify the thrust chamber's operation, specifically regarding thrust generation and cooling capability.

4.7.3. Triplet Injector and Spark Plug Igniter

In order to show the modularity of the thruster, a third configuration was developed. This thruster includes twelve triplet injector elements integrated into the manifold together with a central spark plug igniter. As this is more of a conventional design, it was not prioritized for computational analysis and rather will be tested in the propulsion lab. An important consideration for designing an impinging injector is the amount of elements. Based on the size of the engine and the minimum size of the orifices, it was decided to have twelve elements, as any more elements would either reduce the size too much resulting in manufacturing difficulties, or it would simply not fit in the faceplate, resulting in overlapping orifice channels. Furthermore, as the design has many internal channels, it was decided to additively manufacture the manifold for this configuration. In order to show the modularity of the thruster, it was decided to use a spark plug igniter for this design. A 3D model of this configuration can be seen in Figure 4.21.

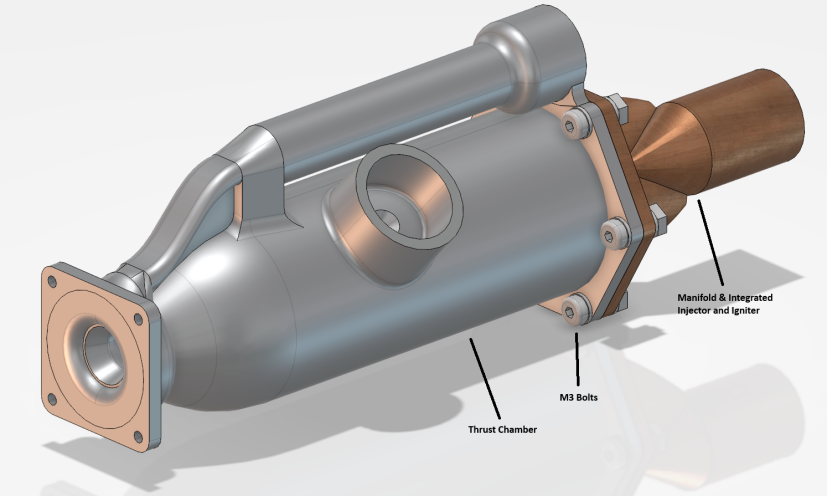

Figure 4.21: Unlike impinging injector and spark plug igniter configuration CAD model

5
Verification Approach

In order to show the functionality, performance and structural integrity of the thruster, a verification process needs to be performed. Based on the requirements that were developed, a verification control matrix (VCM) was set up, which can be seen in Appendix D. This chapter will describe the verification process in detail. During the verification campaign of the thruster, multiple tests shall be performed in order to ensure the requirements stated in the VCM are satisfied. As this thruster shall not be used in space, and thus will not undergo a rocket launch, this list of testing methods shall be limited to what is necessary in preparation of a full-system hot-fire campaign of the engine.

These tests shall be performed at either ESA ESTEC in Noordwijk, The Netherlands or the newly constructed propulsion laboratory in Marknesse, The Netherlands. Small component tests such as cold flows and actuation tests can be performed in Noordwijk, while bigger, pressurized tests such as leak tests and hot-fires shall be performed in Marknesse[1].

Next to the physical tests, requirements are also be verified by means of analysis. Either by performing calculations by hand or simple computing, or by the use of computational software such as CFD and FEA. This is the main verification method that is performed in this thesis. The CFD and FEA methodologies are discussed in the following sections. In the final section, the verification plan related to the physical testing is shown. The verification method "Review of Design" is either verified during the design process, or it is related to a test performed by the manufacturer or supplier.

5.1. CFD Simulation Setup

In order for a CFD simulation to be accurate, but also not be too costly (in time and power) to run, careful considerations have to be made before the simulation is performed, to avoid wasting time and having to make changes to the setup again later. In this section, the full simulation setup of the CFD that was performed will be shown. This includes the mesh, but also boundary conditions, viscous models, material/fluid setup, combustion, solving methods etc. As was mentioned before, the CFD was performed on the configuration with the central coaxial swirl injector and central internal glow plug igniter. In order to capture the swirling effect properly, the CFD was performed in a 3D domain.

5.1.1. Geometry

For the geometry of the thruster, a simplified geometry was chosen in order to make the meshing and subsequent simulation simpler and easier to converge. The cooling channels are kept with the same geometry, however they are inserted as a separate fluid domain, meaning in the CFD the thruster is not fully 'regenerative'. Instead, the nitrous oxide will be inserted into the injector with an artificially set higher temperature (depending on the outlet temperature of the coolant from previous runs). As it is desired for this simulation to see the temperature of the thrust chamber wall, a simplified version of this wall was generated. To avoid a too large amount of cells, it was decided to not simulate the manifold and injector. However, the glow plug tip was simulated, in order to verify that the glow plug would not be subjected to too high temperatures.

[1] Due to the propulsion laboratory in Marknesse being unfinalized, this could be subject to change.

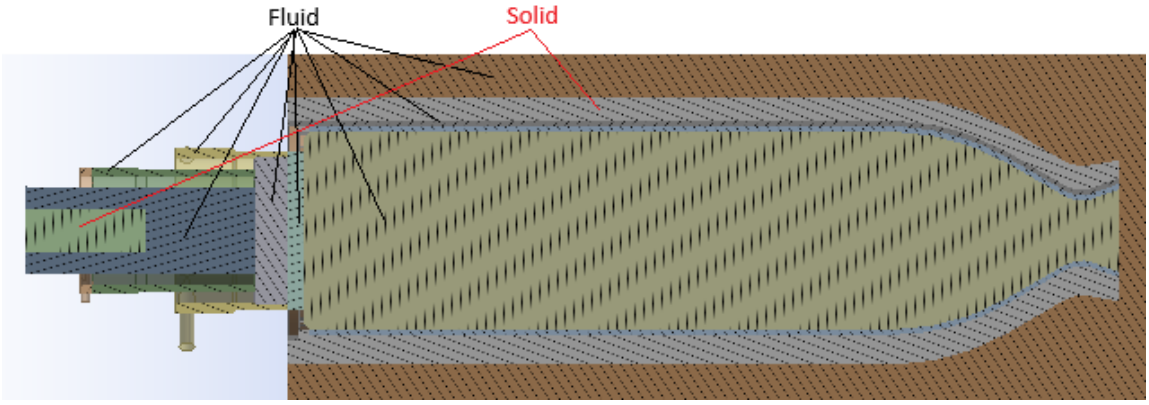

Figure 5.1: CFD main geometry section view

Initially, simulations were performed without an external fluid domain and with the outlet at the exit of the nozzle. However, due to the outlet being a supersonic domain, this would not converge and gave inaccurate results. Thus, it was decided to have an external fluid domain or “farfield” in order to simulate the exhaust of the engine properly and have a more accurate simulation. To ensure the simulation has a realistic exhaust, but also limit the size of the simulation, it was decided to have the farfield be around 2.5 times the combustion chamber length. This is an arbitrary length, which was decided by increasing the length as much as possible while not resulting in an excessive amount of cells. Furthermore, initial simulations showed that the exhaust plume had sufficient space to develop in this length, and thus the length was not changed. A section view of the full fluid domain can be seen in Figure 5.2.

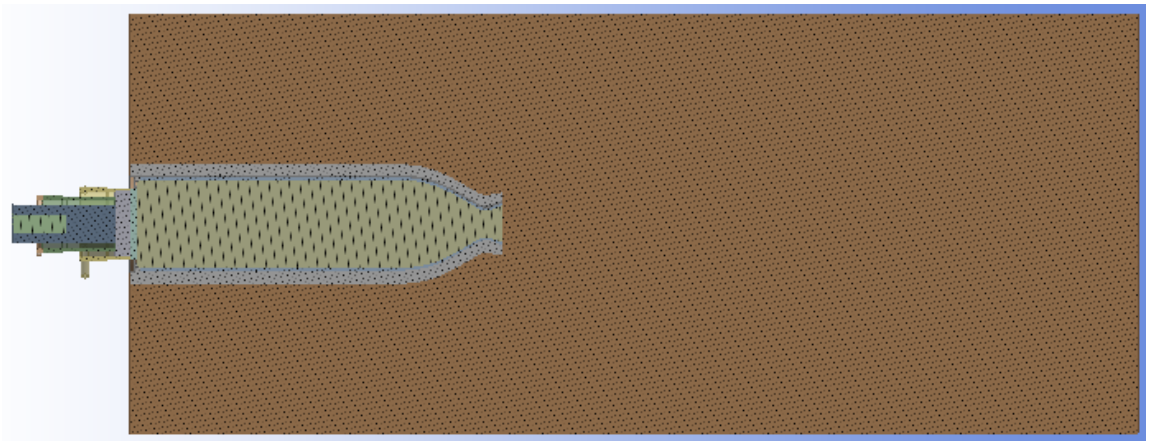

Figure 5.2: CFD full fluid domain section view

To simulate the swirling effect properly, at each tangential inlet for both the fuel and oxidizer an extrusion was made of a few mm long straight “pipe” in order to properly set the boundary condition and have the flow enter the injector tangentially. The geometry can be seen in Figure 5.3

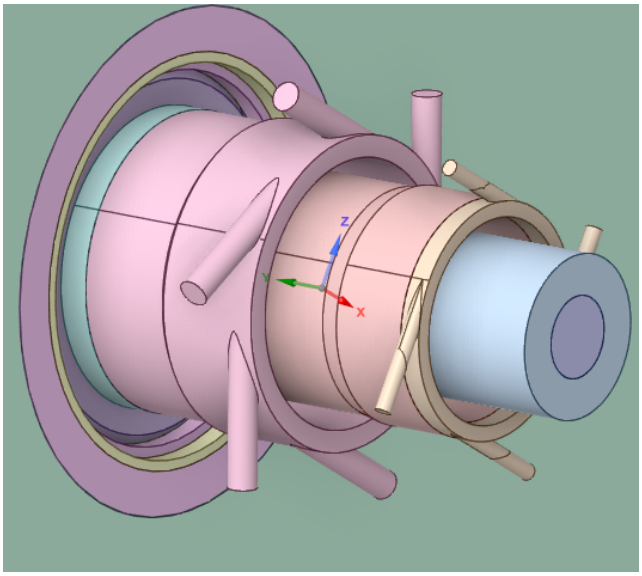

Figure 5.3: Swirl injector fluid domain geometry

5.1.2. Mesh

Ansys Meshing was used for meshing the geometry. The software by itself has an automatic mesh generation tool that can already generate a good coarse mesh, however some adjustments had to be made in order to obtain a finer, higher quality mesh. In this case, there were four meshing criteria that were considered in order to see if the mesh quality is sufficient. These were skewness, orthogonal quality, element quality and aspect ratio. The quality spectrum for these criteria can be found in Table 5.6.

Table 5.1: ANSYS Mesh Quality Spectrum (Ansys Inc., 2024)

Metric	**Excellent**	**Very Good**	**Good**	**Acceptable**	**Bad**
Skewness	0.00 – 0.25	0.25 – 0.50	0.50 – 0.80	0.80 – 0.94	> 0.95
Orthogonal Quality	0.95 – 1.00	0.70 – 0.95	0.20 – 0.69	0.15 – 0.20	< 0.15
Element Quality	0.80 – 1.00	0.5 – 0.8	0.30 – 0.50	0.05 – 0.30	< 0.05
Aspect Ratio	1 – 5	5 – 10	10 – 35	35 – 100	> 100

Naturally, you would desire to be near the excellent region of all the metrics. However, realistically, for a complex geometry like this with small cooling channels and curved domains this is difficult to achieve. To refine the mesh, three main built-in meshing control methods were used, namely element sizing, inflation meshing and contact sizing. Firstly, element sizing was used on the main fluid domains (0.15 mm for injector, 0.4 mm for thrust chamber, 0.2 mm for cooling channels and 2 mm for surrounding fluid/exhaust domain). These values were found to be the optimal distribution, as smaller values would increase the amount of elements exponentially, and thus computational time without significantly improving the mesh quality.

Inflation meshing was done at a few locations, firstly near the inner wall of the combustion chamber, in order to accurately simulate the boundary layer and the convection heat transfer between the fluid and the wall, secondly in the cooling channels, also to simulate the boundary layer and convection, thirdly in the farfield fluid domain around the thruster itself, to first of all simulate the convection from the thruster to the atmosphere and secondly to have a more refined mesh near the thruster exhaust and have proper simulation of the velocity distribution. Finally, an inflation mesh was also generated around the solid glow plug element, to have a good simulation of the convection.

In order to have a similar cell size near fluid interfaces as well as solid-fluid interfaces, at some locations contact sizing was used. This was specifically done between the cooling channels and the thruster wall, as well as the fluid domains of the thruster and the farfield, and finally also between the fluid domain of the thruster and the thruster wall. With these mesh controls applied, the following mesh quality is found:

Table 5.2: Mesh Statistics and Quality Criteria

Statistic	**Value**	
Nodes	3,194,598	
Elements	12,454,906	
Metric	**Average**	**Worst**
Max Aspect Ratio	2.029	15.275
Min Element Quality	0.833	0.323
Min Orthogonal Quality	0.787	0.202
Max Skewness	0.211	0.733

As the average values are all in the excellent/very good limits, and the worst values are not within the unacceptable ranges, this mesh was deemed to be sufficient for the CFD simulation. Furthermore, it was also inspected that the worst cells are not cluttered in a specific region, which could still result in inaccurate results or divergence within the simulation. The meshes themselves can be seen in Appendix C.

5.1.3. Fluent Setup

For the CFD simulation itself, Ansys Fluent was used. A viscous transient simulation was performed, including non-premixed combustion. In Table 5.3, an overview is given of the general solver setup and which models are used. In this section, I will go more in depth on the reasoning and specific settings of the models.

Table 5.3: Summary of Solver Setup

Solver Settings	
Time Definition	Transient
Solver Type	Pressure-Based
Gravity	Off
Active Physical Models	
Energy	On
Viscous Model	Realizable $k-\varepsilon$ (Incl. Enhanced Wall Function)
Radiation	Discrete Ordinates (DO)
Species	Non-Premixed Combustion

For the turbulence model, both $k-\epsilon$ and $k-\omega$ were tried, however $k-\epsilon$ gave better convergence. The wall y+ distribution can be seen in Figure 5.4. y^+ is a dimensionless distance from the wall to the first mesh node. It is essentially a way to see which parts of a boundary layer the CFD simulation can solve, and is defined by the following equation:

$$y^+ = \frac{y u_\tau}{\nu} \tag{5.1}$$

Where,
y^+ Dimensionless wall distance [-]
y Absolute distance from the wall to the first cell center [m]
u_τ Friction velocity [m/s]
ν Kinematic viscosity of the fluid [m^2/s]

In Figure 5.4 this value might seem high, however it should be noted that $k-\epsilon$ only solves turbulence in the log layer, where the y+ value ranges from around 30 to 350 (ANSYS, 2020). As the y+ values fall in this range, the near-wall mesh quality was deemed sufficient. In order to still simulate the sub/buffer layer to improve heat transfer accuracy, the enhanced wall function model that is built into Ansys Fluent was used.

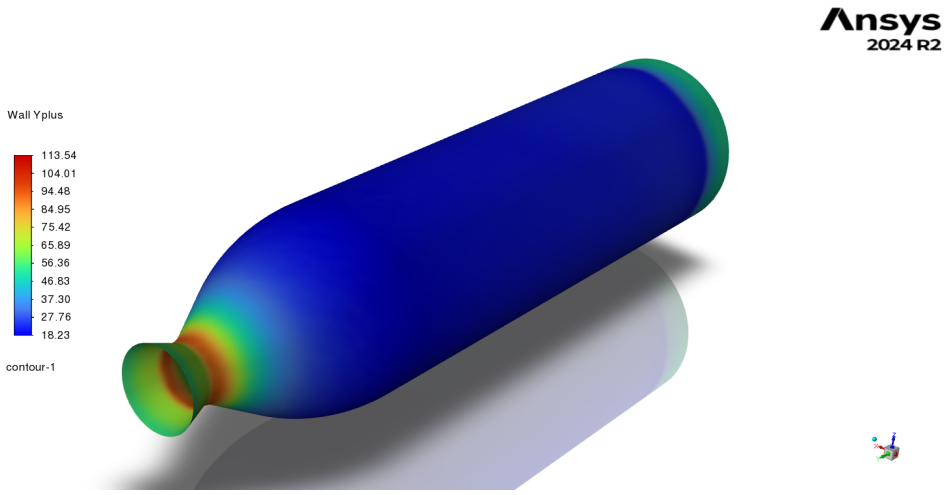

Figure 5.4: Y+ distribution in combustion chamber

As was specified before the coolant fluid and the main fluid domain of the thruster are separated. Thus for the boundary conditions, there are three inlets specified and two outlets. An overview of the inlet and outlet boundary conditions and the key parameters can be seen in Table 5.4. For the pressure outlets should be noted that Ansys uses a gauge pressure as input. That results in an absolute pressure which is the summation of the gauge pressure and the operating pressure. As the thruster was fired in atmospheric conditions, the operating pressure is 1 atm. Furthermore, all the walls between a fluid and a solid were set as thermally coupled to properly simulated the heat transfer. The outer wall of the farfield was set at a constant temperature of 300 K. For the wall material ABD900AM was used, as this gave the best results during the thermal optimization process as can be seen in subsection 6.1.1.

Table 5.4: Boundary Conditions Summary

Boundary Name	**Type**	**Quantity**	**Value**
Inlets			
Inlet Coolant	Mass-Flow Inlet	Mass Flow Rate Temperature	$0.010\,42\,\mathrm{kg\,s^{-1}}$ 300 K
Inlet Fuel	Mass-Flow Inlet	Mass Flow Rate Temperature	$0.001\,16\,\mathrm{kg\,s^{-1}}$ 300 K
Inlet Oxidizer	Mass-Flow Inlet	Mass Flow Rate Temperature	$0.010\,42\,\mathrm{kg\,s^{-1}}$ 500 K
Outlets			
Main Outlet	Pressure Outlet	Gauge Pressure Temperature	0 bar 300 K
Outlet Coolant	Pressure Outlet	Gauge Pressure Temperature	7 bar 500 K

For the viscous model, both $k-\epsilon$ and $k-\omega$ were used, however it was found that $k-\epsilon$ gave better convergence, thus this model was used for the final simulation. The realizable $k-\epsilon$ model with default Fluent settings was used, including enhanced wall treatment with thermal effects, in order to have the most accurate wall temperature. For the radiation model, the discrete ordinates model was used. This is generally seen as one of the most accurate radiation models that is not computationally too demanding, and can simulate gases well, unlike the P1 model which is more suited for dense fluids (Kord, 2025).

Combustion is one of the most complicated things to simulate. Ansys Fluent has multiple methods to simulate combustion, but for this case it was decided to use the Non-Premixed Combustion Chemical Equillibrium model.

The Steady Diffusion Flamelet would have been preferred however for this method a chemical kinetics mechanism is required, and as none could be found for N_2O/C_2H_6, the chemical equilibrium model had to be used. In the Non-Premixed Combustion Chemical Equillibrium model, the combustion is simulated by means of a look-up table, where mean values of species fractions, density, and temperature are looked up depending on the local mixture fraction and mixture fraction variance. This means that ignition is not simulated, which is a limitation but also makes the model less complex. This does mean that most likely the hot gas temperature, especially near the inlet, will be overestimated due to the fact that the gases "combust" instantly once they come in contact. For comparison, the flamelet model uses finite-rate chemistry where the chemical equillibrium model assumes instantaneous combustion. Because of this the equillibrium model will generally over-predict peak flame temperatures and is poor at predicting intermediate species.

With regard to the spatial discretization methods in Ansys, the initial value for each method was first order. After the run converged for one-hundred time steps, one of the methods was increased. This was done every one-hundred time steps until the following final setup which can be seen in Table 5.5 was reached. It was attempted to increase also the transient method to second order, however this would often result in divergence, thus it was kept at first order. For the pressure-velocity coupling method, multiple methods were tried, but it was found that PISO gave the best convergence. For the momentum, it was decided to use third-order MUSCL, as the Ansys Fluent user guide advises on this for swirling flows.

Table 5.5: CFD Solution Methods and Spatial Discretization Schemes

Setting	**Scheme / Method**
Pressure-Velocity Coupling	PISO
Spatial Discretization	
Gradient	Least Squares Cell Based
Pressure	PRESTO!
Density	Second Order Upwind
Momentum	Third-Order MUSCL
Turbulent Kinetic Energy	Second Order Upwind
Turbulent Dissipation Rate	Second Order Upwind
Energy	Second Order Upwind
Discrete Ordinates	Second Order Upwind
Mean Mixture Fraction	Second Order Upwind
Transient Formulation	First Order Implicit

For the running the simulation, the supercomputer from the TU Delft was used, DelftBlue. A journal file was made, where during the run the time step would be increased. Fixed time-steps were used, as adaptive time steps would result in a very low time step (around 5e-8 s), most likely due to the many transient processes in the flow. This would be acceptable for characterizing the flow patterns, but it is not acceptable for simulating the heat transfer, as this would simply make the simulation too long. The run was started with a time step of 1e-6 s, slowly doubling it after 100 time steps until it reached a time step of 5e-5 s. It was found that increasing the time step more than this would eventually lead to divergence. During the run, the flow was observed by 2D pictures of the temperature distribution. This was done in order to ensure the flow would not drastically change after a change in time step. Furthermore, this would also give a good indication of convergence.

5.2. FEM Simulation Setup

After the CFD simulation was finalized, using the outputs of the CFD simulation a static loading simulation was done, in order to verify the structural performance of the thruster while undergoing high heat loads and pressure. For this simulation, there were a couple of things that needed to be verified. First of all, the chamber has a small inner wall thickness of only 0.5 mm. Initial calculations showed that this is sufficient, however FEM is needed to verify this. Secondly, the structural integrity at the point of highest temperature in the thruster should be verified. Since here the yield strength is the lowest, this could be a critical point. Lastly, the stress at the interface and inside the bolts should be simulated in order to verify that the current interface is sufficient. It should be noted that as the FEM analysis was performed with static loading and a constant temperature, it does not fully verify the structural integrity of the thruster. A future recommendation would be to include variable loading and thermal cycling in the thruster wall in order to perform a complete verification.

5.2.1. Geometry

For the geometry of the thruster, the same geometry was used as the geometry in the CFD simulation, however a few things were added. Firstly, the boltholes/flange of the thrust chamber were removed in the CFD simulation in order to reduce complexity of the geometry and mesh. In this simulation, these holes are added again in order to simulate the bolted interface. Secondly, in order to have this interface, a rough geometry simulating the manifold was generated, excluding the internal channels. The full geometry, excluding the surrounding farfield can be seen in Figure 5.5.

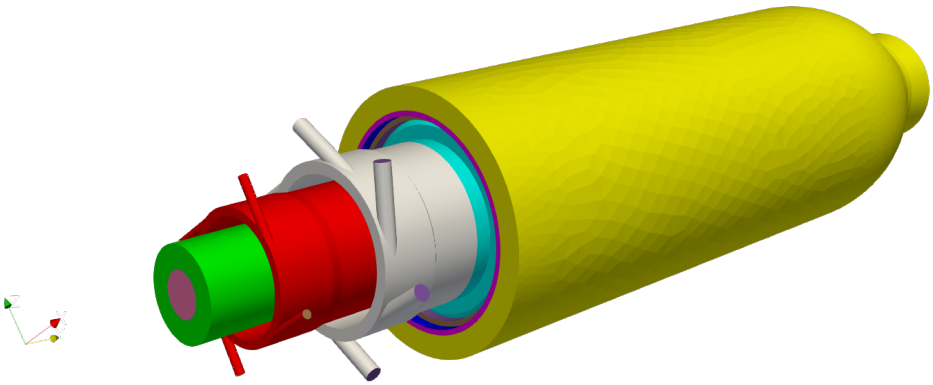

Figure 5.5: Isometric view of CFD main geometry

5.2.2. Mesh

The thrust chamber itself was split into three different bodies. There are the inner and outer wall of the chamber, which were also present in the CFD simulation, and there is the flange/boltholes body, which was added for this simulation. For the mesh quality guidelines, the criteria which can be seen in Table 5.6 were adhered.

Table 5.6: Ansys Mechanical mesh quality spectrum (Ansys Inc., 2024)

Metric	Excellent	Very Good	Good	Acceptable	Bad
Skewness	0.00 – 0.25	0.25 – 0.50	0.50 – 0.80	0.80 – 0.94	≥ 0.95
Element Quality	0.80 – 1.00	0.70 – 0.80	0.50 – 0.70	0.10 – 0.50	< 0.10
Jacobian Ratio	0.95 – 1.00	0.80 – 0.95	0.50 – 0.80	0.10 – 0.50	≤ 0.00
Aspect Ratio	1 – 5	5 – 10	10 – 20	20 – 50	> 50

In order to have the mesh propagate smoothly through the whole geometry, shared topology was used between these three parts. However still, similarly to the CFD mesh, sizing tools were used to size the different bodies separately. For the inner wall of the chamber, an element size of 0.25 mm was used, while for the other bodies a size of 0.4 mm was used. This gave the following mesh quality in Table 5.7.

Table 5.7: Mesh Statistics and Quality Criteria

Statistic	Value	
Nodes	5,259,703	
Elements	3,629,537	
Metric	**Average**	**Worst**
Max Aspect Ratio	1.889	7.83
Min Element Quality	0.825	0.216
Min Jacobian Ratio	0.995	0.244
Max Skewness	0.251	0.964

From this it can be seen that the mesh is slightly worse compared to the CFD mesh, however it is still deemed sufficient. Furthermore, similarly to the CFD mesh it was ensured that the “bad” cells are not clustered around the same point, and rather are spread through the geometry. The full mesh can be seen in Appendix C.

5.3. Testing

While no physical verification was performed during this thesis, a verification plan was nonetheless made in order to lay the groundwork for any future tests performed by ESA. In the following subsections the different tests will be elaborated on, as well as the test locations. It should be noted that these tests could be subject to change, and procedures still have to be written. The purpose of this engine is to commission a test facility that is being developed

by ESA. With this in mind, the test methods have been developed in such a way that the facility is fully validated by means of testing this thruster.

5.3.1. Inspection

Upon arrival of the parts from external suppliers, but also those manufactured in-house, these parts should be properly inspected to verify important characteristics such as the (critical) dimensions and roughness. For this, the following methods below will be used. All these tests can and should be performed in the clean room, such that no dust or dirt would be able to enter the small channels in for example the cooling channels, the manifold, or the injectors.

Dimensions

To verify the critical dimensions of the thruster specified in the test requirements, specific tools can be used. One of the most common tools used in engineering is a caliper, which can measure a dimension accurately with an accuracy of 0.01 mm.

Roughness

Another very important characteristic, especially in small thrusters, is roughness. Too high of a roughness in the thrust chamber additively manufactured body could cause high pressure drops in the cooling channels. While too high of a roughness in the triplet injector manifold could cause misalignment of the injection streams, leading to bad mixing. In aerospace and space propulsion applications, a common measurement tool for roughness is called a contact stylus profilometer (surface roughness tester). This device has a diamond tip that can be dragged along a surface to record many measurements and create a line profile that will result in an average roughness (Ra) and two roughness parameters (Rq and Rz) that will emphasize the roughest points.

To measure the roughness inside the cooling channels, an estimate of the average roughness will need to be made at the exit of the cooling channels (where it attaches to the manifold). Here, the roughness should be measured in each cooling channel, and an average should be taken of that value.

5.3.2. Component and System Tests

The thruster consists of five different parts (excluding fasteners, o-rings and fittings) that should be tested in order to verify the requirements stated previously. These parts are the additively manufactured thrust chamber made from ABD900AM. The coaxial swirl injectors, both made from IN625. The injector plate/manifold which houses the injector and the igniter, of which the material is currently chosen to be IN625, but could still be changed depending on the manufacturing entity. IN625, IN718 and ABD900AM are all suitable. In Table 5.8 the materials and its properties are shown. The igniters, specifically a glow plug igniter with a ceramic sheathed tip and a 1/4-32 spark plug igniter. And finally the valves, which are poppet valves developed by Gevasol. The specific test requirements have been stated before, however to summarize, the components should be sufficiently leak tight, can withstand high pressures and temperatures and should have the performance characteristics as it was designed for.

Table 5.8: Component Material Properties

Material	**Density** (g/cm^3)	**Melting Range** ($^\circ C$)	**Yield Strength** (MPa) @$25C$	**Ultimate Tensile Strength** (MPa) @$25C$	**Max Elongation** (%)
IN718 (SPECIAL METALS, 2007)	8.19	1260 – 1336	1100	1375	25
IN625 (Special Metals Corporation, 2013)	8.44	1290 – 1350	414	827	30
ABD900AM (Alloyed, 2025)	8.395	1285 – 1366	>900	>1300	>10

Thrust Chamber

The thrust chamber can be seen as arguably the most important part of the thruster. Especially in small engines, this is a critical component, since here the highest temperatures occur (>3000 K) and also the highest loads on the

structure. Furthermore, in the end the thrust chamber, as the name suggests, will create a certain amount of thrust based on the geometry of the thrust chamber, the propellants that are used and the injector design.

The most important test that should be performed, but is usually done at the final stage, is a hot-fire test. This is an integrated system test that measures multiple parameters specified in the requirements, but most importantly it will measure the performance of the engine such as specific impulse, exit velocity and chamber pressure. However, as this is a test which carries certain safety risks, a number of de-risking tests should be performed first in order to verify the capabilities of the thruster. As was specified before, the thrust chamber includes eight thermocouple holes, in two groups of four, where each group is distributed along the axial direction of the chamber wall, and has a specific hole length (distance from the inner wall). During testing, it is suggested to have thermocouples in all holes. For each thermocouple pair at the same axial location, the temperature and can be measured. Together with the known distance to the inner wall, the inner wall temperature can be interpolated. It is important to use all thermocouple holes, as the swirling effect could potentially create hot spots, thus it is important to cover a large part of the wall. After the hot-fire has been performed, a comparison should be performed between the testing data and the CFD results that were found during this thesis.

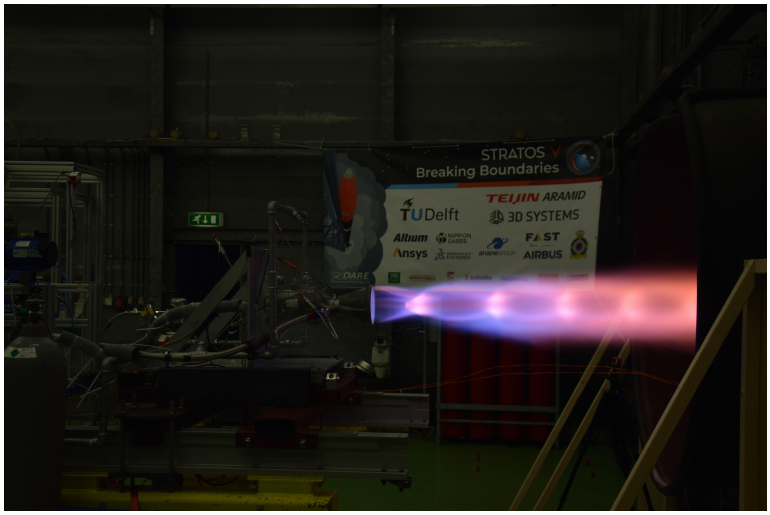

Figure 5.6: Hot-fire of the DLX150B "Firebolt" LOx/Ethanol engine developed by Delft Aerospace Rocket Engineering (Delft Aerospace Rocket Engineering, 2024)

A test that could be performed to verify the pressure drop in the cooling channels is a so-called coolant-channel pressure drop characterization. This method uses water or a gas like nitrous oxide to flow through the cooling channels, where than on each side the pressure is measured with varying mass flows. To validate the previous simulations, it should also be compared with the pressure drop inside the cooling channels of the thruster in the CFD results. Furthermore, also a visual verification here can be done to see if any of the cooling channels are blocked.

Furthermore, the cooling channels can also be pressurized to both proof and burst pressure in order to verify the structural integrity. However, with this test it should be taken into account that there are no thermal stresses present.

Injector and Manifold

During testing activities, the injector, and the manifold will often be integrated with each other in order to perform the test. For that reason, they have been put in the same section. Regarding the injector, there are a few key parameters that should be characterized. These are specifically the discharge coefficient, which is the actual mass flow compared to the ideal theoretical mass flow, the pressure drop, the actual mass flow itself, the spray pattern and atomization and the structural integrity when it is subjected to high pressures and temperatures.

Most of these characteristics will be characterized during simulations of CFD and FEA, however they should still be verified in physical testing. For the injector, this is usually done by performing a cold flow using either the actual propellants or a cheaper alternatively like water or a certain gas. It should be noted that the nitrous oxide and ethane are injected in gaseous state, and as such using water for a cold flow test will probably give less accurate results. The

cold flow tests should be performed along the entire pressure box.

The cold flow campaign will have two separate phases. First, the injector should be tested with water or a visible (but safe) gas where it is hooked up to a hose in order to verify the spray pattern of the injector and the impinging point of the two propellants. This can be done by simply printing a PLA housing which can be attached to the hose and is leak tight (perhaps by using o-rings or other sealing methods). This test could also be performed with the injector already inserted into the manifold, such that a hose can be attached to the fuel and oxidizer inlets respectively. This way, the pressure drop along the entire manifold plus injector can be characterized. It should be noted that the connecting of a hose to the nitrous oxide ports could be difficult, since this is essentially the ring connected with the cooling channels.

In the second phase, the cold flow will be performed by including the entire propulsion system (perhaps the feed system will be variable however the thruster as designed in this report will be the same), the igniter could be included for completeness but is not necessary, as in a cold flow it is not used. With this cold flow, the flow throughout the entire system can be characterized, and possibly also the pressure drop from the valve until the combustion chamber.

In addition to the performance characterization, the structural integrity of both the injector and the manifold should also be verified. Prior to any pressurized tests, a leak test using helium should be performed on all the seals, threads and other interface that could have leaks. In general, a leak test is performed in such a way that the testing element is pressurized up to a certain pressure and a helium sniffer (an electronic device which can measure the percentage of helium in the atmosphere) is used to measure the leak rate.

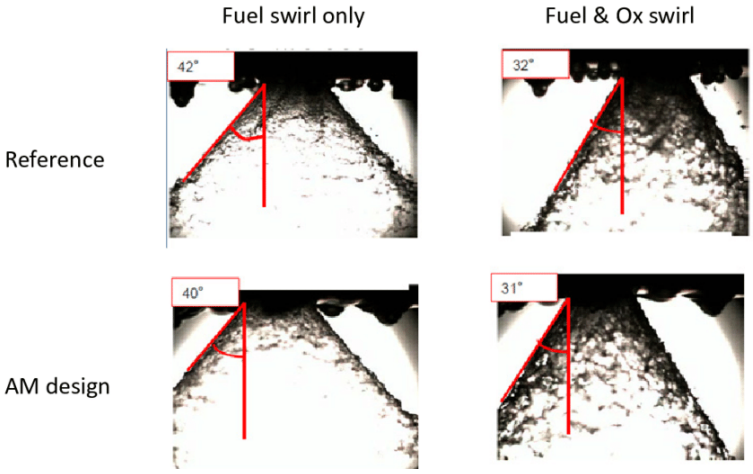

Figure 5.7: Flow patterns for coaxial swirl injectors (Soller et al., 2017)

Igniter
Before any integrated tests can happen with the igniter, it should first undergo certain acceptance tests in order to verify the performance and the reliability as a standalone component. Since igniters are almost always electrical components that require a supply voltage, they should be actuated with the supply voltage given by the supplier and a small margin above and below. If the engine were to be flown on a satellite, there is a limited voltage the satellite power supply can supply to the igniter. In that case, a custom PCB is necessary in order to increase this voltage using a voltage transformer. However, this engine currently will not be flown in space, so this is not necessary.

For the glow plug specifically, certain tests will have to be performed in order to characterize the temperature of the heating element, which should be higher than 1200 K as specified in requirement [3.5.2-1]. As glow plugs are generally not often used in space propulsion thrusters, it would be interesting to go further than the basic acceptance tests and perform a comparison between different glow plugs from different suppliers (NGK, Bosch HKT), and characterize the effect of the material, location, heating time, voltage, and dimensions of the glow plugs. With respect to the spark plug, a duty-cycle test can be performed by perming a high number of spark ignitions and visually inspecting the spark plug after this test.

Regarding the integrated tests these tests will be performed in the same manner for both the spark plug and the

glow plug, where a hot-fire is performed with the whole integrated system including all the components, and ignition is verified using cameras, pressure sensors and temperature sensors.

Valves
While the valves will already undergo some tests during the development at the supplier/manufacturer, more tests are needed in order to completely verify that the valves are safe and perform as desired. Furthermore, it is generally less costly to test the functionality of the valve in-house (if the required equipment is available) compared to outsourcing the testing or having it done by the supplier. In this section, both the tests done by the supplier and the tests that will be performed at ESA will be shown.

Before the valve is pressurized or in contact with any of the propellants or test fluids/gasses, the valve will be dry-cycled both in order to verify its proper actuation, but also to ensure that the poppet of the valve is properly seated into the valve orifice, making sure it is leak tight when pressurized. This will first be done in a batch of 100 cycles, and secondly another batch of at least 2000 cycles. Between these cycles, if desired, ESA could opt for performing a leak test, in order to see the effect of the cycles on the valve.

After the dry cycles have been performed, the valves will be pressurized in order to verify its leak tightness. This will be done with helium up to a pressure of 60 bar for both valves. A helium sniffer will be used to measure the leak tightness.

After the leak testing, the mass flow of the valve must be calibrated. This will be done by using an existing needle valve on the feed system developed by ESA in combination with a mass flow meter. Then, the mass flow will be measured and set according to the pressure box in subsection 5.3.3.

5.3.3. Pressure box
In order to set the boundaries for at what operating conditions the testing shall take place (excluding safety factors), a pressure box was developed. This box or envelope essentially shows the nominal operating conditions of the thruster, and thus at which conditions the thruster should still be able to perform a hot-fire and pass all the tests. Based on this envelope the test values will be set, depending on the component or (sub)system that is to be tested.

N_2O / Ethane Saturation Pressure Box (5°C – 25°C)

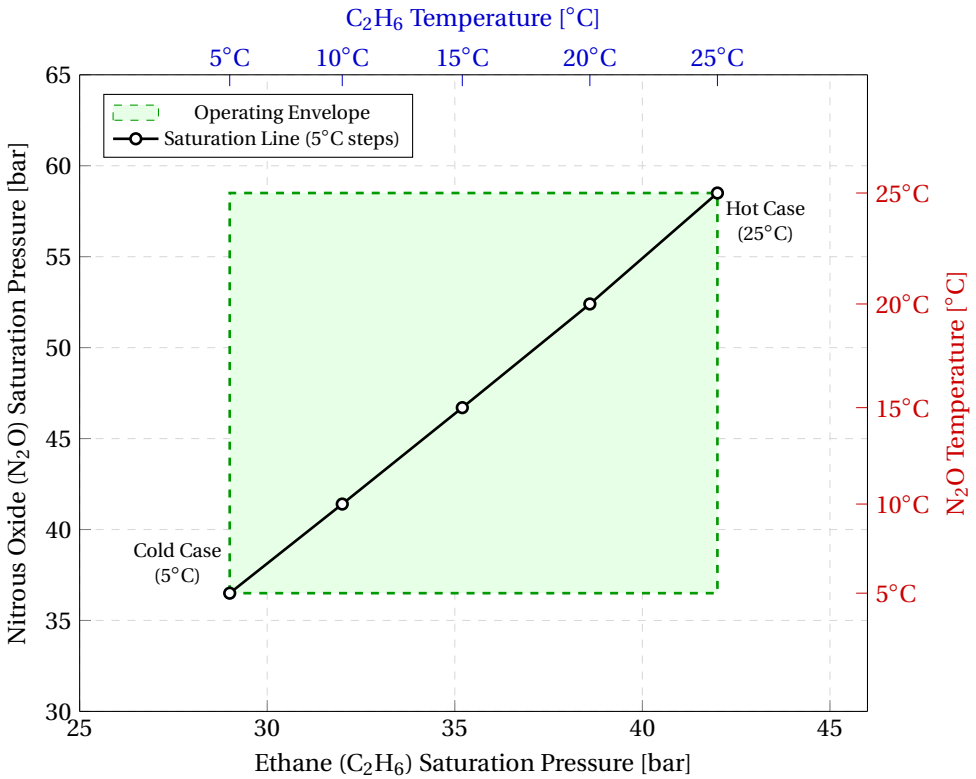

5.3.4. Test Overview

In Table 5.9 an overview is given of the tests that will be performed and which requirements will be verified by these tests.

Table 5.9: Test-to-requirement verification matrix (ground / sea-level campaign).

Test ID	Test	Location	Requirements verified (ID)
SAF-01	Safety verification checks	ESTEC & Marknesse	3.2.1, 3.2.1, 3.2.1, 3.2.1, 3.2.1, 3.2.1
INS-01	Incoming inspection: critical dimensions	ESA Cleanroom (ESTEC)	[3.2.2-1], [3.2.2-2], [3.2.2-3], [3.4.1-4], [3.5.2-2], [3.5.2-3], [3.3.3-4], [3.3.3-5], [3.4.3-3], [3.3.3-8]
TC-01	Coolant-channel pressure-drop characterization	Marknesse	[3.3.1-2]
TC-02	Thrust chamber proof pressure test	Marknesse	[3.3.3-1]
TC-03	Thrust chamber burst pressure test	Marknesse	[3.3.3-2]
IM-01	Injector/manifold helium external leak tests	Marknesse	[3.4.1-3]
IM-02	Injector/manifold cold-flows	Marknesse	[3.4.2-1], [3.4.2-2], [3.4.2-3], [3.4.2-1], [3.4.2-2], [3.4.2-3], [3.6.2-1], [3.6.2-2], [3.6.2-3]
IGN-01	Igniter electrical actuation acceptance (nominal supply voltage ± margin)	ESTEC	[3.5.1-1]
IGN-02	Glow plug heating element temperature characterization	ESTEC	[3.5.2-1]
IGN-03	Spark plug duty-cycle / repeated ignition test + post-test inspection	ESTEC	[3.4.2-4]
VAL-01	Valve dry-cycling	ESTEC	[3.6.1-5]
VAL-02	Valve helium leak tests (external + internal leak rate), before and after cycling/-operation as applicable	Marknesse	[3.6.1-1], [3.6.1-2]
VAL-03	Valve flow calibration / characterization	Marknesse	[3.6.2-1], [3.6.2-2], [3.6.2-3]
HF-01	Atmospheric integrated hot-fire (1 x 60 s)	Marknesse	[HL-1], [HL-4], [3.3.1-5], [3.3.2-1], [3.3.2-5], [3.3.2-2], [3.3.2-3], [3.3.2-4], [3.2.2-6], [3.3.1-1], [3.4.2-4], [3.5.1-2]
HF-02	Lifetime / pulsing campaign hot-fires	Marknesse	[3.3.1-7], [3.3.1-6], [3.4.2-4]

5.3.5. Test Locations

For the testing activities, two main locations will be used. However, this does not include the locations of external suppliers, which also perform their own tests on the ordered parts.

Marknesse ESA Chemical Propulsion Laboratory

The new ESA chemical propulsion laboratory in Marknesse is still under construction, and thus the description of this laboratory will not be complete at the time of writing. However, some details can be given regarding this new laboratory. This new laboratory will be placed on the grounds of the Netherlands Aerospace Centre (NLR), and will be used to test chemical space propulsion engines with a maximum thrust of around 100 N. The facility itself will be a customized sea-transport container, which will have two rooms. One control room where the tests will be actuated and prepared, and a 'test room' where the actual test will be conducted in a safe environment.

The laboratory will be used for multiple engines with different type of propellants, and has a modular feed system architecture. The supply voltage available at the test bench is 24 V. In order to obtain the nitrous-oxide from the tank in gaseous state, the supply tank of nitrous oxide will be directly attached to the system. Alternatively an existing tank

in the test setup could be used, however there the nitrous oxide would be drawn from the bottom of the tank, which could like result in it drawing it in a liquid state. As the thruster is designed for it to be used with gaseous nitrous oxide, this is something that is not desired.

ESA Propulsion Laboratory at ESTEC
ESA already has an existing propulsion laboratory that is present at the main headquarters in the Netherlands, at ESA ESTEC in Noordwijk. However, due to the limited space in the facility it is difficult for ESA to perform loud, (potentially) dangerous, chemical propulsion tests here. So, this lab is mainly used for electrical propulsion tests in vacuum chambers, and small component tests. One of the vacuum chambers used at ESTEC can be seen in Figure 5.8.

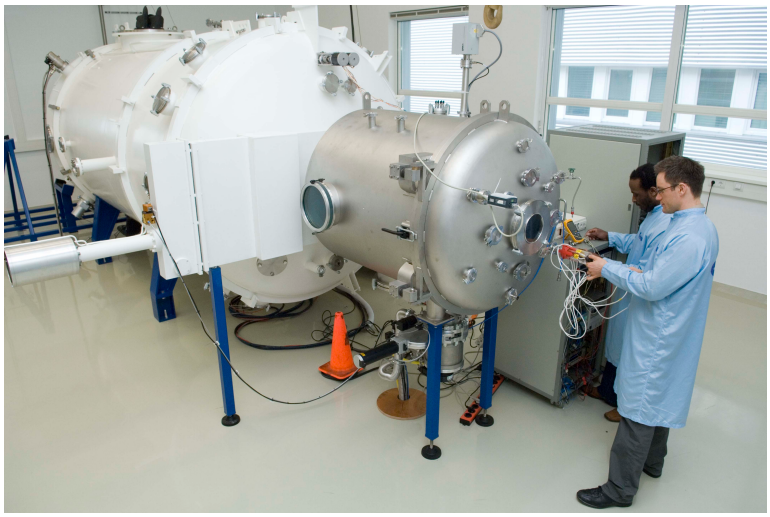

Figure 5.8: The largest vacuum chamber of ESA's Propulsion Laboratory, used for testing different types of thrusters for space. (ESA, 2017)

ESA Cleanroom
Tests that do not perform pressurization or any other potentially dangerous activities, these should be performed in the clean room, in order to make sure that the part does not become contaminated, and is handled with care. Most clean rooms at ESA ESTEC have a class 8 rating, however there are some clean rooms with class 7 and class 5. A typical cleanroom can be seen in Figure 5.9.

Figure 5.9: Cleanroom/controlled-environment installation. (Dagard, 2026)

6
Results and Discussion

This chapter will present the final design of the thruster, and will also go into the verification results of the verification process described earlier in chapter 5. For the design, to perform comparison tests and most importantly show its modularity, three different design configurations were developed. From these three configurations, one was verified using CFD and FEM analysis. As all configurations have the same thrust chamber, only the injector type, which was in this case a swirl injector, differed. The igniter was not simulated, this is something that would either need to be done with further analysis, or most likely with physical testing as described in chapter 5. For the development of the 3D model, 3DExperience was used. For the CFD Ansys Fluent was used and for the FEA Ansys Mechanical was used, using the fluent analysis data as its inputs.

6.1. Design

In this section, the full design of the thruster assembly and all the relevant parameters that were calculated are shown. To keep the section brief, calculations will not be written out, but for reference the theory can be found in chapter 4.

6.1.1. Thrust Chamber

First of all, the thrust chamber geometry was designed using RPA. This gave the following outputs for the geometry from Figure 4.2.

Table 6.1: Thrust Chamber and Nozzle Geometry

Parameter	**Symbol**	**Value**	**Unit**
Chamber Diameter	D_c	18.07	mm
Chamber Length	L_c	72.07	mm
Cylindrical Length	L_{cyl}	54.29	mm
Characteristic Length	L^*	711.01	mm
Convergence Angle	b	30.00	°
Radius 1	R_1	4.09	mm
Radius 2	R_2	21.50	mm
Throat Diameter	D_t	5.45	mm
Nozzle Radius	R_n	1.04	mm
Divergence Angle	T_e	20.00	°
Divergence Length	L_e	3.15	mm
Exit Diameter	D_e	7.61	mm
Contraction Ratio	A_c/A_t	11.00	–

It should be noted that most likely after the thesis, ESA will develop multiple thrust chambers with different characteristic lengths. However, due to the limited length of the thesis, it was decided to pursue the design and subsequent simulations with the characteristic length that can be found in Table 6.1. For this geometry, the estimated performance and efficiencies shown in Table 6.2 could be derived, based on the theory from section 2.2. The total efficiency is simply the nozzle efficiency multiplied with the reaction efficiency.

Based on this geometry the optimization of the cooling channels was performed using PyRocket. In PyRocket a total of 900 different configurations were simulated, each varying in chamber material, number of channels, O/F ratio, channel width and channel height. In Figure 6.1, 6.2 and 6.3, the results can be seen. It was decided to plot the varying parameters against the maximum wall temperature, since this would give the best indication which configuration would be the best option.

Table 6.2: Estimated Performance Parameters

Parameter	Symbol	Value	Unit
Efficiencies & Flow			
Reaction Efficiency	η_{reac}	0.9591	–
Nozzle Efficiency	η_{nozz}	0.9641	–
Overall Efficiency	$\eta_{overall}$	0.9247	–
Characteristic Velocity	c^*	1506.71	m/s
Total Mass Flow Rate	$\dot{m}_{tot}$	0.01158	kg/s
Oxidizer Mass Flow Rate	$\dot{m}_{ox}$	0.01042	kg/s
Fuel Mass Flow Rate	$\dot{m}_{fuel}$	0.00116	kg/s
Optimum Expansion Performance			
Chamber Thrust	F_{opt}	0.01980	kN
Specific Impulse	$I_{sp,opt}$	174.39	s
Effective Exhaust Vel.	$v_{e,opt}$	1710.19	m/s
Thrust Coefficient	$C_{f,opt}$	1.1351	–
Vacuum Performance			
Chamber Thrust	F_{vac}	0.02461	kN
Specific Impulse	$I_{sp,vac}$	216.69	s
Effective Exhaust Vel.	$v_{e,vac}$	2125.04	m/s
Thrust Coefficient	$C_{f,vac}$	1.4104	–

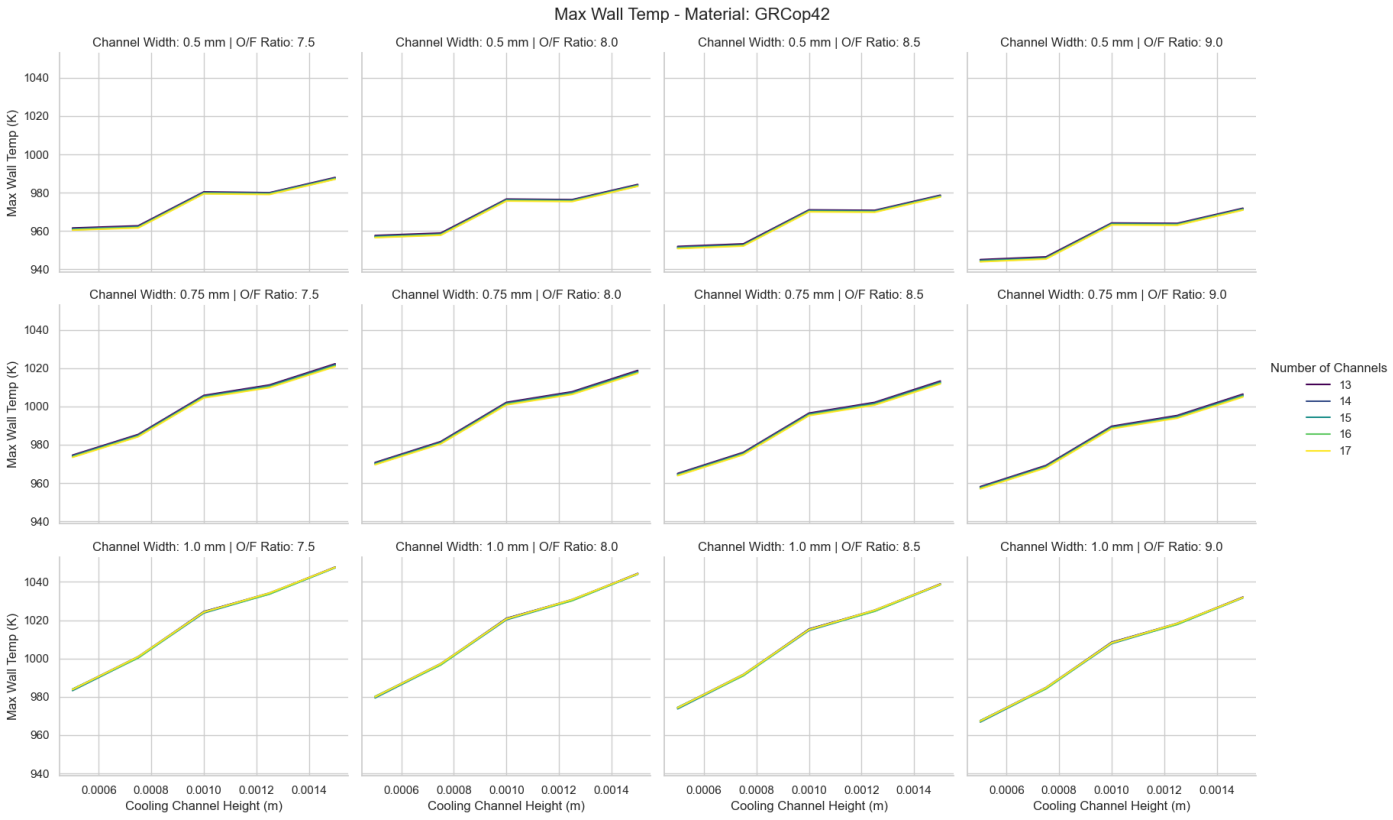

Figure 6.1: Maximum wall temperature optimization with GRCop42 as wall material

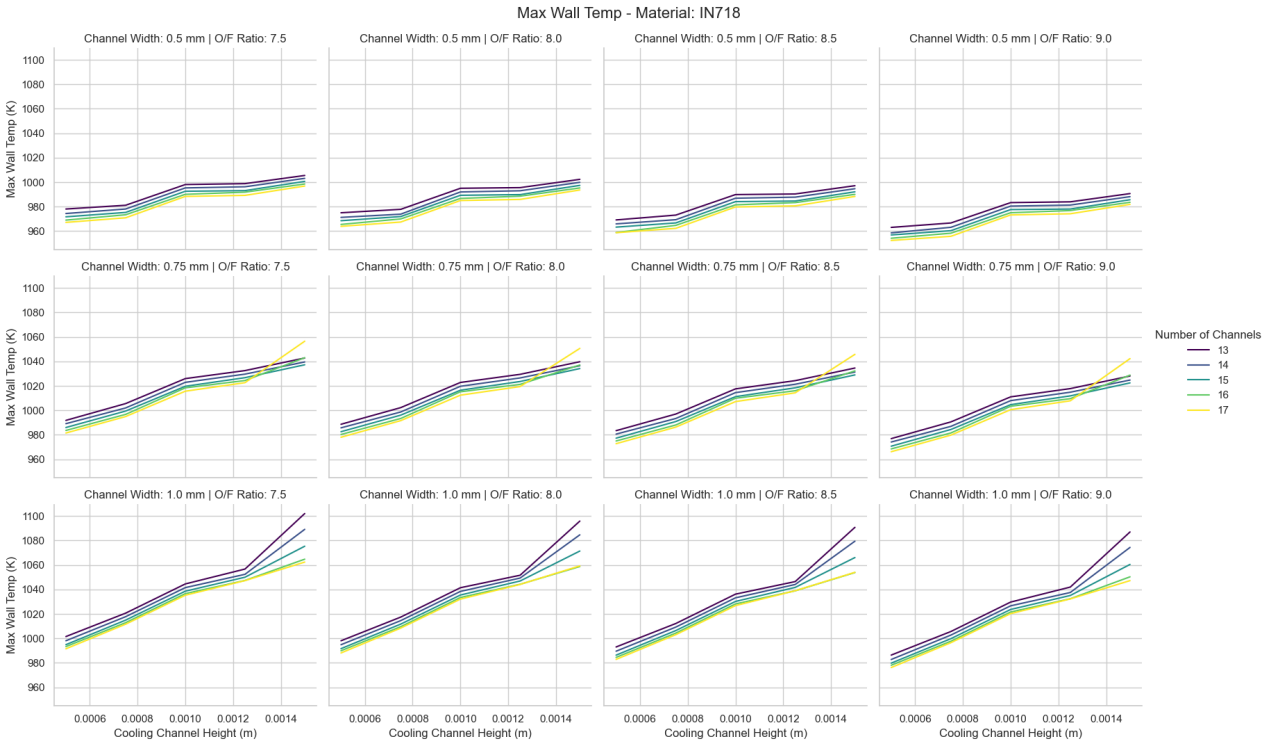

Figure 6.2: Maximum wall temperature optimization with IN718 as wall material

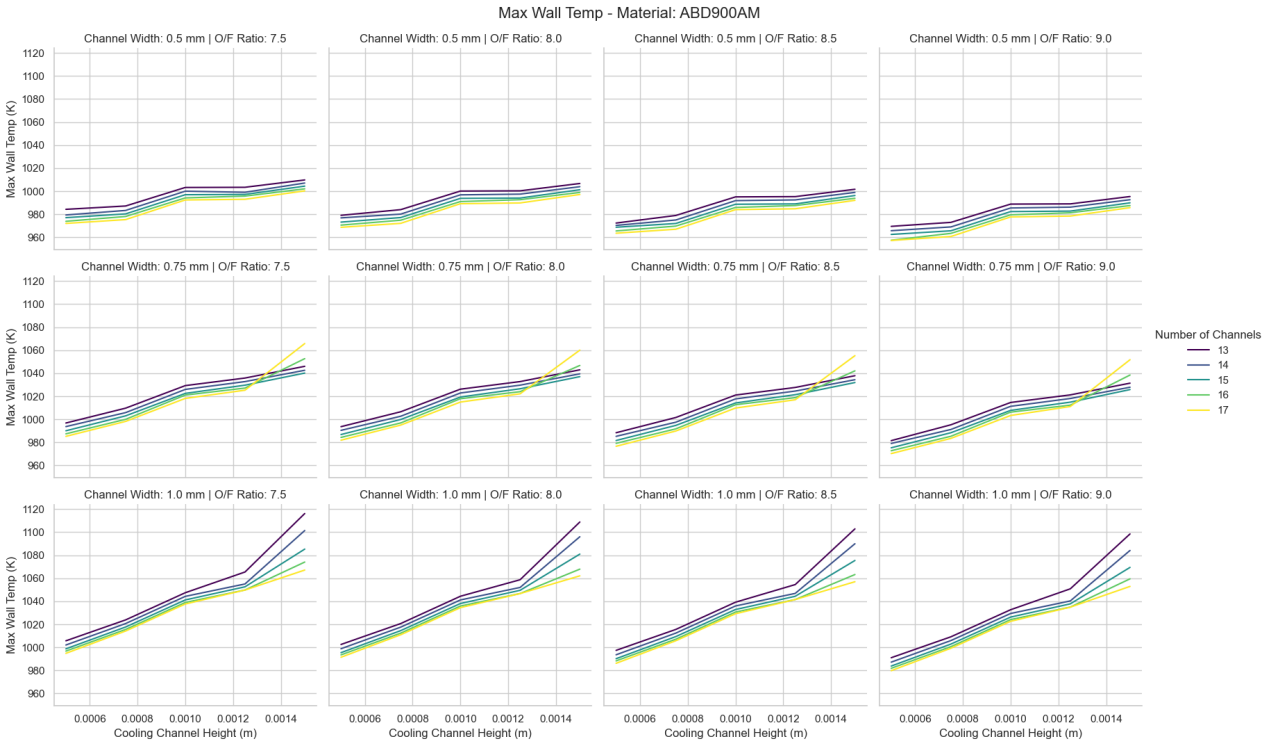

Figure 6.3: Maximum wall temperature optimization with ABD900AM as wall material

From these figures different conclusions can be drawn. First of all, depending on the specific configuration, GRCop-42 overall has the lowest wall temperature, generally with a 20 °C difference in respect to IN718 and ABD900AM. However, this still gives GRCop42 a maximum wall temperature of 943 K in the best cooling channel configuration,

which would result in a significantly lower strength then IN718 and ABD900AM. Furthermore it can be observed that due to the very high thermal conductivity of GRCop-42, the number of cooling channels does not have a big influence on the maximum wall temperature. While it is out of the scope of this thesis, something that could be further explored is using GRCop-42 in a radiation cooled engine, or using thicker inner walls to negate the stress caused by the higher temperature.

However, for this engine, based on these results, it was decided to use ABD900AM as the material, since the results were very close, but ABD900AM retains its yield strength at a temperature of around 100 °C higher compared to IN718. For the cooling channel dimensions, it was decided to go with a channel height and width of 0.5 mm and 17 channels. It should be noted that it was decided to not make the channel dimensions any smaller, as this could cause manufacturing problems. Furthermore, the number of channels could not be increased as this would result in a wall thickness of less than 0.5 mm at the throat, which was deemed as the minimum wall thickness required.

Table 6.3: Wall geometry and cooling channel parameters

Parameter	**Value**	**Unit**
Cooling Channel Height	0.5	mm
Cooling Channel Width	0.5	mm
Inner Wall Thickness	0.5	mm
Outer Wall Thickness	2	mm
Number of Cooling Channels	17	–

Once the cooling channels were optimized, the thermostructural calculations were done using the python code described before. Before performing the calculations, the location with the highest temperature gradient needed to be determined. Looking at Figure 6.5, this location seems to be at the throat. Thus, a section view of this location is taken, and the temperature gradient is used in the thermostructural calculation.

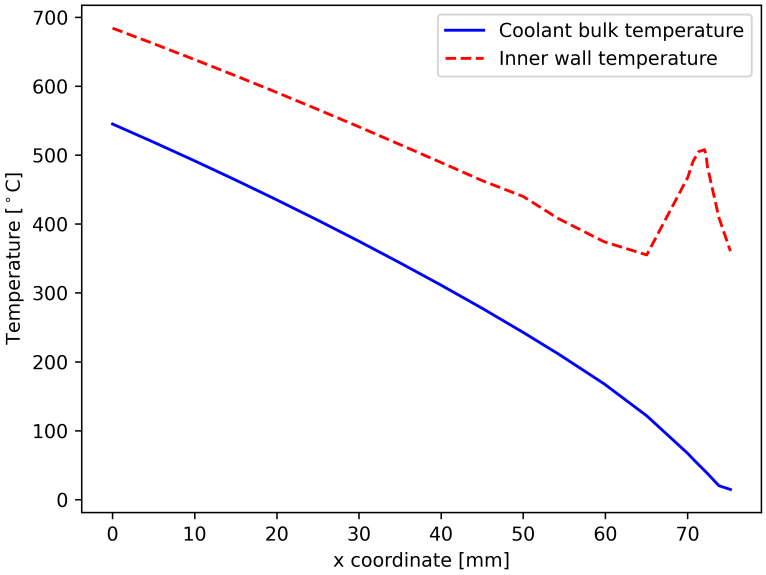

Figure 6.5: Temperature along chamber length

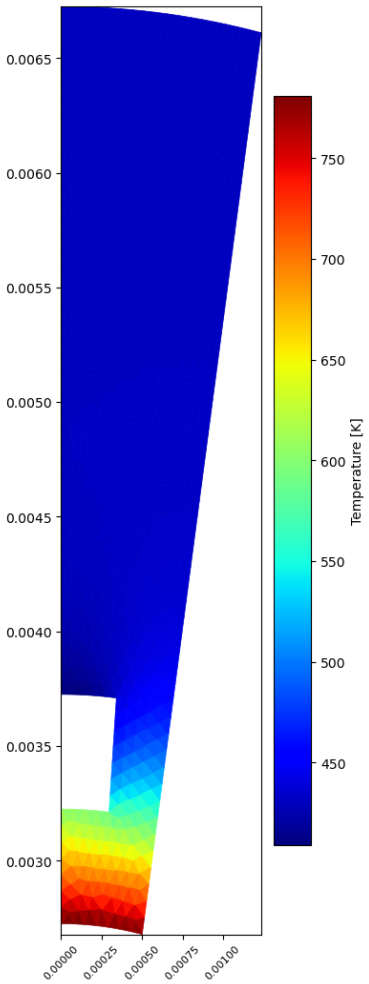

Figure 6.4: Wall temperature distribution

Apart from the temperature distribution results of the PyRocket optimization, it also gives an estimation of the total pressure along the cooling channel length. this result can be seen in Figure 6.6, where x = 0 is at the injector face.

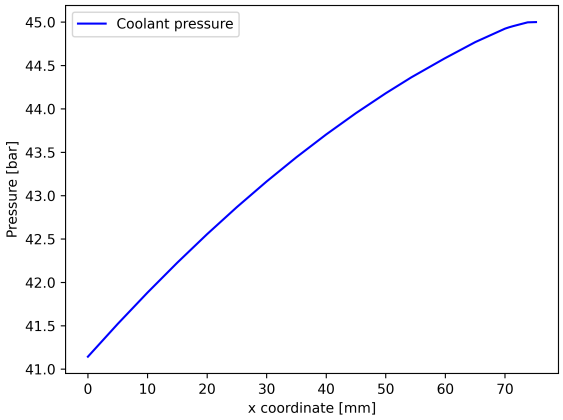

Figure 6.6: Total coolant pressure along chamber length

With the geometry, material and temperature results of the optimization, the following results are found for the cooling channel stress calculations. These preliminary results show that the thrust chamber is structurally sound, with a safety factor of 1.5, which is compliant with the requirements.

Listing 6.1: Example terminal output of stress calculations.

```
======================================================================
COOLING CHANNEL STRESS ANALYSIS RESULTS
Material: ABD-900AM Nickel Superalloy
======================================================================

STRESSES:
  Tangential Stress (Hoop):        371.82 MPa
  Longitudinal Stress (Thermal):   114.24 MPa
  Von Mises Equivalent Stress:     655.77 MPa
  Critical Buckling Stress:        7770.49 MPa

MATERIAL PROPERTIES AT WALL TEMPERATURE:
  Yield Strength:                  1002.71 MPa
  Young's Modulus:                 116.00 GPa
  Thermal Conductivity:            17.13 W/(m °C)
  Thermal Expansion Coefficient:   1.38e-05 1/°C
  Average Wall Temperature:        402.0 °C

SAFETY MARGINS:
  Tangential Stress:               2.70
  Longitudinal Stress:             8.78
  Von Mises Stress:                1.53
  UTS (Longitudinal Stress):       12.39

 Safety margins are acceptable.
======================================================================
```

Apart from the main features of the thrust chamber, it also has other features that should be mentioned. Foremost, the thrust chamber includes a pressure sensor port as well as 8 thermocouple ports. The thermocouple ports are divided in two groups, with four ports each along the axial length. The depth of the ports are different such that due to knowing the temperature at the different wall locations, the inner wall temperature can be estimated without having to insert the thermocouple inside the chamber. Secondly, the thrust chamber has two interface points. Firstly near the nozzle exit there are four threaded M2 holes, which would allow for a nozzle plug such that the chamber can be statically pressure tested, as well as six threaded M3 holes at the injection face, to assemble the thruster with the manifold. A CAD model of the thrust chamber can be seen in Figure 6.7.

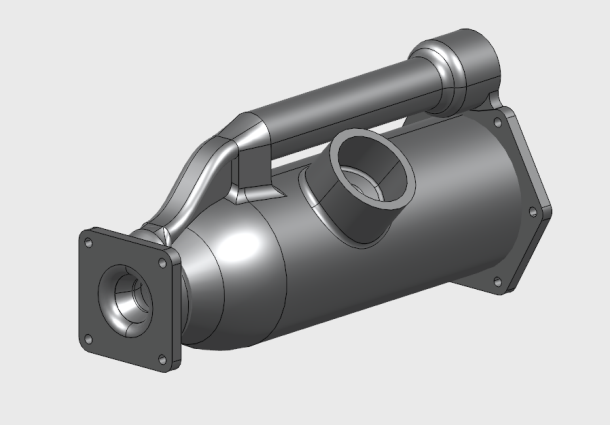

Figure 6.7: Thrust chamber CAD model

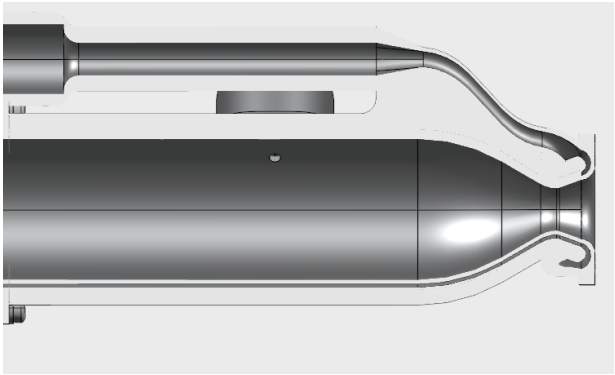

Figure 6.8: Thrust chamber cross-section view

6.1.2. Injector and Manifold

As was discussed before, three different injectors were designed. Firstly, the unlike impinging injector, secondly the "regular" coaxial swirl injector and thirdly the central coaxial swirl injector. In this section the designs of all three injectors will be shown one by one, for each injector a technical drawing can also be found in Appendix B.

For the unlike impinging injector based on geometrical and sizing considerations it was decided to use twelve elements. Based on the performance parameters of the engine, the following design was found, which can be seen in Table 6.4. Furthermore, an orifice separation (between the central and outer elements) of 1.079 mm was calculated.

Table 6.4: Geometric and Flow Parameters for Unlike Impinging Triplet Design

Parameter	**Left Orifice**	**Centre Orifice**	**Right Orifice**
Diameter (mm)	0.6264	0.4	0.6264
Tilt Angle (°)	30.0	0.0	30.0
Mass Flow Rate Per Element (g/s)	0.43165	0.09667	0.43165
Pressure Drop (bar)	1.5	1.5	1.5
Propellant Density (kg/m^3)	13.5	9	13.5

As was said before, for the unlike impinging triplet injector, the injector was integrated into the manifold. The 24 oxidizer holes are connected with the outlet of the cooling channels using eight separate channels. The fuel is inserted into the manifold through three different channels, which lead from the valve interface. The spark plug igniter can be directly inserted using a threaded interface. A CAD model of this manifold can be seen in Figure 6.9. For sealing of this configuration, only two metal o-rings are needed at the interface of the thrust chamber and the manifold. During assembly these metal o-rings need to be compressed in order to seal completely. For this reason, IN718 M3 bolts are used, as calculations performed by the manufacturer showed that this would be sufficient.

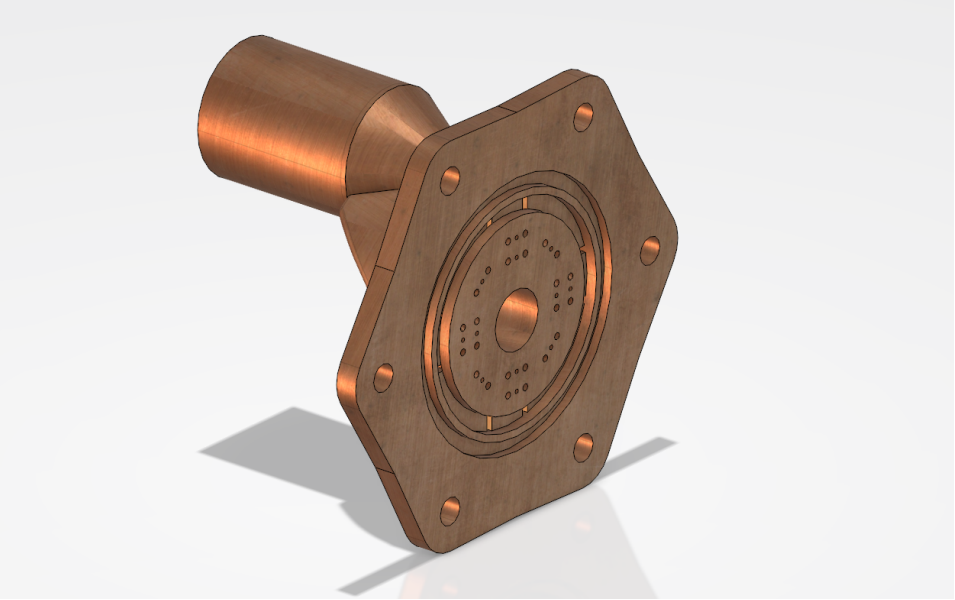

Figure 6.9: Unlike impinging manifold

For the swirl injectors, the designs are nearly identical, with the only parameter that is varying is the vortex chamber radius for both the inner and the outer element. Thus, the design will be given in two tables, one for the central injector and one for the regular off-center injector.

Table 6.5: Geometric and flow parameters for central coaxial swirl injector

Parameter	**Inner Element**	**Outer Element**
Geometric Parameters		
Nozzle Radius (mm)	5.538	7.258
Outer Nozzle Radius (mm)	6.538	—
Vortex Chamber Radius (mm)	5.755	7.604
Tangential Inlet Radius (mm)	0.395	0.745
Number of Inlets	4	6
Flow & Performance		
Mass Flow Rate (kg/s)	0.00116	0.01042
Pressure Drop (bar)	1.50	1.50
Fluid Density (kg/m^3)	9.00	13.50

The table above shows the main dimensions of the central coaxial swirl injector. Here, it should be noted that the outer oxidizer element of this injector would be integrated into the manifold, while the inner fuel element is a separate part. The CAD model of this configuration can be seen in Figure 6.10. For sealing, the coaxial swirl injector itself will have three grooves, two grooves for two 12.5 mm x 1 mm FKM O-ring and one groove for an 12 mm x 1 mm FKM O-ring. The manifold will use two metal o-rings due to the high temperatures and stresses. The igniter will be sealed by very tightly torqueing it against a tapered face.

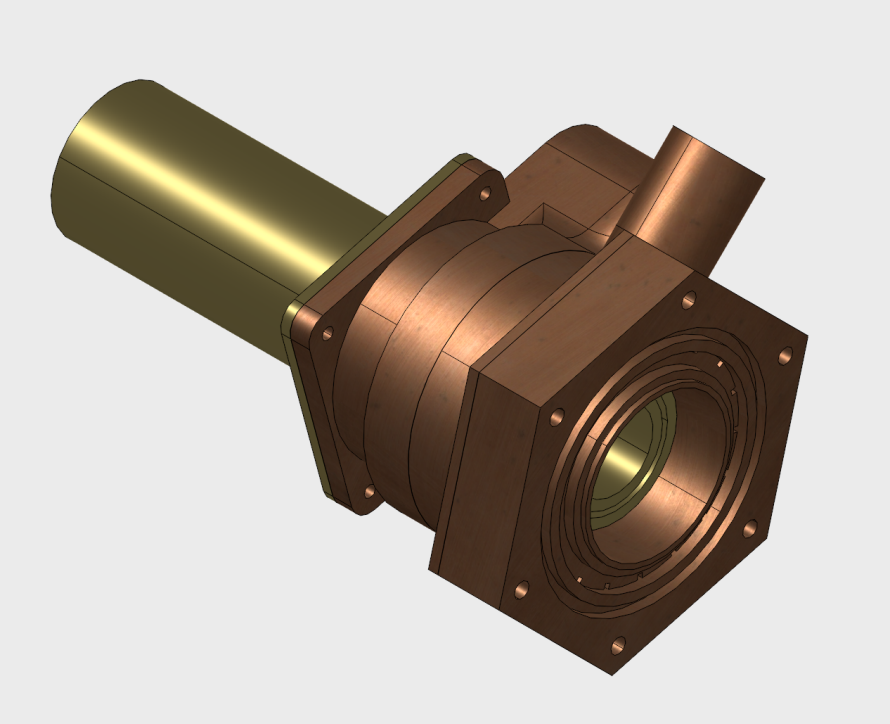

Figure 6.10: Central injector and igniter manifold

For the off-center coaxial swirl injector with the glow plug, a custom manifold was designed that could house both the injector and the igniter as separate parts. However, the injector has to be brazed, which would mean it could not be replaced after. The CAD models of the injector and the manifold with integrated injector can be seen in Figure 6.11 and Figure 6.12 respectively. For sealing here, the igniter will be sealed in the same way as the central configuration, except here it will be within the injector itself. The only two (metal) O-rings present in this configuration are at the thrust chamber interface, similar to the previous configuration.

Table 6.6: Geometric and Flow Parameters for off-center Coaxial Swirl Injector

Parameter	**Inner Element**	**Outer Element**
Geometric Parameters		
Nozzle Radius (mm)	1.272	4.056
Outer Nozzle Radius (mm)	2.272	—
Vortex Chamber Radius (mm)	3.186	5.000
Tangential Inlet Radius (mm)	0.335	0.645
Number of Inlets	4	5
Flow & Performance		
Mass Flow Rate (kg/s)	0.00116	0.01042
Pressure Drop (bar)	1.50	1.50
Fluid Density (kg/m^3)	9.00	13.50

It should be noted here that the outer element of the off-center coaxial swirl injector only has five inlets, instead of six. This was done for manufacturing reasons, in order to fit the coaxial swirl element together with the igniter into the manifold.

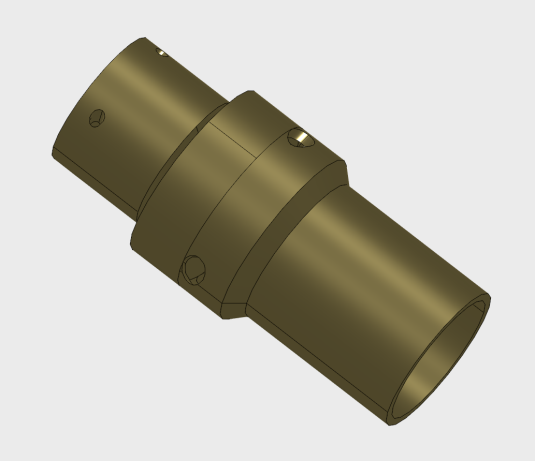

Figure 6.11: Coaxial swirl injector

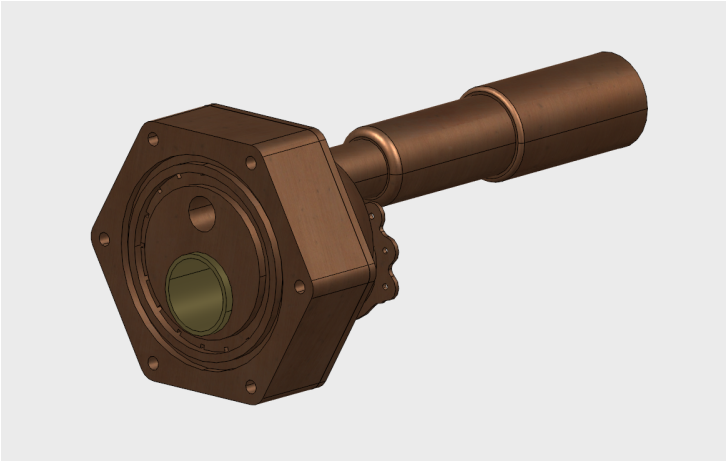

Figure 6.12: Off-center injector and igniter manifold

For the igniters, the unlike impinging configuration will use the Pichler Modellbau 1/4-32 Spark Plug (Pichler, 2026). The off-center coaxial swirl and central coaxial swirl configurations will use the Maxgear 66-0091 glow plug (Autodoc, 2026). The spark plug was selected due to its easy availability and small form factor. The glow plug was selected as it has a ceramic tip, which was shown to be capable of reaching higher temperatures (section 2.5). Furthermore, it has a small form factor and also has good availability.

6.2. Manufacturability

Near the latter stages of the thesis, manufacturing companies were contacted in order to have a better understanding of the manufacturability of the engine, and if any changes should be made to the design. In this section the outcomes of these discussions will be shortly discussed, focusing on what changes have been made, and what changes should still be made after the thesis has been finalized. Furthermore, any considerations made with respect to manufacturability in the initial design process will also be elaborated on.

6.2.1. Manifolds and injectors

As the design of the manifold, the integration with the igniter, the injector, and the valves is very complex, assessing manufacturability is a crucial, if not the most crucial part of the process. Thus, during the design, multiple changes were made in order to make the manifold and coaxial swirl injector easier to manufacture. The most design iterations were done on the central coaxial swirl injector manifold. Due to the complex geometry, it was decided to fully additively manufacture the manifold, and solely machine the coaxial swirl injector itself. Initially, the entire coaxial swirl injector was meant to be machined however eventually it was decided to integrate the outer “oxidizer part” of the coaxial swirl injector with the manifold, and only machine the inner coaxial swirl injector parts. It was decided to not additively manufacture the “fuel part” of the coaxial swirl injector, in order to have the ability to easily change this part if the fuel was changed. This way the manifold design can stay the same, and simply the tangential inlet holes needed to be changed depending on the mass flow and density of the fuel.

For the sealing, the manifold was initially designed to have five O-Ring grooves, two for the fuel swirl injector interface, one for the oxidizer injector interface and two for the thrust chamber-manifold interface at the cooling channels. However, after discussion with ESA, this was reduced to only the two grooves at the thrust chamber interface, and the three other grooves were instead moved to the coaxial swirl injector itself, as it was deemed more straightforward to machine those grooves on the outside of the swirl injector rather than having them additively manufactured in the manifold.

Finally, for the unlike impinging manifold, after discussion with the machinists from ESA, some changes were also made. As the orifice diameter of the injector is very small, a concern was brought up that the roughness of the additively manufactured part would have too big of an impact on the alignment of the jet streams, which could cause efficiency loss and poor mixing. Thus, it was decided to additively manufacture only part of the injector channel, and have the last few millimetres remain solid. Then, during the post-processing, the machinist can drill the holes using microdrilling, improving the roughness of the part. However, to be able to achieve this, an additional face needs to be

added to the front of the manifold, as it would not be possible to drill the holes at an angle. This way, the machinist can cut off an angular face, ensuring the drill bit is drilling straight into the manifold.

6.2.2. Thrust chamber

For the thrust chamber, both during the design process and after the design changes were made based on the manufacturability. Firstly, using regenerative cooling, the size of the cooling channels is a critical aspect of the design. However, with a small-scale thruster, keeping the cooling channels large enough, while still retaining the cooling capability with a small mass flow is a difficult trade-off. Thus, early in the design process, an additive manufacturing entity was contacted in order to decide the minimum cooling channel dimensions in order to remain manufacturable. From these discussions, a minimum of width/height of 0.5 mm was found.

Another change that was made on the design was the flange/interface geometry. Based on discussions with the machinists at ESA, it was decided to make the flange a square geometry, in order to make the post-processing easier. Furthermore, supports were added to the design in order to make the geometry printable. However, upon progressing with the manufacturing authority, more supports might need to be added.

6.3. Verification

In the following section, the results from both the CFD analysis of the thruster and the FEM analysis will be shown. After this, some conclusions will be drawn. Validation of the CFD simulation and comparison to experimental results is not performed as the thesis was finalized before the experiments began. However, the results will be compared with the thermal simulations performed during design, and different trends can be compared with existing public data.

Both the CFD and FEM simulations were performed using Ansys (Fluent and Mechanical), and the post-processing was done in Paraview. For the simulations themselves, the DelftBlue supercomputer from the TU Delft was used in order to perform a transient CFD simulation with a large number of time steps and also in order to use a fine mesh for the FEM simulation.

6.3.1. CFD Results

From the CFD simulation there are multiple parameters that can be viewed. The simulation is mainly used to verify the performance of the thruster with the design parameters that were found in the RPA design and the PyRocket optimization performed beforehand. As there are no material properties related to stress and no fixed joints assigned, this simulation does show any structural parameters. However, one crucial parameter that can be seen is the temperature. While stresses can't be seen, the maximum inner wall temperature should still be low enough in order for the material to retain its strength properties.

Foremost, the performance parameter should be verified. These parameters are thrust, chamber pressure, specific impulse and characteristic velocity. When these values are found, some efficiencies can be calculated as well. It should be noted that the mass flow is an input of the CFD simulation and therefore is not shown as a result. Apart from the performance of the thrust chamber, the performance of the swirl injector in terms of flow pattern and mixing should also be analysed. Firstly, the (absolute) chamber pressure can be seen in Figure 6.13.

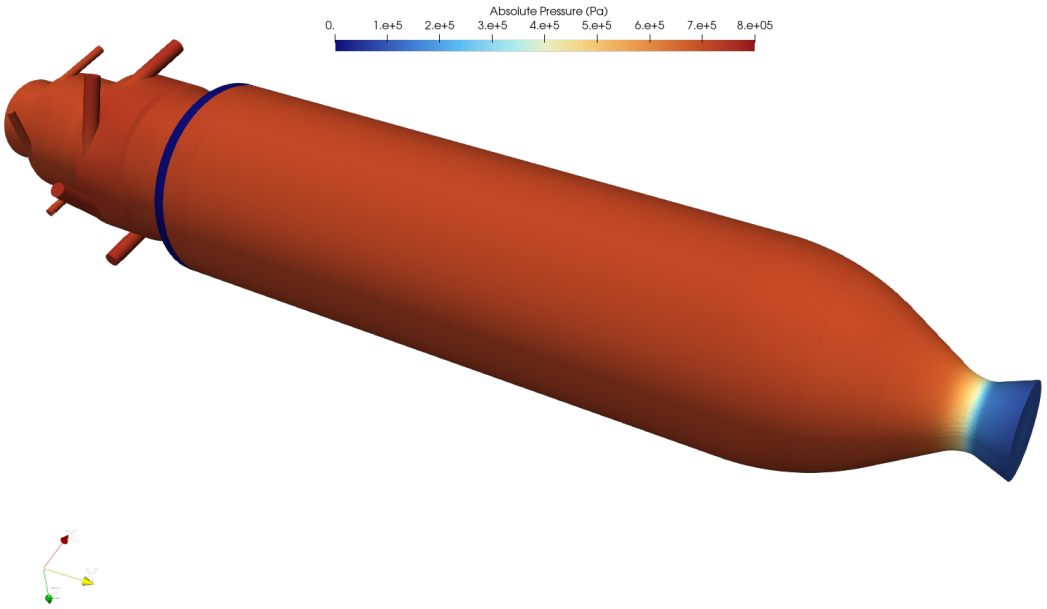

Figure 6.13: Absolute pressure distribution at chamber wall

When probing the absolute pressure in the combustion chamber region, it is found that the chamber pressure is around 7.1 bar, which is a bit lower than expected, however it is still within the allocated margin of the pressure requirement. It can also be seen that the pressure drop is very low, only around 0.5 bar. However, most likely Ansys underestimates the pressure, drop. Still, this is something that should be verified in future experimental tests.

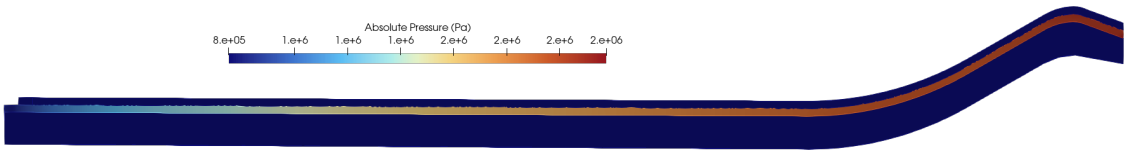

Figure 6.14: Cooling channel absolute pressure

In the figure above, the absolute pressure along a cooling channel can be seen. This shows a pressure drop of 12 bar, which is significantly larger than the 3-5 bar that was found in the PyRocket optimization. Furthermore, with very small additively manufactured parts, the roughness of the material can increase the pressure drop even more. Thus, this is a point of concern that should be verified with experimental testing. However, a reason for this large pressure drop could be a flaw of the CFD simulation. As the coolant domain and the main flow domain are split, the coolant domain has a separate outlet. This outlet is a ring at the interface point between the thrust chamber and the manifold. In Ansys Fluent, the inlet pressure is not assigned (only the mass flow). Rather, the software calculates the inlet pressure for an assigned outlet pressure. In this simulation, the outlet pressure was assigned to be around 1-1.5 bar higher than the chamber pressure, to account for the pressure drop. Thus, as the channel geometry drastically increases at the outlet, it could be that Ansys overestimates the inlet pressure. This result is most likely unreliable and should only be used for illustrative purposes. For future studies, it is recommended to either connect the cooling channel and main flow domains, or have the cooling channel domain geometry stay constant across the entire domain, in order to have a realistic result. For this thruster the actual pressure drop should be measured during testing at ESA. Furthermore, it was concluded with the European Space Agency that another thrust chamber should

be made with a cooling channel height of 1 mm, in order to compare the results.

In order to calculate the thrust, characteristic velocity and specific impulse, the exit velocity should be analysed. In order to do this, the absolute velocity contour plot was plotted in the YZ plane, and can be seen in Figure 6.15.

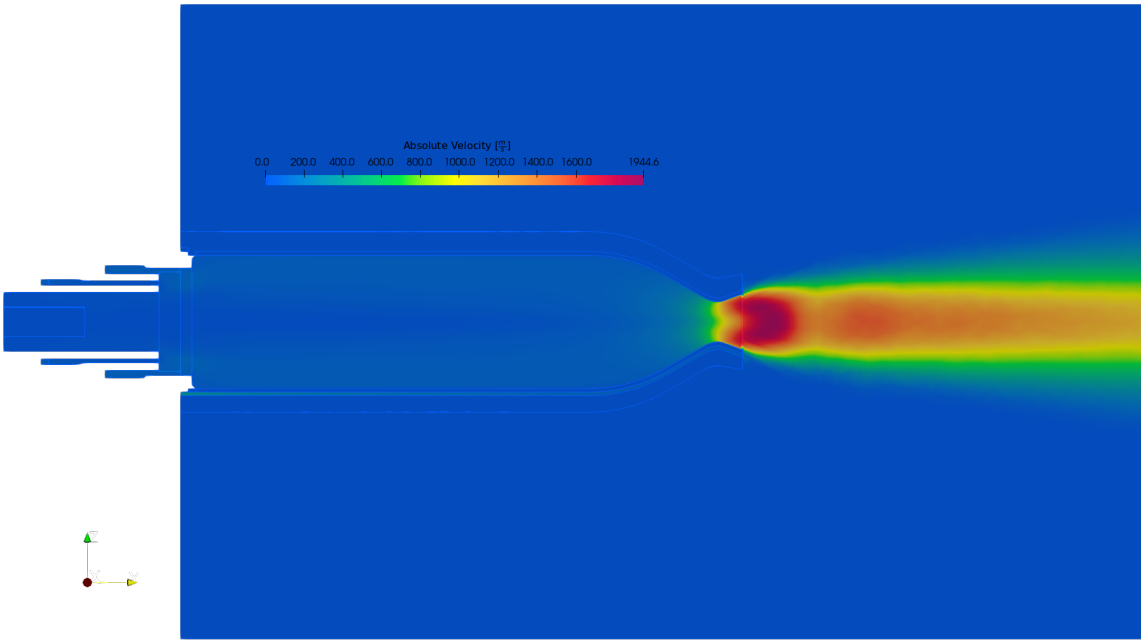

Figure 6.15: Absolute Velocity in YZ plane

In this figure, it can be seen that the highest velocity at the exit is 1944.6 $\mathrm{m\,s^{-1}}$. Furthermore, the mass flow through the nozzle exit is found to be 0.011 61 $\mathrm{kg\,s^{-1}}$ (slightly, higher than the design mass flow) and the nozzle is perfectly expanded into 1 atm (as could be seen in Figure 6.13). To calculate the thrust, the integral of the axial velocity should be taken across the nozzle exit area. From Ansys Fluent a value of 1569.1 $\mathrm{m\,s^{-1}}$ was found. With this value, the thrust can be calculated using the following equation:

$$F = \dot{m}\, v_e = 0.01161 \cdot 1569.1 = 18.22\ N \tag{6.1}$$

This shows that the thrust is slightly lower than the design thrust, however this is likely due to the lower chamber pressure. During physical testing tests should be performed at higher inlet pressures in order to see the impact on the thrust. From this thrust, the specific impulse can be calculated:

$$I_{sp} = \frac{F}{\dot{m}\, g_o} = \frac{18.22}{0.01161 \cdot 9.81} = 159.95\ s \tag{6.2}$$

Due to the thrust being lower than the design thrust, the specific impulse is also lower. Thus, most likely, the realistic specific impulse will be higher than what is found in the simulation. Physical hot-fire tests are needed in order to confirm that the thruster can obtain the minimum specific impulse as was specified in the requirements.

Apart from the performance parameters, the inner wall temperature is another crucial parameter that should be analysed in order to ensure that the temperature does not surpass 1100 K, after which the properties of ABD900AM quickly degrade (as could be seen in Appendix A.1). In this simulation the maximum wall temperature was found to be 936 K, where the overall distribution can be seen in Figure 6.16. Which is well below the 1100 K limit, however FEM analysis needs to confirm that the stresses inside the chamber are not too high.

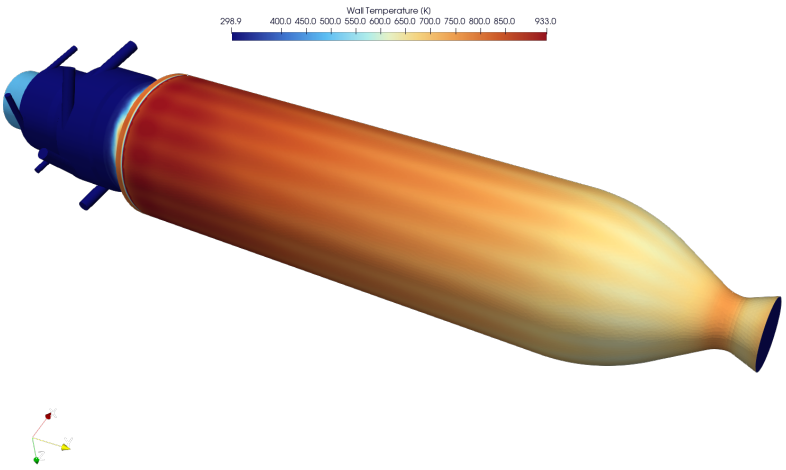

Figure 6.16: Combustion chamber inner wall temperature distribution

From this distribution it can be seen that the highest temperature occurs at the inlet, with a small peak at the throat. This was expected, as was previously found in the PyRocket simulation in Figure 6.4. What should be noted is that due to assuming complete and instant combustion (depending on the mixture fraction), the temperature at the inlet is likely overestimated. In Figure 6.17, a scatter plot can be seen of the surface heat flux along the axial direction, where, as expected, the heat flux at the throat and at the injector are the highest. As Ansys Fluent assumes instant and complete combustion, the heat flux at the injector is most likely overestimated. The heat flux at the throat might also be slightly overestimated, but is probably more accurate.

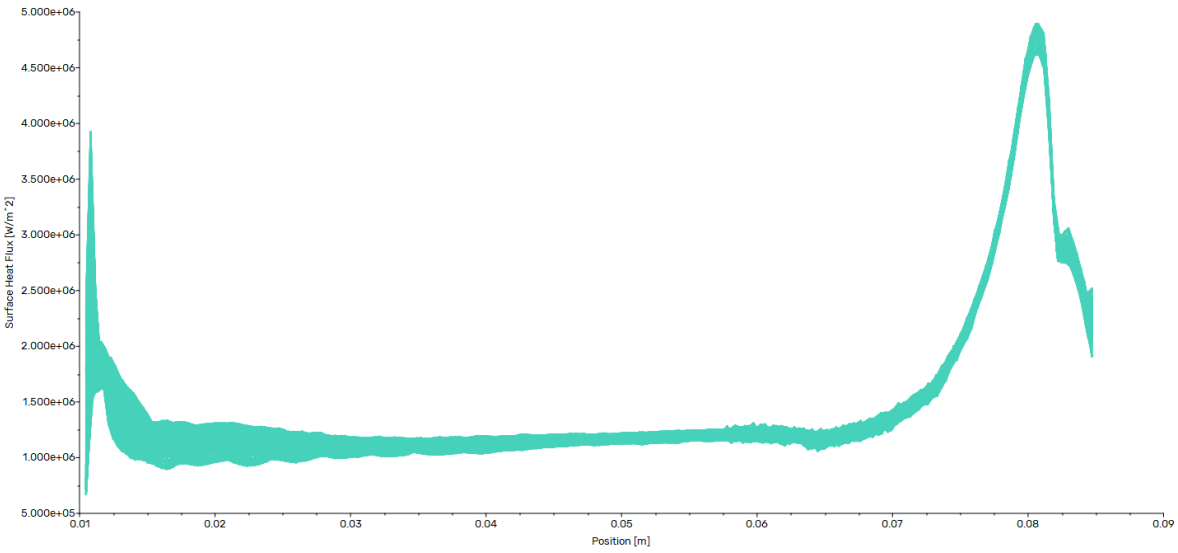

Figure 6.17: Surface heat flux combustion chamber inner wall along axial direction

In order to visualize the flow of the simulation, a pathlines can be generated within Ansys Fluent. This gives an illustration of the swirling effect, the spray pattern and the flow within the injector itself. The pathlines can be seen in Figure 6.18.

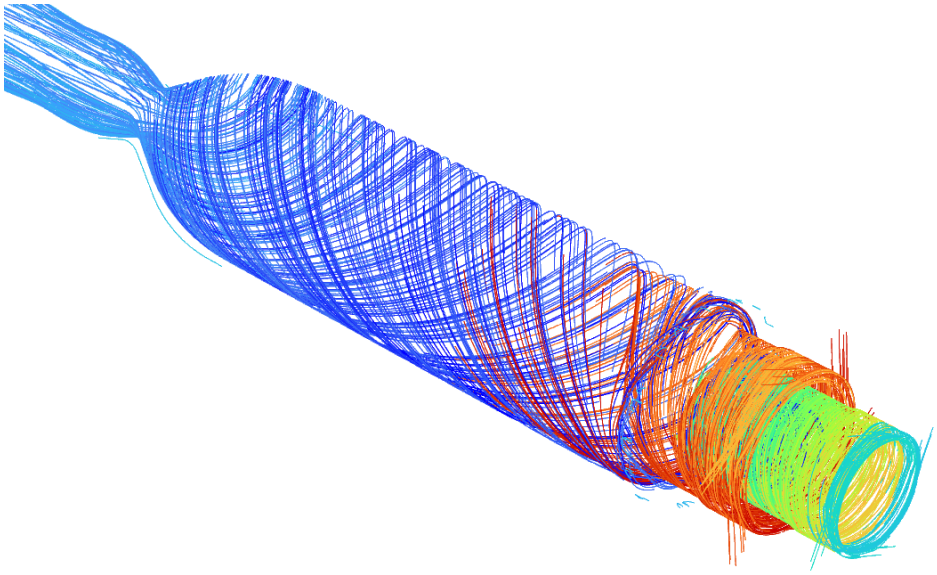

Figure 6.18: CFD simulation pathlines

This shows that the swirling effect performs well, in order to see the mixing of the fuel and oxidizer at the injector, the following vector plot in Figure 6.19 is generated. It should be noted that the z-component of the vector has been omitted, in order to properly show the impingement point and flow direction.

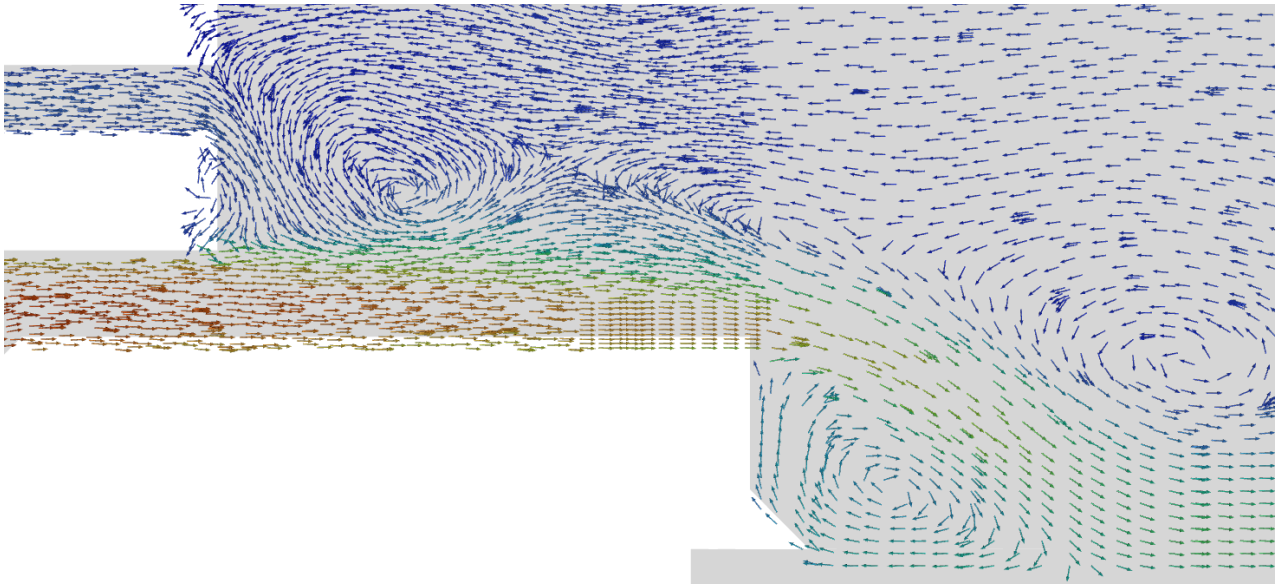

Figure 6.19: Flow vectors at injector

This plot shows that fairly quickly after the fuel enters the main chamber, the swirling flow impinges with the oxidizer flow. While the vortex chamber was designed to have an impingement point further downstream, this does not necessarily have to be an issue, but this should be validated during future injector cold flows. This plot shown above is for the case of a cold flow, where the combustion was “turned off” in Ansys Fluent. In Figure 6.20, a contour can be seen of the mixture fraction, after the combustion was “turned on”. Here, a mixture fraction of 1 represents pure fuel, a mixture fraction of 0 represents pure oxidizer.

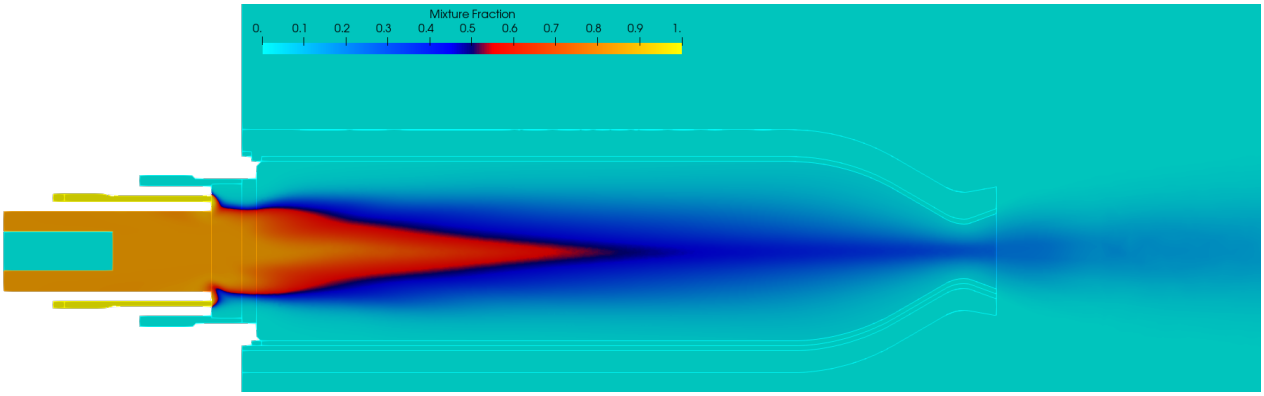

Figure 6.20: Mixture fraction contour plot

As Ansys Fluent essentially assumes instant combustion upon mixing at the injector, the mixture fraction is likely not completely realistic. Still, it can give some estimation of the mixture distribution along the chamber length.

6.3.2. FEM Results

Based on the final temperature and pressure results of the Ansys Fluent simulation, a static structural simulation was performed in Ansys Mechanical. It should be noted that the simulation is not a transient simulation, thus structural effects that are time dependent are not taken into account in this simulation. Furthermore fatigue is also not measured. The main results that were analysed were the principal stresses in the bolts and the thrust chamber itself.

For the bolts, Inconel 718 was used as the material. In order to ensure physical testing could be done safely, a minimum safety factor of 1.5 was chosen. This safety factor was calculated in the following way:

$$SF = \frac{\sigma_{vm}}{\sigma_{yield}} \tag{6.3}$$

As Ansys does not allow for varying the yield strength with temperature, the data was post-processed using python and the graphical plotting was done in Paraview. For the yield strength-temperature graph the datasheet for ABD900AM was used, which can be seen in Appendix section A.1. To make the post-processing easier, the graph was used for the entire geometry, including the IN718 bolts. As the yield strength of IN718 is actually higher than ABD900AM at temperatures below 600 °C, this was an appropriate assumption. In Figure 6.21 a cross-section view of the thrust chamber, the flange and two bolts can be seen.

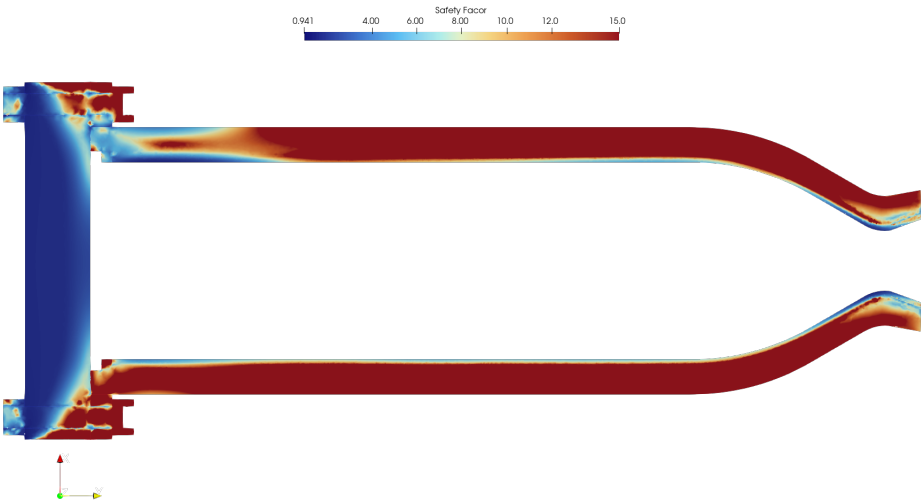

Figure 6.21: Safety factor distribution along cross-section of the thrust chamber

Probing the values in this figure, the minimum safety factor value of 1.5 is not exceeded almost anywhere in the thruster assembly. This only happens at two locations, as can be seen more clearly in Figure 6.23 and Figure 6.22. These locations are the corners of the fixed flange, and some hot spots at the inner wall of the chamber. However, both locations do not necessarily have to be a problem. For the inner wall hot spots, the minimum safety factor reaches a value of around 1.4, which is lower than desired but still above the yield strength of the material. Furthermore, it needs to be confirmed with testing if the wall will actually undergo this stress, as the temperature of the CFD is likely overestimated, as was stated before in subsection 6.3.1. Regarding the stress at the corners of the flange, this is a bit more critical, but can also be explained. Firstly, the temperature was not calculated in the CFD, and was inserted as a constant 500 °C across the entire flange. While this is most likely a good estimate for the part near the chamber, it is most likely not a good estimate for the side furthest from the chamber. Also, the coolant flow has not been taken into account here, which will likely have a cooling effect on this part. Taking all this into account, the safety factor will be very likely above 1, but likely not 1.5. Thus, in future iterations of the design, a recommendation would be to increase the thickness around the bolted interface, and testing rigorously to ensure the flange does not fail. Another location that should be noted is the throat, where the safety factor reaches a value just above 1.5. After hot-fire testing, the throat should therefore be inspected in order to see if the material has degraded.

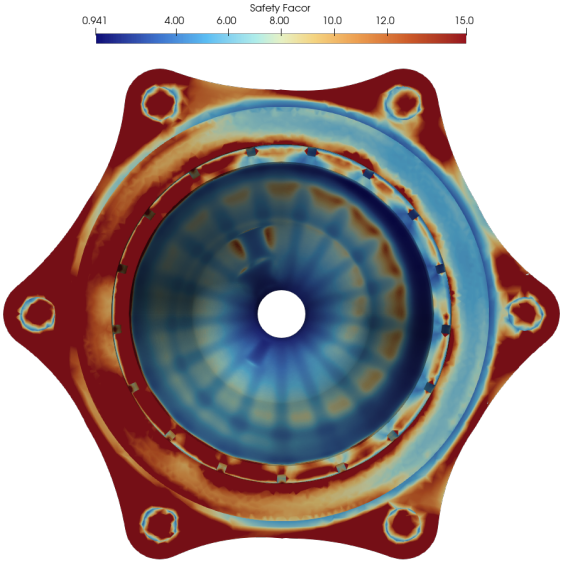

Figure 6.22: Safety factor distribution aft view

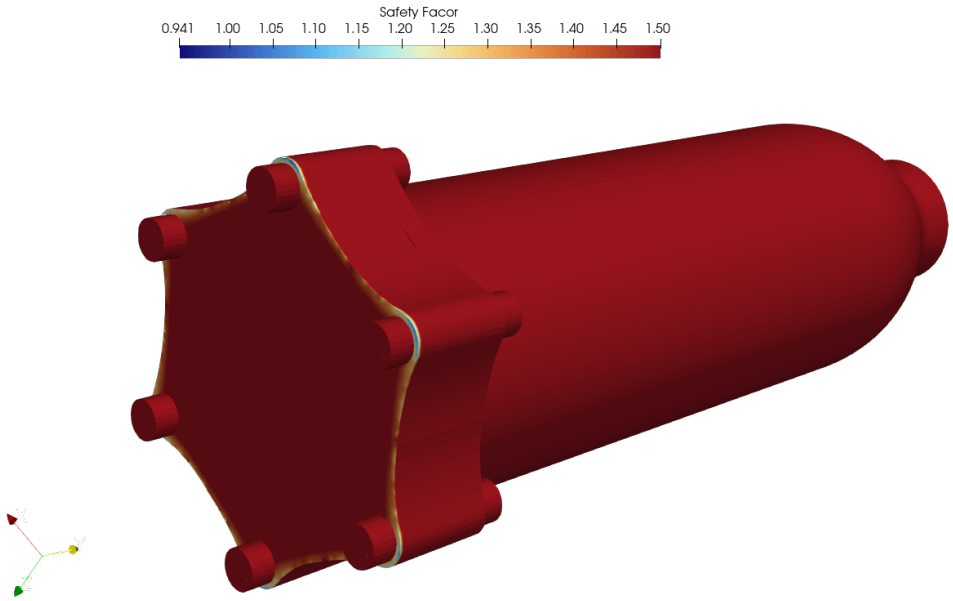

Figure 6.23: Minimum safety factor isometric view

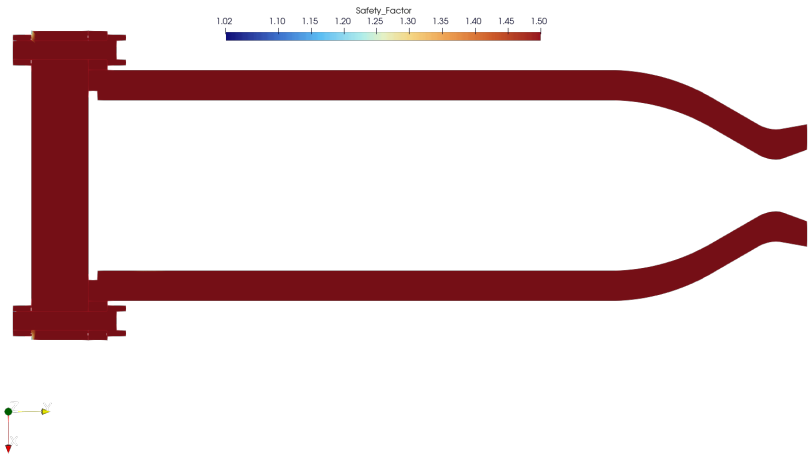

Figure 6.24: Safety factor section view (clipped to 1.5)

In Figure 6.23 and Figure 6.24 above, the data range has been manipulated to a maximum of 1.5 in order to show the critical stress locations. Especially in Figure 6.24 it can be seen that the minimum safety factor of 1.5 is not exceeded in the chamber wall. However, increasing the data range to a safety factor of 15, the following distribution can be seen in Figure 6.25.

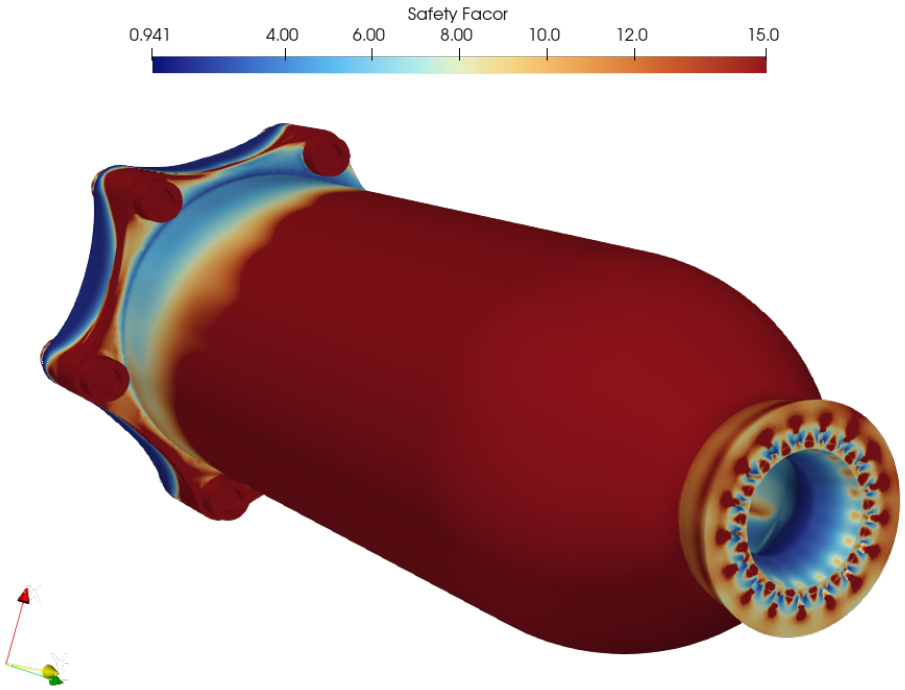

Figure 6.25: Safety factor full range isometric view

7
Conclusion and Recommendations

Concluding the thesis, the design of three different thruster configurations has been performed. However, some more work has to be done in order to completely verify the thruster, and verify the simulation results. Furthermore, depending on the feedback of the manufacturing entities, changes to the design could also still be made. In this chapter the design, as well as the verification process and results will be discussed. In the next chapter future recommendations will be given based on the work that has been performed.

7.1. Research Questions Conclusions

At the beginning of the thesis, a total of five research questions needed to be investigated. In the following paragraphs each question will be elaborated on.

How can a thruster architecture be designed to allow for the interchange of different fuels, injector concepts, and ignition systems while remaining leak tight, without performance loss and failure-proof?

During the design of the thesis, multiple decisions were made to show the thruster architecture is modular. Firstly, two different types of injectors were used. These are a coaxial swirl injector and an unlike impinging injector. The coaxial swirl injector was mainly chosen due to its good properties, and more novel method of injection. While the unlike impinging injector was mainly chosen to show the modularity, as well as that it is a reliable injector with a large heritage in rocket engines.

For the igniter, similarly like the injector, two different types of igniters were chosen for the design. Again, similarly like the injectors, the glow plug was chosen for its good properties and novel architecture. While the spark plug was chosen to show modularity and have reliability at the same time. Furthermore, as this engine will be used by ESA to do research on a test bench, it gives a good comparison case between both igniters.

Finally, the fuel has been kept constant across all designs. However, very little has to be changed to the design in order to change the type of fuel. Since nitrous oxide is the fixed oxidizer, for the coaxial swirl injector configuration only the fuel element of the coaxial swirl injector has to be changed. Specifically the tangential inlet geometry has to be resized, and for the unlike impinging injector either the manifold has to be remanufactured with a different orifice size, or it can be kept the same, depending on the fuel.

Eventually, there was not enough time in the thesis to perform physical tests, which would be demonstrating that the thruster configurations were failure-proof, leak-tight and without performance loss. However, a verification plan was made in section 5.3, which lays the groundwork for any future tests that will be performed by ESA.

What design features are critical to optimizing pulse-mode performance, specifically to achieve a low minimum impulse bit, minimize propellant dribble volumes, and ensure pulse-to-pulse repeatability?

One of the project requirements given by ESA was to make the thruster be capable to operate in pulse mode. With this in mind, the thruster and the relevant components were designed and selected. For achieving pulse mode two components are critical, namely the valves and the igniter. For the valve, which were outsourced, as can be seen in section A.2, the minimum response time of 15 ms was set as a critical requirement. Furthermore, the igniters have also been selected with the pulse mode capability in mind. Spark plugs have a nearly instant response time, while glow plugs take a longer time, namely around 7.2 s for ceramic glow plugs, as was shown by Breisacher and Ajmani, 2009. However, glow plugs function by heating up the chamber atmosphere. Thus, since the pulses occur rapidly after each other, only for the first pulse a longer heating period is necessary, after which the chamber is already heated and

pulses can ignite easily. But, testing is still necessary to see the functionality of glow plugs in pulse mode.

Another important part of firing a thruster in pulse mode is the dribble volume. This volume can be related to the length of the path that the propellants must follow before the combustion chamber is reached. In order to keep this volume to a minimum, the valves are directly inserted into the thrust chamber and manifold for the oxidizer and fuel respectively, and the flow paths in the thruster and the manifold have been optimized. To verify the actual minimum impulse bit and thus the minimum pulse time, a pressure sensor has been placed in the combustion chamber. This way, the minimum impulse bit can be measured with great accuracy.

With what methods can the heat loads on the thruster be measured, and how do they compare to both (other) experimental and analytical values?

In order to verify the structural integrity of the thruster for either longer duration, or high-cycle firings, the temperature of the thrust chamber wall should be verified. To be able to achieve this, the thrust chamber has been designed to include eight thermocouples along a pattern in the combustion chamber. There are two holes for four axial locations, each one placed in the middle between two cooling channels. This has the least effect on the structural integrity, and also measures the highest heat loading. To be able to interpolate the heat loading measured by the thermocouples to the very inner wall, each axial location has two thermocouples placed at two different heights in the chamber wall. One thermocouple is placed at 0.5 mm from the chamber one, while another thermocouple is placed 1.5 mm from the inner wall. An illustration of this can be seen in Appendix B.

Apart from this, three pressure sensors will also be present in the flow. One at each propellant valve port, as well as an integrated pressure sensor in the manifold. If desired, a pressure sensor could be included which can also measure temperature. Experimental tests still have to be performed with the thruster, thus a comparison with the analytical values found from the CFD can't yet be performed. However, a verification plan was written in section 5.3 which outlines the steps that should be taken to verify the temperatures.

Which combustion chamber material and cooling method would allow for steady-state firing of this thruster?

In this thesis, multiple combustion chamber materials and cooling methods were considered. After a trade-off, regenerative cooling was selected as the best option for this thruster. Other cooling methods such as ablative cooling, radiation or transpiration cooling were either deemed not sufficient for reusability/pulse mode firing, or it would not be sufficient for achieving a steady-state hot-fire. Film cooling was considered as an option that could be used in combination with regenerative cooling, however eventually was not used as it was deemed not necessary, based on the outcome of the simulations. Furthermore, it would make the thruster design unnecessarily more complex, and could influence the modularity of the thruster.

For the material, also a trade-off was performed, however this lead to three materials. ABD900AM, IN718 and GRCop-42. Based on these materials, a thermal simulation had to be performed, utilizing regenerative cooling, which would eventually show that ABD900AM would be the best option, due to its superior strength compared to the other options at high temperatures. Furthermore, these simulations also lead to a geometry of the cooling channels and inner/outer wall thickness, as could be seen in Table 6.3. The geometry that was found let to a maximum wall temperature of around 680 °C at the inlet. After these simulations, also a transient CFD simulation was performed. This simulation showed promising results, with a maximum wall temperature of 663 °C.

Based on the geometry and the CFD simulations that were performed, a FEM analysis was performed in order to verify the structural integrity. Upon advice of the European Space Agency, a minimum safety factor of 1.5 was adhered. After the simulation, a few critical points were found where the safety factor is below this value of 1.5. Firstly, at the corners of the fixed flange. This could have multiple reasons, but physical tests should verify this value. Furthermore, a constant temperature of 500 °C was applied, which most likely will be less at those corners. Apart from this, another point of attention is the hottest point at the inner wall, where the safety factor reaches just below 1.5. This should not be an issue for a single test, however for longer duration, high-cycle tests this could be an issue. Therefore, a suggestion is to perform an inspection after the first longer duration tests, to see if the material degrades or deforms after these tests. This should also be done at the throat, where the safety factor is just above 1.5.

How can the thruster design be optimized to be manufacturable and within budget?
After the initial design, the CAD model and dimensions of the thruster were discussed together with ESA machinists. This was done in order to analyse the manufacturability of the thruster, and if changes should be made to the design before the manufacturing process should start. Furthermore, during the design process itself, manufacturability was taken into account. Since the thruster is not a flight version, mass optimization is not critical. Thus, geometries of the thruster have been attempted to remain simple, and relatively easy to manufacture. Manufacturability of additively manufactured parts is especially important when design small channels, such as the injector orifices or the cooling channels. For the cooling channels, manufacturability was discussed very early in the design process together with the additive manufacturing entity. From these discussions, it was deemed that 0.5 mm was the minimum size the cooling channel could be without risking blocking of the cooling channels, which could result in large pressure drops or even completely blocked flow. For the injector orifices, it was decided to machine these in-house, during the post-processing process.

During the design process, multiple companies were contacted for to manufacture parts of the thruster. In order to manufacture the thruster within the budget, a preference was made to perform manufacturing in-house, with exception for the valves and the thrust chamber. The valves were outsourced due to its complex design and limited reduction in cost when developed in-house. However, during the acquisition process, most of the verification steps (which drive up the price of the valves) were decided to be performed at ESA, in order to limit the cost. For the thrust chamber, Alloyed was selected as the company to additively manufacture the thrust chamber in ABD900AM. For the other parts (manifold and injector), the material does not necessarily have to be ABD900AM. This process has not been finalized yet, but an inquiry within ESA is performed in order to see if these parts can be additively manufactured in-house. Alternatively, Alloyed adheres a minimum order amount of 10 kg of powder. Since the thrust chamber only weighs a few hundred grams, a possibility could be to use the spare powder to manufacture the manifolds. In order to reduce the cost of the additively manufactured parts that are manufactured by Alloyed, post-processing of these parts will be done in-house at ESA ESTEC.

7.2. Thesis Conclusion

To conclude this thesis, a design of a small-scale modular nitrous-oxide-based thruster has been successfully developed. During the design, the emphasis was put on ensuring high performance, functionality with the test bench and structural integrity. In this thesis, this was mainly done by performing different types of simulations like CFD and FEM, as well as simulations using custom-made tools in Python. Furthermore, external advice from manufacturers, the university supervisor and the supervisors from ESA was used to improve the design and its functionality.

The design was initially made using ideal rocket theory, implement in a software called Rocket Propulsion Analysis. After which a thermal optimization was performed using a range of different materials, dimensions and number of cooling channels. From this optimization, it was found that ABD900AM would be the best option as chamber wall material, due to its superior strength at high temperatures. Furthermore, ethane was selected as the fuel, due to its high vapour pressure and self-pressurization properties at room temperature, as well as good performance properties, and handling safety. For the injector and the igniter three types of configurations were selected, based on size, performance, cost/complexity and stability. First of all, two configurations were designed with a glow plug igniter and coaxial swirl injector, due to its good mixing properties and ignition performance. One configuration was made where the igniter and injector were put in the manifold in an off-center configuration, as two separate components. For the second configuration, the igniter was integrated into the injector itself, which was done as it is expected to have a better heat distribution of the igniter and thus better ignition performance. However, due to the large size of the coaxial swirl injector element, the mixing near the wall could create high temperature hot spots.

With the hot spots in mind, a CFD simulation was deemed necessary to give an indication of the heat loads that the chamber wall would undergo. These simulations showed, as expected, the highest temperatures near the injector mixing plane. However, with a maximum temperature of 936 K, this temperature was well below the maximum temperature of ABD900AM, 1100 K, after which the yield strength properties drop significantly. Following the CFD simulations, a FEM analysis was performed in order to verify the structural integrity of the thrust chamber. This analysis showed one defect in the thrust chamber itself, where at the thrust chamber temperature hot spot the safety factor was just below 1.5. Furthermore, the safety factor at the chamber throat was similarly just above 1.5. A recommendation would be to visually inspect both of these locations after the first firings during the verification tests, in order to see if any defects occur. Apart from that, the corners of the fixed flange used in the FEM analysis showed a

safety factor of one. This could be an issue, however likely in reality the temperature of the flange at that location is overestimated, and thus in reality the thermal stress will be less, and the yield strength will be higher. However, this should also be kept in mind during the remaining parts of the verification process.

7.3. Further Recommendations

During the thesis, there was not enough time to complete the entire engine design, manufacturing and verification/qualification process. Thus, after this thesis, some work should still be performed in order to finish this project. In the following section I will shortly go into what work should still be performed, as well as some recommendations based on the results that I have found during this thesis.

Firstly, during this thesis there were some iterations made on the design of the thruster and its components based on feedback given by manufacturing entities. However, the manufacturing process was not yet completed, and especially for the additively manufactured parts it is possible that some tweaks have to be made in order to make the design more printable, i.e. adding supports. Next to that, the drawings in Appendix B have an assigned material. However, based on the available budget at the European Space Agency, as well as the final manufacturer, these materials can still change. The currently assigned materials are merely a recommendation based on structural results and estimation of cost, avoiding over-engineering a part.

Secondly, no physical verification was performed on this thruster during this thesis, and all the results and data are solely based on computational methods and analysis. Thus, based on the verification plan in section 5.3, a complete verification and validation process should be performed in order to verify the functionality, performance and structural integrity of the thruster. This should be done by performing component tests like actuation tests and (component-level) cold flows, as well as integrated tests such as leak tests, cold flows and hot-fires.

With a small-scale thruster like the one designed during this thesis, achieving steady-state firing is a difficult objective to achieve. While the CFD and FEM simulations showed promising results, physical verification is necessary in order to ensure firing this thruster is safe. Especially when the engine is used in pulse mode, fatigue could become an issue at the hot regions of the thruster wall. During the simulations performed in this thesis, the thruster showed two points of attention at the inner chamber wall of the engine. Namely near the injector, and at the throat. With the temperatures found at these points in the simulations, the safety factor with the yield strength would be around 1.5 or just below 1.5. Together with ESA a value of 1.5 was decided as the absolute minimum in order to ensure the structural integrity of this engine. Thus, if any hot-fires are performed in the future, these two locations should be visually inspected at least for the first few longer duration hot-fires (>5 seconds).

Another point of concern which should be verified by physical testing is the pressure drop in the cooling channels. As was analyzed in the CFD simulation, currently the pressure drop in the cooling channels is around 12 bar which seems excessively high. While this could be related to the geometry and setup of the CFD simulation, where the coolant and main fluid domains are kept separate, it could also be a realistic value, due to the very small size of the cooling channels. In order to verify this pressure drop, an integrated cold flow should be performed, where between the valve and the thrust a pressure sensor should be inserted, as well as in the manifold. Furthermore, in this thesis the original design of the thruster using cooling channels with a height of 0.5 mm was used. Upon discussion with the European Space Agency of this large pressure drop, it was decided to manufacture another thrust chamber with a cooling channel height of 1 mm.

Bibliography

Ahn, K., & Lee, B. J. (2019). Experimental Study on the Discharge Coefficient of Bi-Swirl Coaxial Injectors. *Journal of Applied Fluid Mechanics*, *12*(5), 1439–1447. https://doi.org/10.29252/jafm.12.05.29533

Alexander Hodge. (2022, July). Topic 5: Engine Cooling Design - MIT Rocket Team - MIT Wiki Service. https://wikis.mit.edu/confluence/display/RocketTeam/Topic+5%3A+Engine+Cooling+Design

Alloyed. (2025). *Material Overview ABD ®-900AM* (tech. rep.). www.alloyed.com

ANSYS. (2020). Turbulent Boundary Layers Basics of Turbulent Flows-Lesson 6.

Ansys Inc. (2024). Ansys Fluent User's Guide, Release 2024 R1. https://ansyshelp.ansys.com

Arrington, L., Reed, B., & Angel Rivera, J. (1996, July). A performance comparison of two small rocket nozzles. In *32nd joint propulsion conference and exhibit*. https://doi.org/10.2514/6.1996-2582

Autodoc. (2026). 66-0091 MAXGEAR Gloeibougie 11V. https://www.autodoc.nl/maxgear/13935636

Badawy, T., Attar, M., Hutchins, P., Xu, H., Venus, J., & Cracknell, R. (2018). Investigation of injector coking effects on spray characteristic and engine performance in gasoline direct injection engines. *Applied Energy*, *220*, 375–394. https://doi.org/10.1016/j.apenergy.2018.03.133

Bazarov, V., Puri, P., & Yang, V. (2004). Design and Dynamics of Jet and Swirl Injectors. In *Liquid rocket thrust chambers* (pp. 19–103). https://doi.org/10.2514/5.9781600866760.0019.0103

Breisacher, K., & Ajmani, K. (2009, March). *LOX/Methane Main Engine Glow Plug Igniter Tests and Modeling* (tech. rep.). NASA.

Chubb, W. B., & McDonough, G. F. (1994). *Verification Handbook* (tech. rep.). NASA.

Clark, J. D. (2018). *Ignition: An Informal History of Liquid Rocket Propellants* (1st ed.). Rutgers University Press.

Copenhagen Suborbitals. (2019). Swirlers. https://copenhagensuborbitals.com/swirlers/

Dagard. (2026). Dagard: Cleanroom expertise for all your needs. https://www.dagard.com/en/our-solutions/cleanrooms/

Dawn Aerospace. (2025). *B20 THRUSTER* (tech. rep.). Delfgauw.

Delft Aerospace Rocket Engineering. (2024). Stratos V – Delft Aerospace Rocket Engineering. https://dare.tudelft.nl/stratos5/

Devenport, W. J. (2001, March). Converging Diverging Nozzle. https://www.engapplets.vt.edu/fluids/CDnozzle/cdinfo.html

Díaz-Álvarez, J., Tapetado, A., Vázquez, C., & Miguélez, H. (2017). Temperature measurement and numerical prediction in machining inconel 718. *Sensors (Switzerland)*, *17*(7). https://doi.org/10.3390/S17071531

DLR. (2024). LUMEN (Liquid Upper Stage Demonstrator Engine). https://www.dlr.de/en/research-and-transfer/research-infrastructure/large-scale-research-facilities/lumen-en

ECSS. (2018). *Space engineering - Verification (ECSS-E-ST-10-02C Rev.1)* (tech. rep.).

ESA. (2017). ESA - Vacuum chamber in Propulsion Lab. https://www.esa.int/ESA_Multimedia/Images/2017/02/Vacuum_chamber_in_Propulsion_Lab

Fischer, D. (2010, August). Pintle Injector Rocket Engines – NSS. https://nss.org/pintle-injector-rocket-engines/

Gill, G. S., & Nurick, W. H. (1976). *Liquid rocket engine injectors* (tech. rep.).

Gohardani, A. S., Stanojev, J., Demairé, A., Anflo, K., Persson, M., Wingborg, N., & Nilsson, C. (2014, November). Green space propulsion: Opportunities and prospects. https://doi.org/10.1016/j.paerosci.2014.08.001

Gradl, P. R., Protz, C., Cooper, K., Garcia, C., Ellis, D., & Evans, L. (2019). GRCop-42 Development and Hot-fire Testing Using Additive Manufacturing Powder Bed Fusion for Channel Cooled Combustion Chambers. https://doi.org/https://doi.org/10.2514/6.2019-4228

Greer, S. C., & Moldover, M. R. (1981). Thermodynamic anomalies at critical points of fluids. *Annual Review of Physical Chemistry*, *32*(1), 233–265.

Grubelich, M. C., & Lindblom, J. D. (2013). A Comprehensive Performance Analysis of Nitrous Oxide as a Rocket Propellant and Gas Generator Oxidizer. https://www.osti.gov/biblio/1115073

Huang, D. H., & Huzel, D. K. (1992). *Modern Engineering for Design of Liquid Propellant Rocket Engines*. American Institute of Aeronautics; Astronautics, Inc. https://api.semanticscholar.org/CorpusID:109192232

Huzel, D. K. (2000). *Progress in Astronautics and Aeronautics : Modern Engineering for Design of Liquid-Propellant Rocket Engines*. American Institute of Aeronautics; Astronautics.

Janzer, C., Richter, S., Naumann, C., & Methling, T. (2022). “Green propellants” as a hydrazine substitute: experimental investigations of ethane/ethene-nitrous oxide mixtures and validation of detailed reaction mechanism. *CEAS Space Journal*, *14*(1), 151–159. https://doi.org/10.1007/s12567-021-00370-8

Kang, D., Han, S., Ryu, C., & Ko, Y. (2022). Design of pintle injector using Kerosene-LOx as propellant and solving the problem of pintle tip thermal damage in hot firing test. *Acta Astronautica*, *201*, 48–58. https://doi.org/https://doi.org/10.1016/j.actaastro.2022.08.029

Karabeyoglu, A., Dyer, J., Stevens, J., & Cantwell, B. (2008). Modeling of N2O decomposition events. *44th AIAA/ASME/SAE/ASEE Joint Propulsion Conference and Exhibit*. https://doi.org/10.2514/6.2008-4933

Kerstens, F. ; Cervone, A. ; & Gradl, P. (2021). End to end process evaluation for additively manufactured liquid rocket engine thrust chambers. *Acta Astronautica*, *182*, 454–465. https://doi.org/10.1016/j.actaastro.2021.02.034

Kim, H.-G. (2019). A Method of Accelerating the Convergence of Computational Fluid Dynamics for Micro-Siting Wind Mapping. *Computation*, *7*, 22. https://doi.org/10.3390/computation7020022

Kirchberger, C. (2014). Investigation on Heat Transfer in Small Hydrocarbon Rocket Combustion Chambers. https://api.semanticscholar.org/CorpusID:103417932

Kord, K. (2025). Complete Guide to ANSYS Fluent Radiation Models for CFD Simulations | CFDLAND. https://cfdland.com/complete-guide-to-ansys-fluent-radiation-models-for-cfd-simulations/

Kumar, R., Sharma, A., De, A., & Vaidyanathan, A. (2025). Numerical investigation of open- and close-end swirl injector dynamics for LOx-CH4 supercritical combustion. *Aerospace Science and Technology*, *164*, 110360. https://doi.org/https://doi.org/10.1016/j.ast.2025.110360

Lee, W., Ahn, K., & Won, S. (2020). Cold-flow Tests on Three Different Types of Bi-swirl Coaxial Injectors for a Bipropellant Thruster. *Journal of Propulsion and Energy*, *1*(1), 44–56. http://www.dbpia.co.kr/journal/articleDetail?nodeId=NODE10488493

Lepore, M. A., Piller, M., Toneatti, L., & Maligno, A. R. (2025). Assessing structural integrity of small thrusters using computational methods. *Aerospace Science and Technology*, *167*, 110721. https://doi.org/https://doi.org/10.1016/j.ast.2025.110721

Mananssis, K. (2020). *Inbetriebnahme einer regenerativ gekhlten 22 N Brennkammer fr N2O/C2H6 Mono- und Bipropellants sowie Analyse der Verbrennungseffizienz und der Wrmelasten in Heigasversuchen* [Doctoral dissertation]. Universitt Stuttgart. https://elib.dlr.de/137818/

Martin-Luengo, M. (2001). Combining residual gas analysis and DSC to develop catalysts for low energy N2O microthrusters. *ESA bulletin. Bulletin ASE. European Space Agency*, *484*, 201.

Michael Neufeld. (2016). Robert Goddard and the First Liquid-Propellant Rocket | National Air and Space Museum. https://airandspace.si.edu/stories/editorial/robert-goddard-and-first-liquid-propellant-rocket

Millán-Merino, A., Fernández-Tarrazo, E., Sánchez-Sanz, M., & Williams, F. A. (2018). A multipurpose reduced mechanism for ethanol combustion. *Combustion and Flame*, *193*, 112–122. https://doi.org/10.1016/j.combustflame.2018.03.005

NASA. (2024). Able 4B (Pioneer P-3) - NASA Science. https://science.nasa.gov/mission/pioneer-p-3-able-4b/

Navaneethan, M., Sundararajan, T., Srinivasan, K., & Jayachandran, T. (2025). Studies on liquid film cooling coupled to compressible gas in a rocket thrust chamber with ablative throat. *Aerospace Science and Technology*, *164*, 110461. https://doi.org/https://doi.org/10.1016/j.ast.2025.110461

Neeser, J. (2026). Pyrocket.

Ohgaki, K., Umezono, S., & Katayama, T. (1990). Pressure-density-temperature (ppT) relations of CHF3, N2O, and C3H6 in the critical region. *The Journal of Supercritical Fluids*, *3*(2), 78–84.

Palej, P., & Palacz, T. (2018). Preliminary Design Analysis of Regenerative Cooling for N 2 O/Alcohol Small Scale Liquid Rocket Engine. *Transactions on Aerospace Research*, *2018*(3), 87–102. https://doi.org/10.2478/tar-2018-0024

Parker. (2016). Pulse Valves.

Parsonson, A. (2024, March). DLR Test Fires LUMEN Upper Stage Rocket Engine Demonstrator - European Spaceflight. https://europeanspaceflight.com/dlr-test-fires-lumen-upper-stage-rocket-engine-demonstrator/

Pichler. (2026). Zündkerze 1/4-32. https://pichler.de/Zuendkerze-1-4-32

Ponomarenko, A. (2010). RPA: Tool for Liquid Propellant Rocket Engine Analysis C++ Implementation. https://api.semanticscholar.org/CorpusID:219556247

Rao, G. V. R. (1958). Exhaust Nozzle Contour for Optimum Thrust. *Jet Propulsion*, *28*(6), 377–382. https://doi.org/10.2514/8.7324

Russian Space Web. (2012). Design of the first artificial satellite of the Earth. https://www.russianspaceweb.com/sputnik_design.html

Showa Denko. (1998). Nitrous Oxide High-Purity Nitrous Oxide N2O.

Sigma-Aldrich. (2025). Ethane. https://www.sigmaaldrich.com/NL/en/product/aldrich/539775

SmallSat Catalog. (2026). B20 Thruster Green Chemical Propulsion from Dawn Aerospace. https://catalog.orbitaltransports.com/b20-thruster-green-propulsion/

Soller, S., Behr, R., Beyer, S., Laithier, F., Lehmann, M., Preuss, A., & Salapete, R. (2017). Design and Testing of Liquid Propellant Injectors for Additive Manufacturing.

SpaceX. (2025). SpaceX - Falcon 9. https://www.spacex.com/vehicles/falcon-9

SPECIAL METALS. (2007). *INCONEL ® alloy 718* (tech. rep.).

Special Metals Corporation. (2013). *INCONEL 625* (tech. rep.). Special Metals Corporation. https://www.specialmetals.com/documents/technical-bulletins/inconel/inconel-alloy-625.pdf

Sutton, G. P., & Biblarz, O. (2016). *Rocket Propulsion Elements* (9th). John Wiley & Sons.

The Engineering Toolbox. (2024). Propane - Thermophysical properties. https://www.engineeringtoolbox.com/propane-d_1423.html

The Engineering Toolbox. (2025). Methane (CH): Thermophysical Properties and Phase Diagram. https://www.engineeringtoolbox.com/methane-d_1420.html

The Engineering Toolbox. (2025). Ethylene - Thermophysical Properties. https://www.engineeringtoolbox.com/ethylene-ethene-C2H4-properties-d_2104.html

Tucker, P. K., Shyy, W., Vaidyanathan, R., & Turner, J. (2000). *An Optimization-Based Approach to Injector Element Design* (tech. rep.). NASA.

Tyll, J. S., & Herdy, R. (2001, 16). *The Nitrous Oxide - Propane Rocket Engine* (tech. rep.). DARPA.

van der Laan, F. H., & Timnat, Y. M. (1985, April). *Chemical Rocket Propulsion* (tech. rep.). Delft University of Technology, Department of Aerospace Engineering. Delft, Netherlands.

Werling, L., & Hörger, T. (2021). Experimental analysis of the heat fluxes during combustion of a N2O/C2H4 premixed green propellant in a research rocket combustor. *Acta Astronautica*, *189*, 437–451. https://doi.org/https://doi.org/10.1016/j.actaastro.2021.07.011

Xie, Y., Zhang, J., Sun, M.-B., Wu, J., Li, P., An, B., Liang, C., Wang, T., Cheng, P., Chen, J., Wang, J., & Li, M. (2024). Review on spray characteristics of liquid–liquid injectors in liquid rocket engines. *Physics of Fluids*, *36*. https://doi.org/10.1063/5.0223894

Yamamoto, Y., & Tachibana, T. (2024). Decomposition promotion of nitrous oxide for its use as an energy carrier. *Fuel*, *364*, 131055. https://doi.org/https://doi.org/10.1016/j.fuel.2024.131055

Zakirov, V., Sweeting, M., Goeman, V., & Lawrence, T. (2000). Surrey Research on Nitrous Oxide Catalytic Decomposition for Space Applications.

Zakirov, V., Sweeting, M., Lawrence, T., & Sellers, J. (2001). Nitrous oxide as a rocket propellant. *Acta Astronautica*, *48*(5-12), 353–362. https://doi.org/10.1016/S0094-5765(01)00047-9

Zandbergen, B. T. C. (2022, September). *Thermal Rocket Propulsion Reader* (tech. rep.). TU Delft.

Zhao, X., Li, Y., Chen, X., Yin, Y., & Huang, G. (2025). Radiation cooling system: Limitations, solutions, and future challenges. *Renewable and Sustainable Energy Reviews*, *212*, 115428. https://doi.org/https://doi.org/10.1016/j.rser.2025.115428

Zhu, M., Han, H., Gao, R., & Xie, B. (2023). Numerical investigation of pyrolysis coking characteristics of supercritical hydrocarbon fuels in sinusoidal cooling channels. *Fuel*, *344*, 127881. https://doi.org/https://doi.org/10.1016/j.fuel.2023.127881

A
Datasheets

In this appendix the datasheet of ABD900AM, the thrust chamber material, will be given. Furthermore, the specification document that was made during this thesis for the valve manufacturing entity, is also given.

A.1. ABD900AM Datasheet

Alloyed

ABD®-900AM

Nickel-based superalloy for additive manufacturing

Material Overview

ABD®-900AM is an age-hardenable nickel-based superalloy designed specifically for use as feedstock in powder bed fusion.

It is optimised for environmental resistance and high-temperature tensile strength, with a working temperature range up to 900°C (1652°F) in its age-hardened state. Compared to alloy 718, ABD®-900AM not only offers a higher operating temperature but also significant long-term stability.

The alloy has excellent creep strength – similar to alloy 939 and alloy 738 – while having superior resistance to cracking during manufacture and heat treatment, enabling complex part design.

ABD®-900AM is suitable for complex components within the Aerospace, Power, Automotive and Space industries (e.g. combustion chamber, left)

Height: 291 mm
Width: 147 mm

Designed to be free of solidification, liquidation, and strain-age cracks, ABD®-900AM showcases exceptional printability for a 40% γ'-phase strengthened alloy.

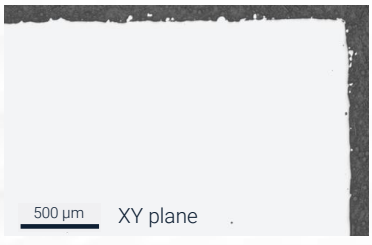

ABD®-900AM shows high as-printed part density of >99.9% and no cracking when printed with standard alloy 718 parameters.

Key Material Properties

Mechanical [1,2] (900°C)	Yield strength/ MPa	574 Z, 568 XY
	Ultimate tensile strength/ MPa	582 Z, 593 XY
	Elongation at failure/ %	13 Z, 7 XY
	Area reduction at failure/ %	12Z,7XY
Thermophysical [3] (25-1200°C)	Thermal Conductivity/ $W(m°C)^{-1}$	11.0 – 30.1
	CTE (Linear)/ $x10^{-6}$ $°C^{-1}$	11.4 – 19.2
Physical [4]	Density/ g cm^{-3}	8.395
	Melting range[2]/ °C	1305 – 1380

All measurements are for the alloy printed with a layer thickness of 30 µm.
[1]strain rate of 10^{-3} s^{-1}, [2]after recrystallisation anneal and full heat treatment,
[3]after full heat treatment, [4]as-printed

Powder Properties

ABD®-900AM powder is available for laser beam melting in a nominal 15-53 µm size range with the following properties:.

Test	Value	Standard
Carney flow/ s $50g^{-1}$	2 - 3	ASTM B964
Hall flow/ s $50g^{-1}$	12 - 14	ASTM B213
Apparent density/ g cm^{-3}	4.3 - 4.5	ASTM B212
Tapped density/ g cm^{-3}	5.1 - 5.4	ASTM B527

Also available in:

- 45-106 µm (EBM/DED)
- Custom size distributions available on request

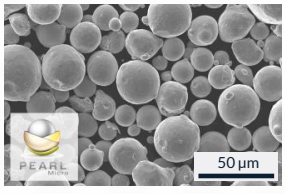

ABD®-900AM is available in batch sizes suitable for R&T and full production from our powder partner Aubert & Duval

Typical powder morphology

made with ABD®

+44 (0)1865 954 250
contact@alloyed.com
www.alloyed.com

Alloyed

ABD®-900AM

Nickel-based superalloy for additive manufacturing

Yield Strength & Ultimate Tensile Strength

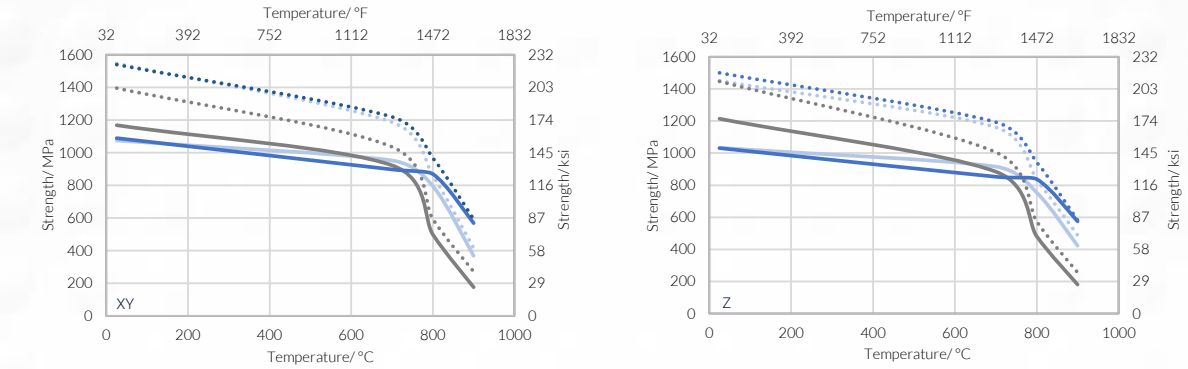

ABD®-900AM – YS – full heat treatment
ABD®-900AM – YS – recrystallisation anneal and full heat treatment
Alloy 718 – YS – standard full heat treatment
ABD®-900AM – UTS – full heat treatment
ABD®-900AM – UTS – recrystallisation anneal and full heat treatment
Alloy 718 – UTS – standard full heat treatment

Tensile properties of additively manufactured ABD®-900AM and Alloy 718, evaluated at a strain rate of 10^{-3} s^{-1}, all other test conditions in accordance to ASTM E8/E8M-16a/E21. No HIP applied. Yield Strength (YS) shown is $R_{p0.2\%}$ stress, Ultimate Tensile Strength (UTS) is stress at maximum force.

Tensile Ductility & Reduction Of Area

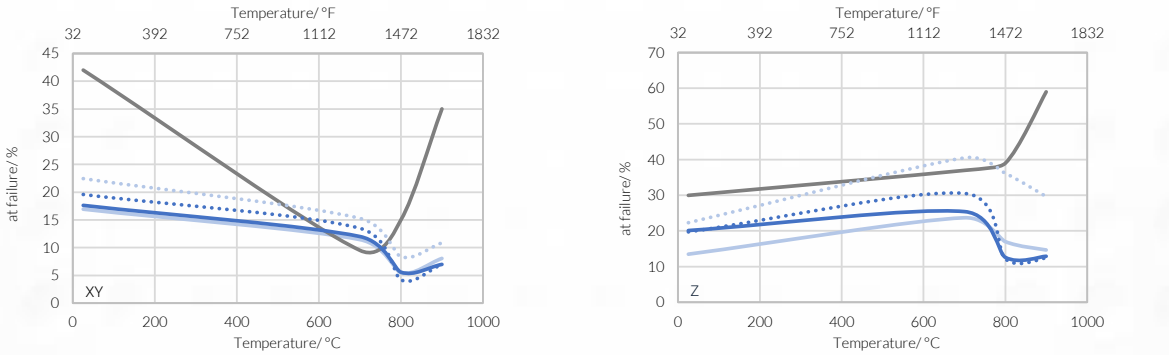

ABD®-900AM – Elongation – full heat treatment
ABD®-900AM – Elongation – recrystallisation anneal & full heat treatment
Alloy 718 – Elongation – standard full heat treatment
ABD®-900AM – Area Reduction – full heat treatment
ABD®-900AM – Area Reduction – recrystallisation anneal and full heat treatment

Tensile properties of additively manufactured ABD®-900AM and Alloy 718, evaluated at a strain rate of 10^{-3} s^{-1}, all other test conditions in accordance to ASTM E8/E8M-16a/E21. No HIP applied. Elongation and Area Reduction were measured after failure as per the standards.

made with ABD®

+44 (0)1865 954 250
contact@alloyed.com
www.alloyed.com

Alloyed

ABD®-900AM

Nickel-based superalloy for additive manufacturing

Long Term Stability

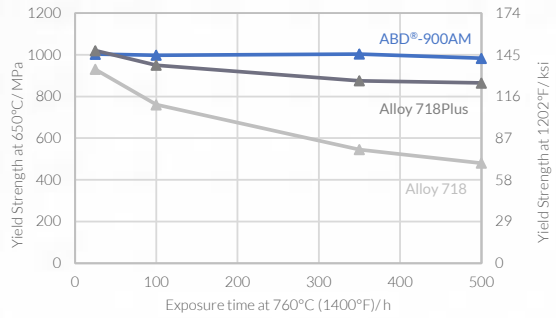

Tensile properties of additively manufactured ABD®-900AM after full heat treatment cycle followed by long term heat exposure. Yield strength evaluated at 650°C with a strain rate of 10^{-4} s^{-1}. Data for cast Alloy 718 and Alloy 718Plus taken from *"Advanced Materials and Processes, December 2006"*

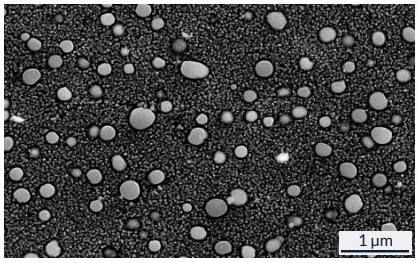

SEM image of fully heat-treated ABD®-900AM after electro-chemical etching in 10% phosphoric acid showing the bi-modal γ'-phase distribution: 50 and 200 nm

Fatigue Properties

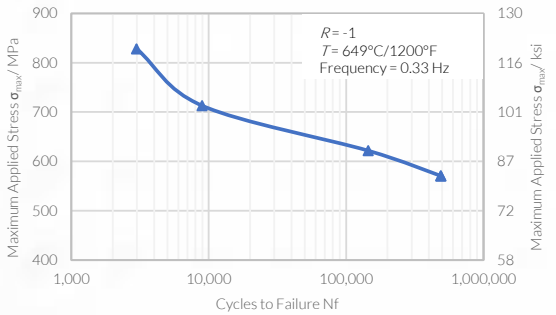

Fatigue properties of additively manufactured ABD®-900AM after full heat treatment cycle. Tested in accordance to ASTM E606.

Stress Rupture Properties

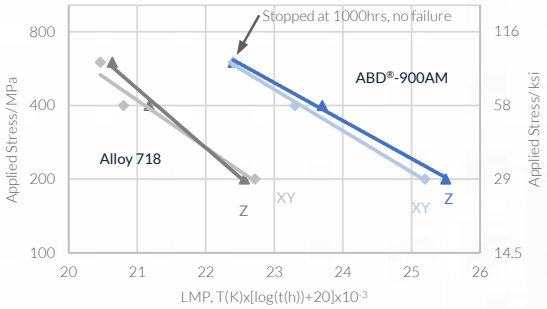

Stress rupture properties of additively manufactured ABD®-900AM after recrystallisation anneal and full heat treatment cycle. Tested in accordance to ASTM E139. Larson-Miller Parameter evaluated with Temperature (T) in Kelvin and Time (t) in hours. Alloy 718 is additively manufactured and fully heat treated.

+44 (0)1865 954 250
contact@alloyed.com
www.alloyed.com

Alloyed

Thermophysical Properties

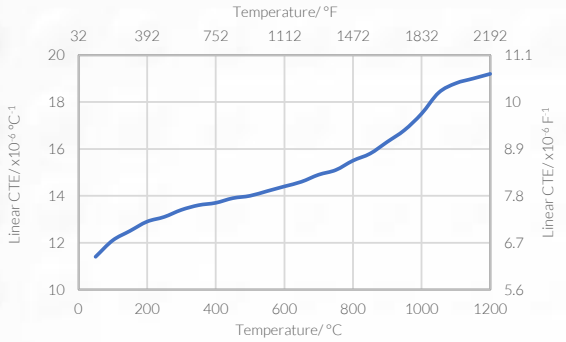

Linear coefficient of thermal expansion measured according to ASTM E228. Average of heating and cooling curves. [1]

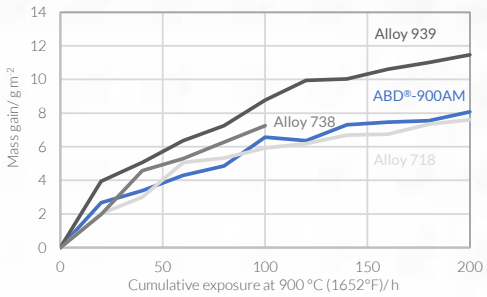

Mass gain of ABD®-900AM and other alloys during the course of cyclic oxidation in laboratory air over 200 hrs. [1]

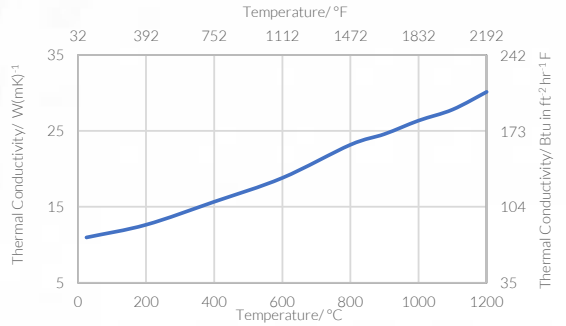

Thermal conductivity (λ) of ABD®-900AM is calculated using ASTM standards from measured values of density (ρ), specific heat capacity (C_p), and thermal diffusivity (a): $\lambda = \rho\ C_p\ a$. [1]

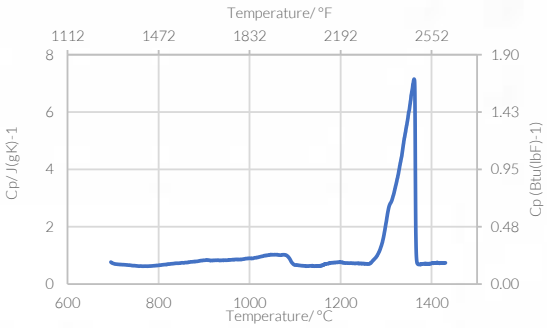

Specific heat (C_p) of ABD®-900AM, measured according to ASTM E1269. [2]

[1]ABD®-900AM after full heat treatment, [2]ABD®-900AM in an as-printed condition

Microstructure & Heat Treatment

Full heat treatment: 1060°C / 2hrs + 850°C/4 hrs + 760°C / 16 hrs

Recrystallisation anneal: 1240°C/ 2hrs, followed by full heat treatment

HIP parameter: 1160°C / 100 MPa / 3hrs

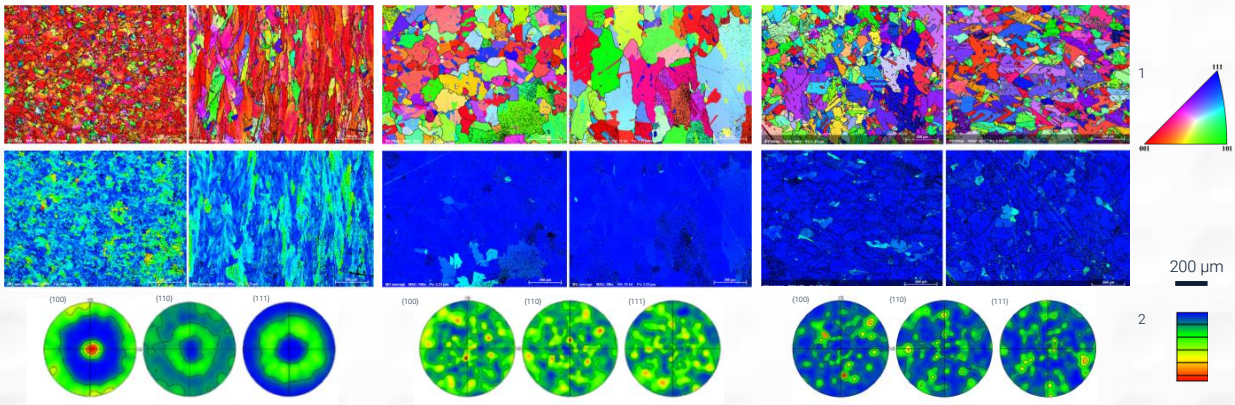

Typical EBSD maps and grain structures of ABD®-900AM after the corresponding heat treatments.

[1]Crystallographic misalignment scale, [2]Scale for pole figures, blue-red = increasing grain density in given direction

made with ABD®

+44 (0)1865 954 250
contact@alloyed.com
www.alloyed.com

A.2. Valve Specification Document

20N BIPROPELLANT THRUSTER VALVE REQUIREMENTS

NOTE
/T refers to a requirement that shall be verified by test
/A refers to a requirement that may be verified by analysis in the frame of this activity
/D refers to a requirement that shall be verified by design
/I refers to a requirement that shall be verified by inspection

1 FUNCTIONAL REQUIREMENTS

VLV10-001/T
The Maximum Expected Operating Pressure (MEOP1) is 60 bar. This is the maximum sustained pressure at which the system actually operates.

For the MEOP pressure cycles test, the MEOP pressure shall be sustained for a min. period of time of 2 min.

VLV10-003/T
The minimum proof factor shall be 1.5 at worst temperature condition. Therefore proof pressure is 1.5xMEOP1.

For the proof pressure test, the proof pressure shall be sustained for a min. period of time of 5 min.

VLV10-005/T
The minimum burst factor shall be 4.0 at worst temperature condition. Therefore burst pressure is 4.0xMEOP1.

For the burst pressure test, the burst pressure shall be sustained for a min. period of time of 1 min.

VLV10-007/A
The valve shall be compatible with the following operating and test media

- Gaseous Helium i.a.w. AD1
- Gaseous Nitrogen i.a.w. AD2
- Gaseous Argon i.a.w. AD3
- Isopropyl alcohol i.a.w. AD4
- Deionised/demineralised water i.a.w. AD5
- HFE-7100 i.a.w. AD6
- Nitrous Oxide AD7
- Various hydrocarbons (propylene, ethylene, ethane, propane, butane)

Note: The requirement could be assessed based on available historical data. No verification by test is strictly required if sufficient justification is provided.

VLV10-009/T
The valve shall be compatible with the following temperature limits:

- Non-operating temperatures shall be between -30°C and +50°C
- Operating temperatures shall be between 0°C and +35°C
- Acceptance temperatures shall be between -5°C and +40°C
- Qualification temperatures shall be between -10°C and +45°C

For transient periods (i.e. up to 30min) in non-operating mode the valve shall not degradate under temperature limits up to 90C and presence of propellant.

Note: Any different conditions from the specified above shall be agreed with the Agency.

VLV10-013/T
The valve shall accept a maximum mass flow rate of 12 g/s of nitrous oxide. Note: The mass flow rate refers to N2O in gaseous state at 20°C and 45 bar.

VLV10-015/T
The pressure drop of the valve at a mass flow rate of 12 g/s of nitrous oxide shall not exceed 0.5 bar .
Note: The mass flow rate refers to N2O in gaseous state at 20°C and 45 bar.

VLV10-017/T
The internal leak rate of each individual seat shall not exceed 1 x 10^{-4} scc/s in any pressure range between [3.5, MEOP1] bar pressurised with Helium as per AD1 and qualification temperature range as specified in VLV10-009.

VLV10-019/T
The external leak rate (before and after operation) shall not exceed 1 x 10^{-6} scc/s with the propellant equipment pressurised at MEOP1 with Helium.

VLV10-021/T (Response Time)
The valve shall either open or close within 15ms within the voltage range specified in VLV1-051, the valve pressurised in the range between [3.5, MEOP1] bar and any temperature in the operative qualification range specified in VLV10-009.
The variability over a pulse train of 50 pulses at the same operating conditions shall be less than +/-1.5ms (2-σ) . The requirement applies for opening and/or closing times.
Note: The response time is measured from the actuation of the valve until the valve is fully opened or closed.

VLV10-023/T (Slam Start test)
The unit inlet shall be pressurised slowly with a propellant simulant from ambient to a min. of 75 bar in not greater than 100 ms shall be applied. This test shall be repeated 20 times. The test shall not result in any degradation of the unit or its performance.

VLV10-025/T (Pressure cycles)
The unit will be subjected to a maximum pressure duty cycles, including re-test if any, given below:

- 10 pressure cycles at proof
- 15 pressure cycles at MEOP

Note: The above number of cycles shall be demonstrated with a safety factor of four. Duration for each pressure cycle as per VLV10-001 & VLV10- 003 apply.

VLV10-027/T (Wet cycles)
The unit shall not be degraded after exposure to a minimum of 100000 wet cycles (fluid flows) .

As a goal, the number of cycles could be extended to 1000000 wet cycles. The extension of the number of cycles may be pursued after the achievement of the

required number of cycles and a successful full functional performance verification.

VLV10-029/T (Dry cycles 1)
The unit shall not be degraded after exposure to a minimum of 100 dry cycles of length not exceeding 10min at its maximum supply voltage as defined in requirement VLV10-051.

Note: a dry cycle is defined as an activation on-ground without fluid flow

VLV10-031/T (Dry cycles 2)
The unit shall not be degraded after exposure to a minimum of 2000 dry cycles of length not exceeding 1 sec at its maximum supply voltage as defined in requirement VLV10-051.
Note: a dry cycle is defined as an activation on-ground without fluid flow

2 MECHANICAL INTERFACE REQUIREMENTS

VLV10-041/D
For testing purposes, the mechanical interface shall be standard threaded ¼" Swagelok straight fittings .

3 ELECTRICAL REQUIREMENTS

VLV10-051/T (Supply voltage)
The equipment shall meet the requirements of this specification when each valve is supplied with voltage of 24 Vdc .

VLV10-053/T (Overvoltage)
The equipment shall be able to withstand an overvoltage no greater than 30Vdc continuously [i.e. min. 5 min] and no greater than 55Vdc for no longer than 5ms without any degradation in performance .

VLV10-055/T (Reverse polarity)
The equipment shall not be damaged after power connection with reverse polarity.

VLV10-057/T (Power)
The power consumption of the two valves (separately) shall be defined by the contractor.

VLV10-059/T (Pull-In Voltage)
The valve shall open at a voltage from 24.0 Vdc with the inlet pressurised in the range between [3.5, MEOP1] bar and any temperature range in the operative qualification range specified in VLV10-009.

VLV10-061/T (Drop out Voltage)
The valve shall close at a voltage not less than 3.0 Vdc with the inlet pressurised in the range between [3.5, MEOP1] bar and any temperature range in the operative qualification range specified in VLV10-009.

VLV10-063/T (Insulation Resistance)

The insulation resistance between the body and the coil shall be larger than 100MΩ with an applied voltage of 500Vdc for a minimum of 1 minute starting from the moment the reading is stable.
The leakage current shall not exceed 0.5mA when measured at 21+/-5 C.

VLV10-065/T (Coil Resistance)

The coil resistance must be defined by the contractor. The variation unit-to-unit of the coil resistance must not be larger than 10%.

VLV10-067/T (Coil Inductance)
The coil inductance must be defined by the contractor. The variation unit-to-unit of the coil inductance must not be larger than 10%.

VLV10-069/T (Electrical bonding)
The equipment mounting surface area shall be unpainted and any protective coating shall produce a conductive finish suitable for electrical bonding.
The dc resistance, measured in any direction, between any metallic parts of the equipment housing shall be less than 20milliohms.

B
Drawings

In the following pages, the drawings will be shown for each custom-made component designed during this thesis. Dimensions are only included for the coaxial swirl injector elements, for the other components the dimensions were not indicated in the drawings. However, the characteristic dimensions of the thrust chamber in section 6.1.

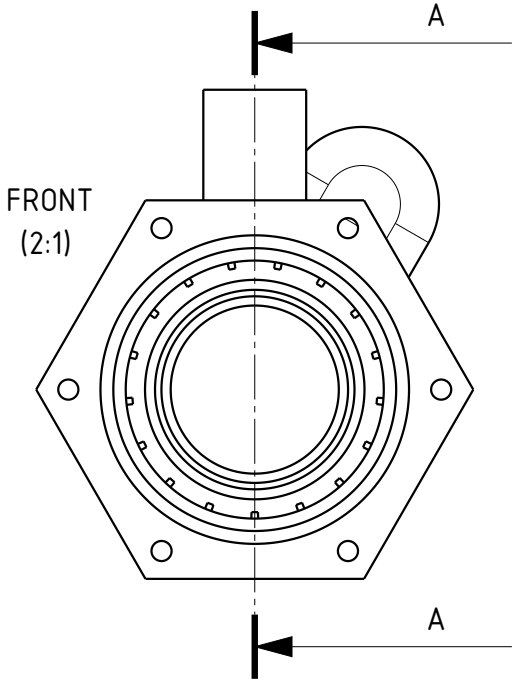

FRONT
(2:1)

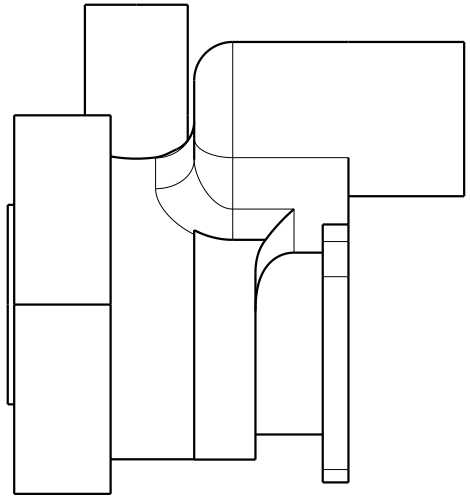

RIGHT
(2:1)

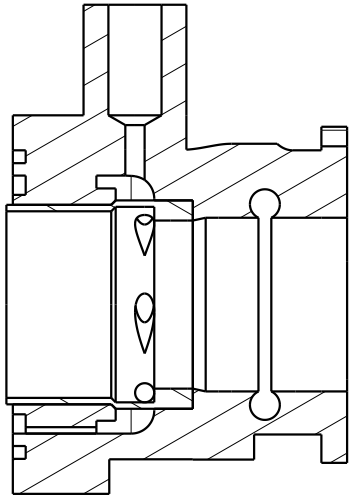

A-A
(2:1)

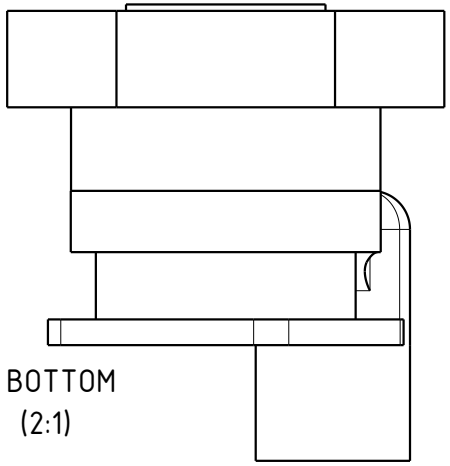

BOTTOM
(2:1)

DESIGNED BY: Timo Kramer	Central Coaxial Swirl Injector Manifold
DATE: 17/02/2026	
SIZE A4	DASSAULT SYSTEMES
SCALE 2:1	MATERIAL IN625 / SHEET 1/1

I	_
H	_
G	_
F	_
E	_
D	_
C	_
B	_
A	_

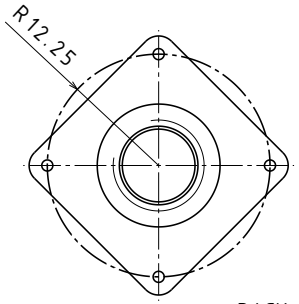

BACK
(2:1)

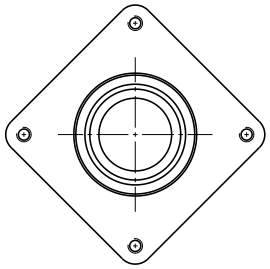

FRONT
(2:1)

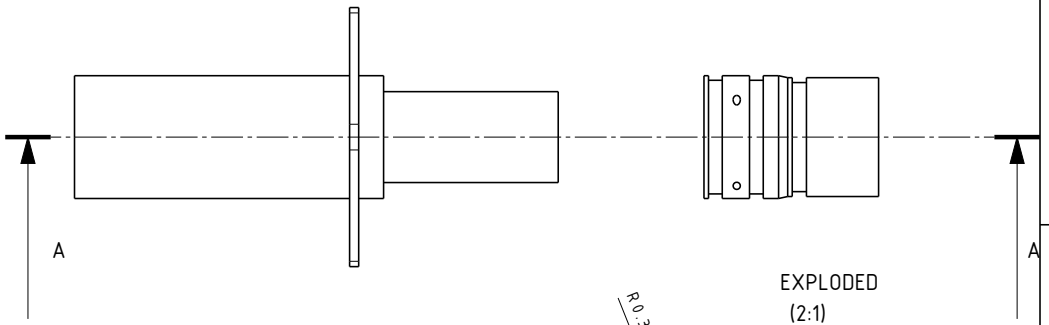

EXPLODED
(2:1)

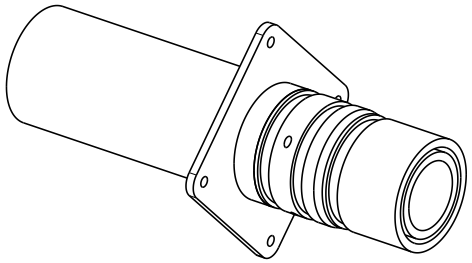

ISOMETRIC
(2:1)

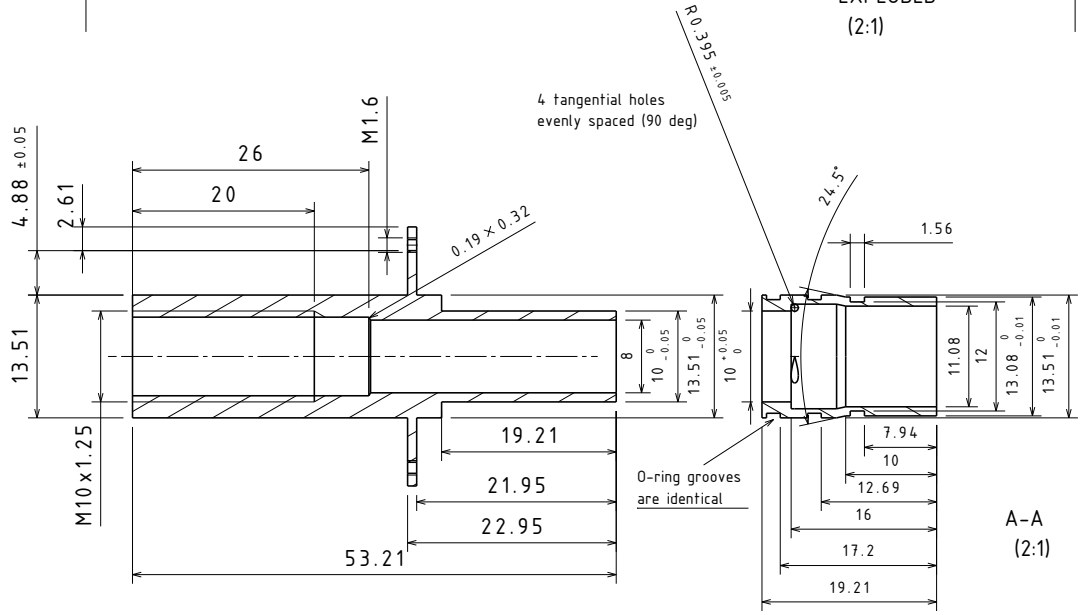

A-A
(2:1)

DESIGNED BY: Timo Kramer DATE: 27/01/2026	Coaxial Swirl Injector		
CHECKED BY: XXX DATE: XXX			
SIZE A3	European Space Agency		
SCALE 2:1	Material: IN625	TOLERANCES (UNLESS STATED OTHERWISE): ISO-2768-m	SHEET 1/1

I	–
H	–
G	–
F	–
E	–
D	–
C	–
B	–
A	–

Four tangential holes equally distributed with a diameter of 0.67 mm

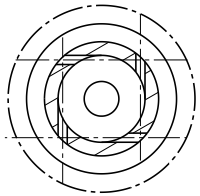

C-C
(3:1)

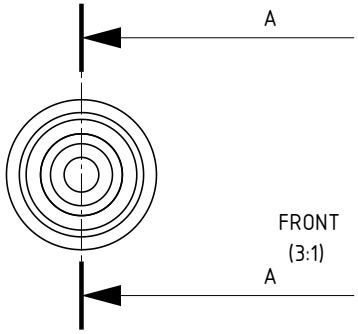

FRONT
(3:1)

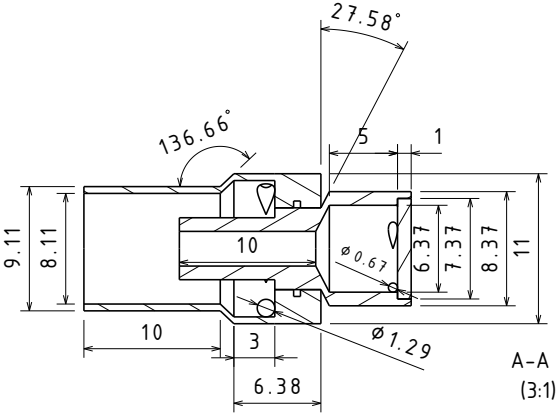

A-A
(3:1)

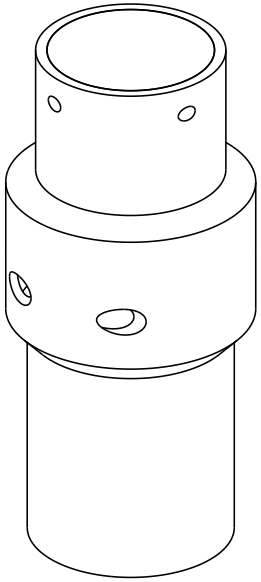

ISOMETRIC
(5:1)

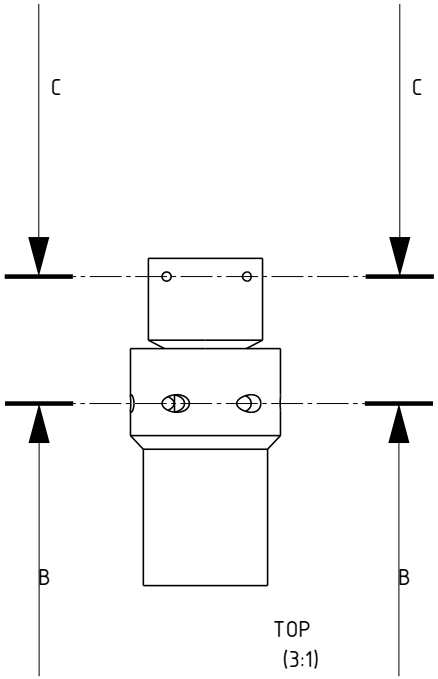

TOP
(3:1)

Five 1.29 mm diameter tangential holes, equally spaced over 300 degrees

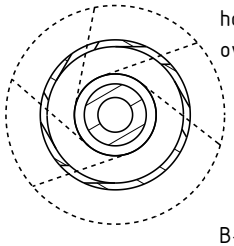

B-B
(3:1)

DESIGNED BY: Timo Kramer	Off-Center Coaxial Swirl Injector
DATE: 20/02/2026	
SIZE A3	DASSAULT SYSTEMES
SCALE 3:1	MATERIAL IN625
	SHEET 1/1

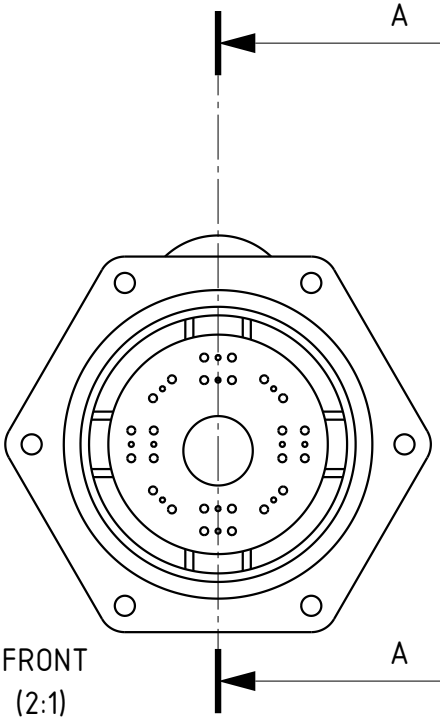

FRONT
(2:1)

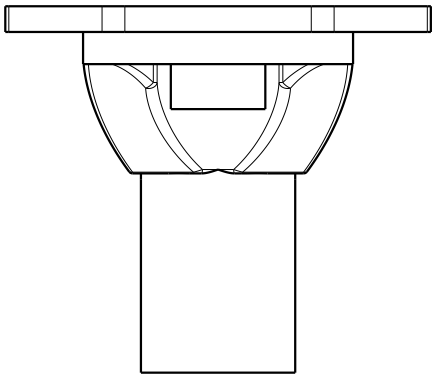

BOTTOM
(2:1)

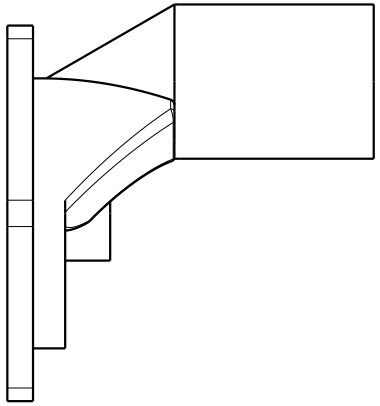

RIGHT
(2:1)

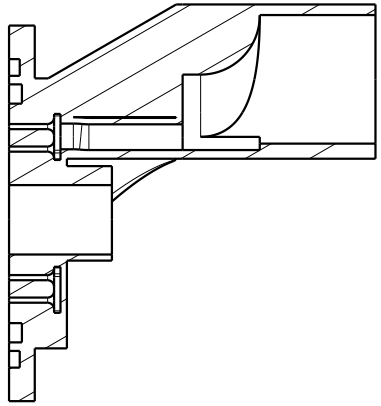

A-A
(2:1)

DESIGNED BY: Timo Kramer
DATE: 17/02/2026

Impinging Injector Manifold

SIZE A4

DASSAULT SYSTEMES

SCALE 2:1

MATERIAL IN625

SHEET 1/1

I	_
H	_
G	_
F	_
E	_
D	_
C	_
B	_
A	_

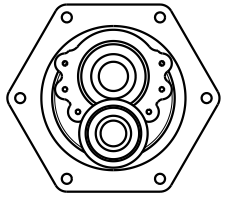

BACK
(1:1)

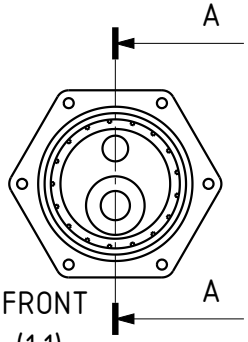

FRONT
(1:1)

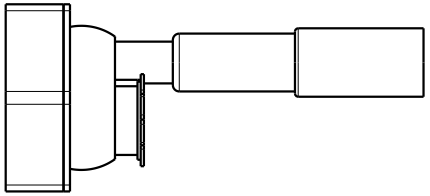

RIGHT
(1:1)

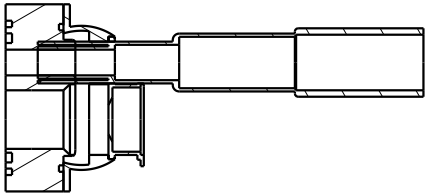

A-A
(1:1)

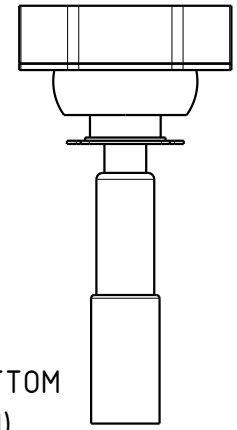

BOTTOM
(1:1)

DESIGNED BY: Timo Kramer
DATE: 17/02/2026

Off-Center Coaxial Swirl Injector Manifold

SIZE A4

DASSAULT SYSTEMES

SCALE 1:1

DRAWING NUMBER XXX

SHEET 1/1

I	_
H	_
G	_
F	_
E	_
D	_
C	_
B	_
A	_

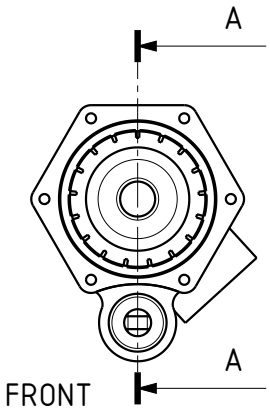

FRONT
(1:1)

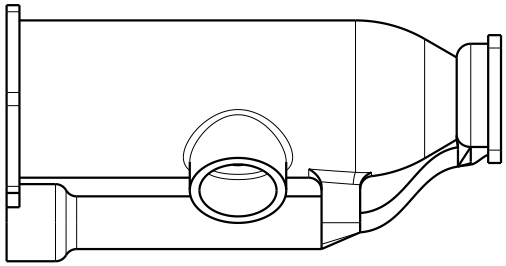

RIGHT
(1:1)

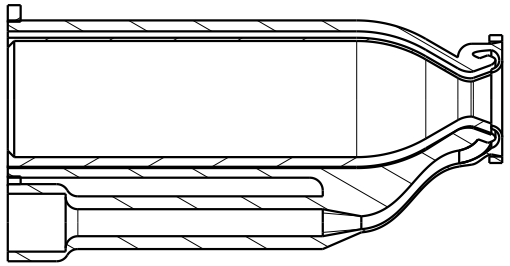

A-A
(1:1)

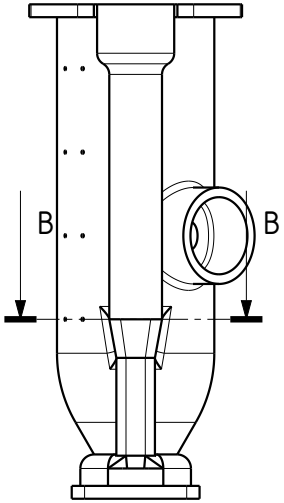

BOTTOM
(1:1)

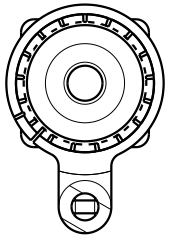

B-B
(1:1)

DESIGNED BY: Timo Kramer DATE: 17/02/2026	Thrust Chamber		I _ H _ G _ F _ E _ D _ C _ B _ A _
SIZE A4	DASSAULT SYSTEMES		
SCALE 1:1	MATERIAL ABD900AM	SHEET 1/1	

C
Meshes

In this chapter, the meshes of both the CFD simulation and the FEM simulation will be shown. Both meshes are created from tetrahedral elements in Ansys Meshing.

C.1. CFD Mesh

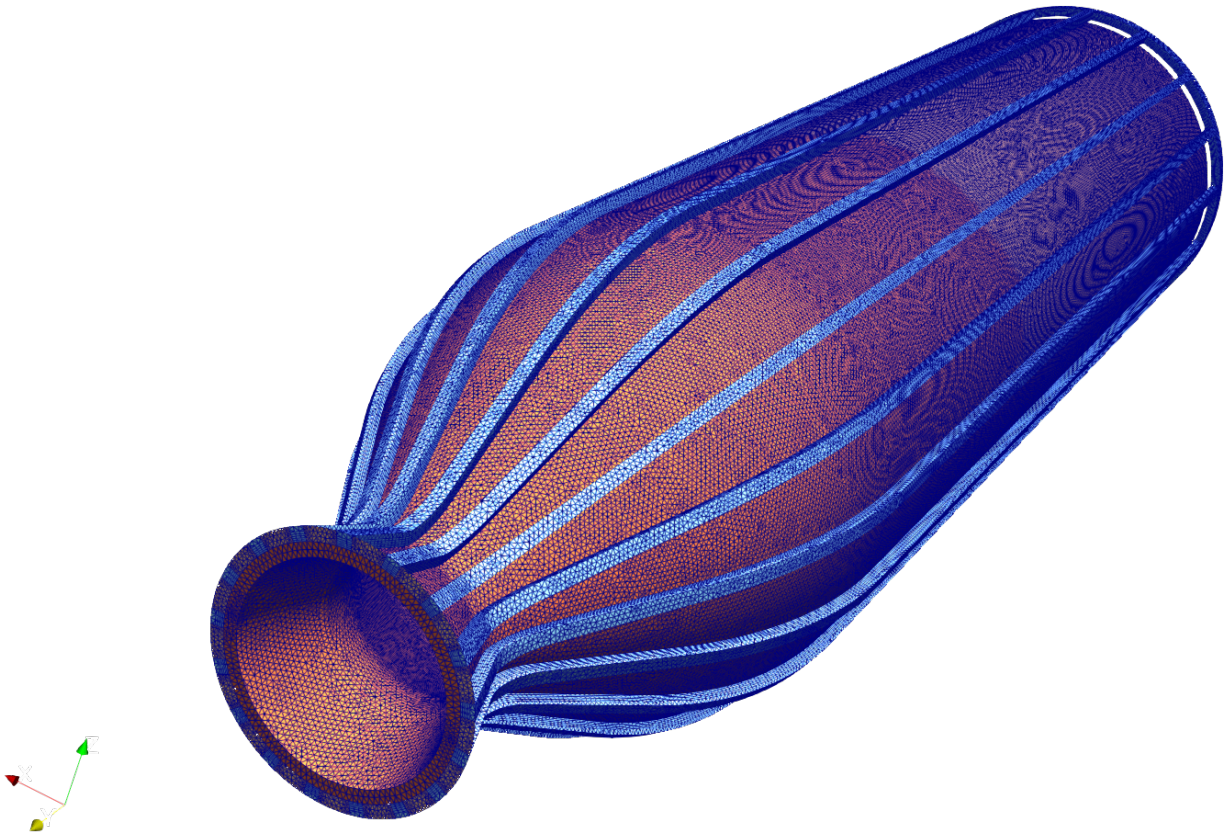

Figure C.1: CFD mesh inner wall and cooling channels isometric view

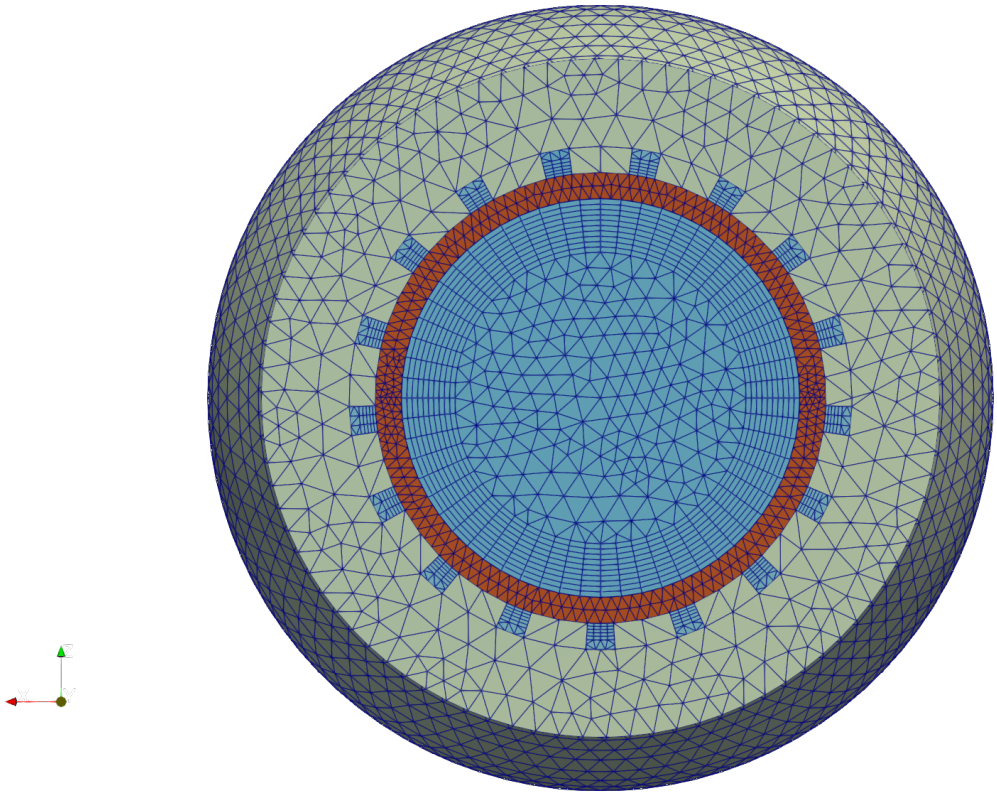

Figure C.2: CFD mesh front view

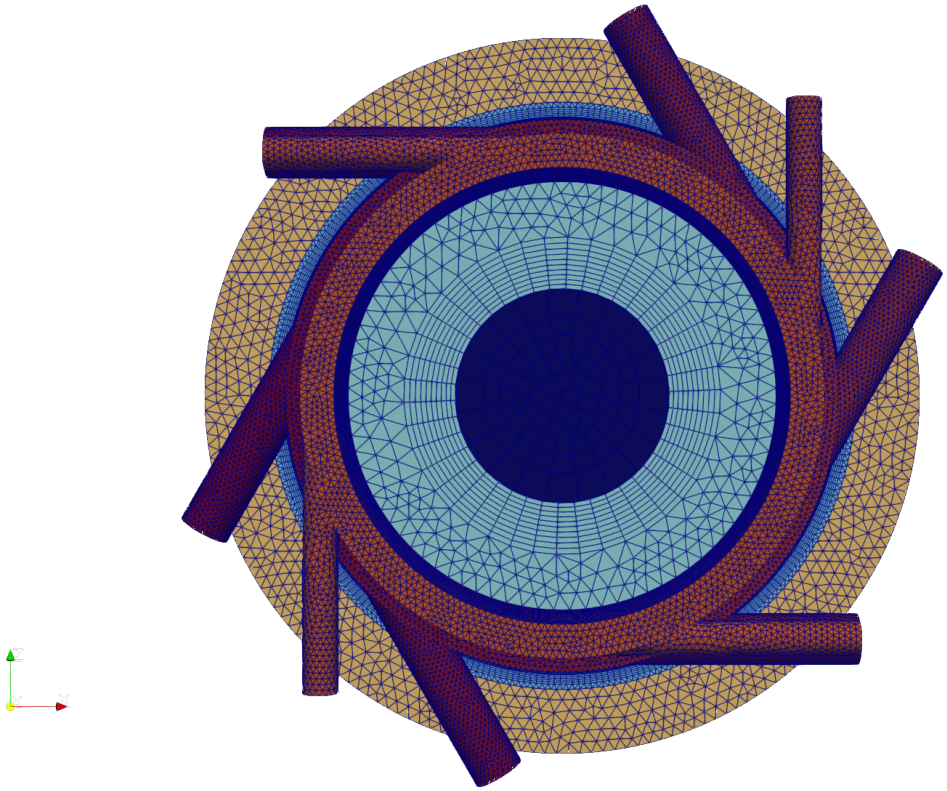

Figure C.3: CFD mesh back view

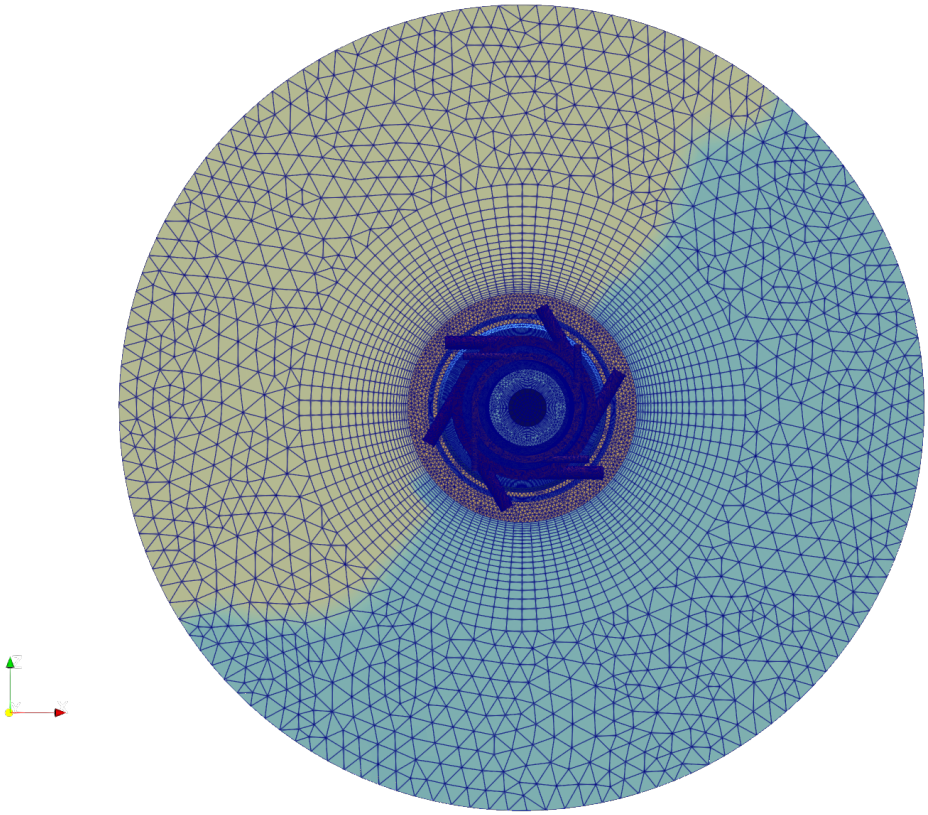

Figure C.4: CFD mesh back view of full domain

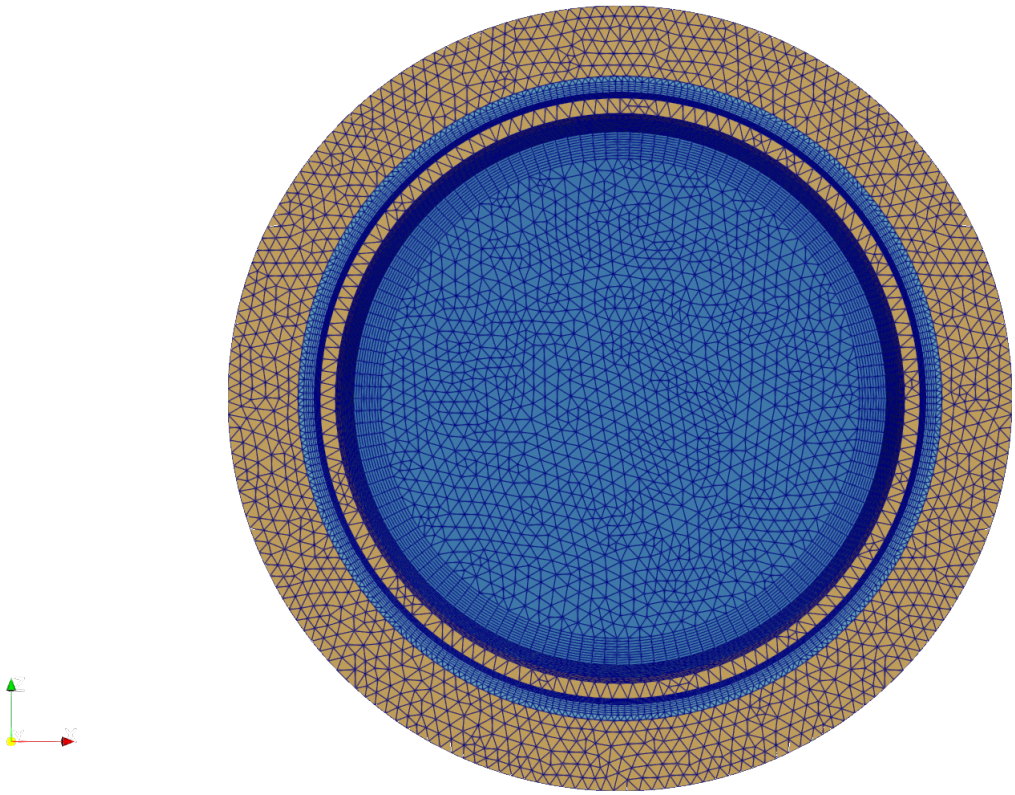

Figure C.5: CFD mesh back view of main chamber

C.2. FEM Mesh

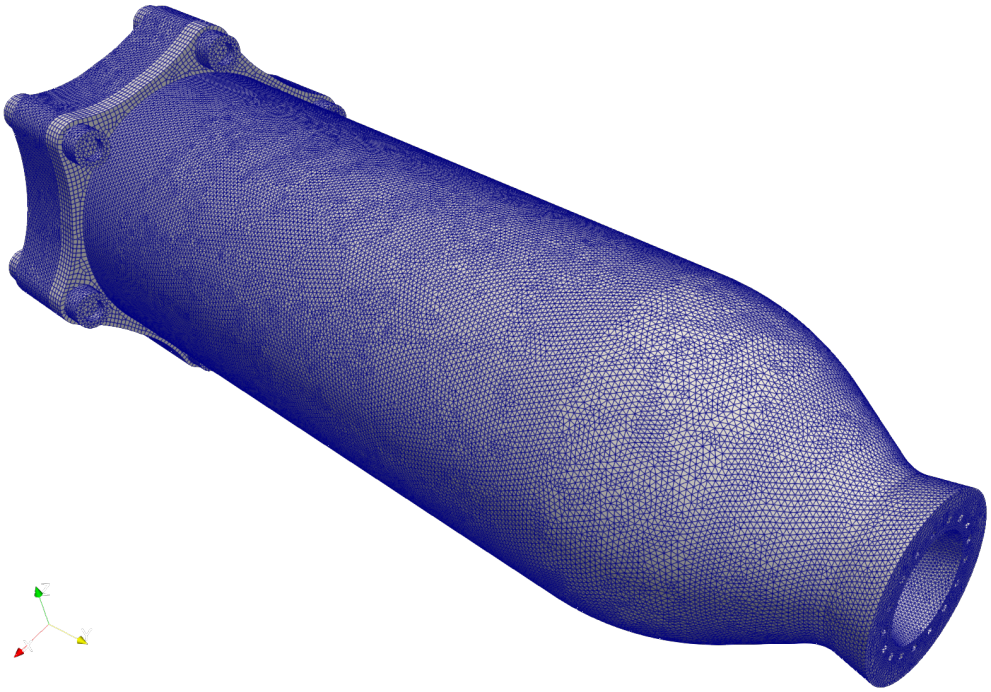

Figure C.6: FEM mesh isometric view

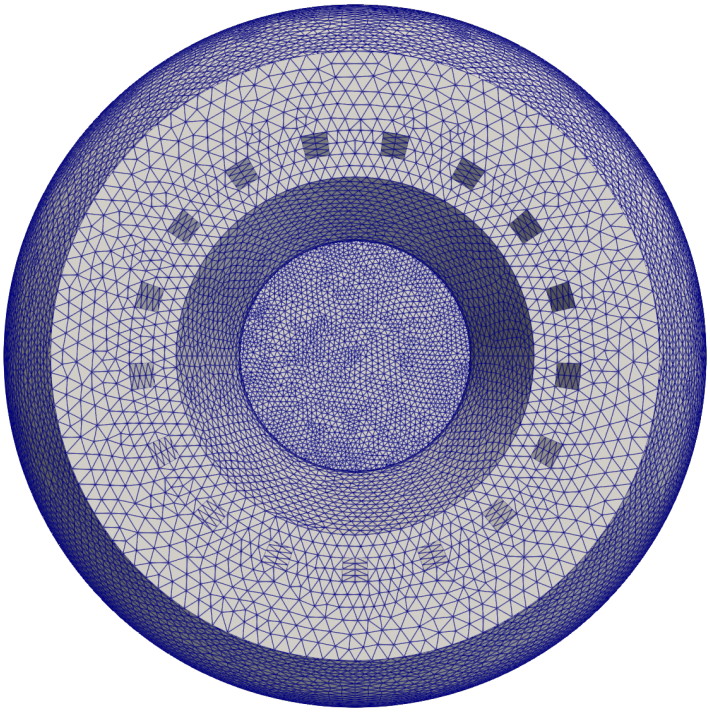

Figure C.7: FEM mesh front view

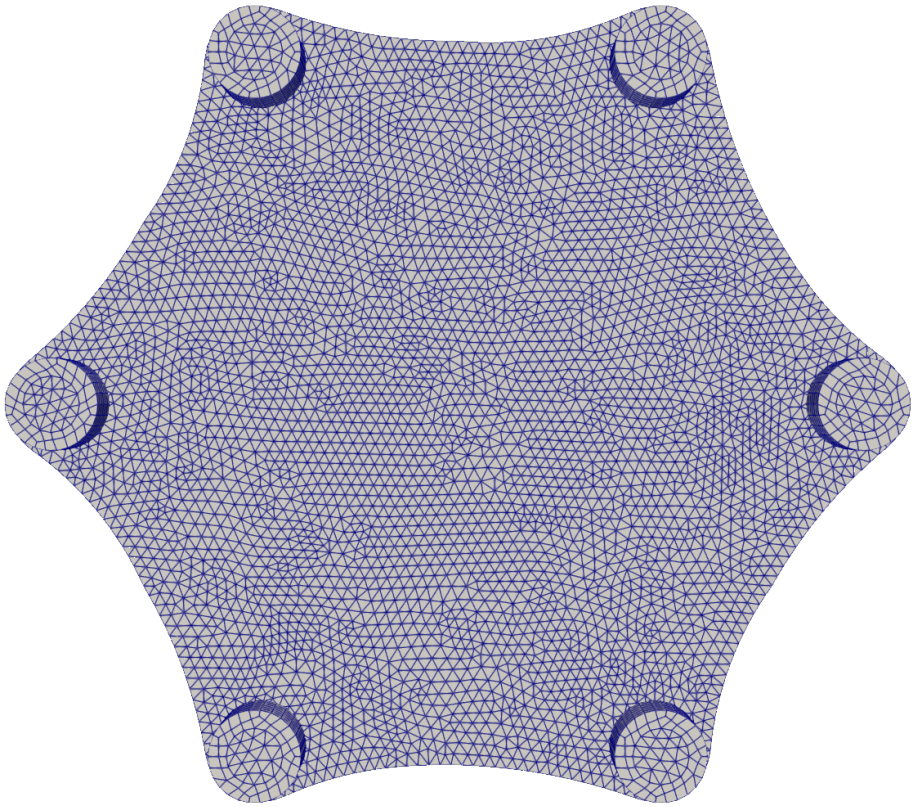

Figure C.8: FEM mesh back view

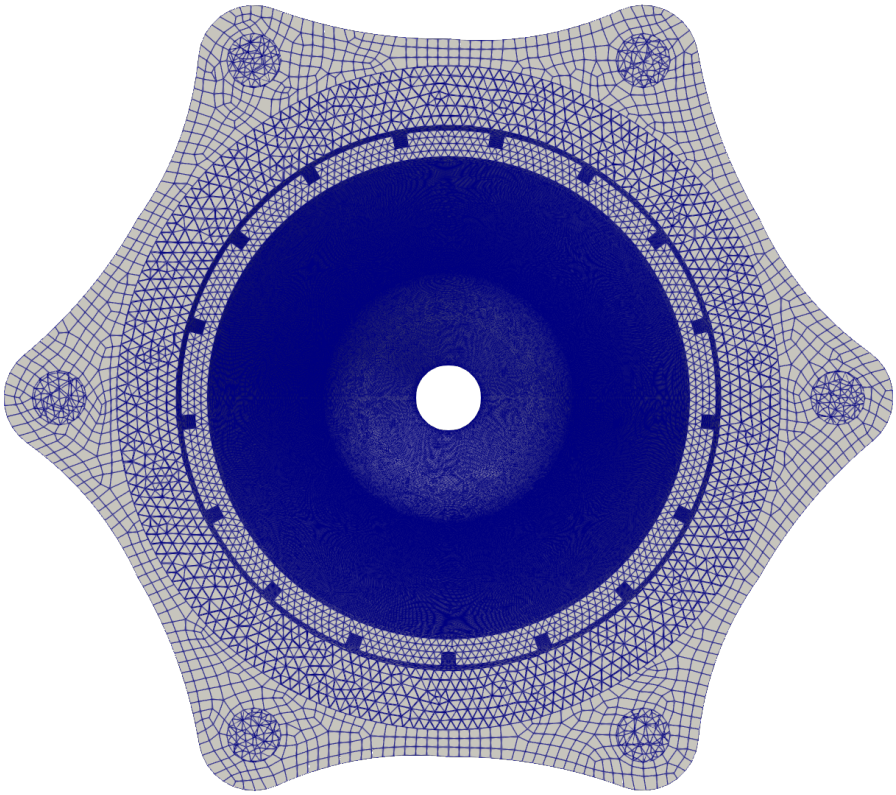

Figure C.9: FEM mesh back view excluding flange

D
Verification Control Matrix (VCM)

In the verification control matrix the requirements will be once again stated, however in this table it will also include the testing method (test, analysis, inspection, or review of design) and the equipment level (equipment, component, system, project). It should be noted that this is a preliminary table, and during the verification campaign this table could be changed or appended based on the testing results.

Table D.1: Verification Control Document (VCD) Matrix.
Methods: T=Test, A=Analysis, I=Inspection, ROD=Review of Design.

Req. ID	Requirement Description	Method	Level
Stakeholder Requirements			
[HL-1]	The thruster shall allow testing for more than one; fuel, injector, and igniter type	T	Sys
[HL-2]	The thruster shall be designed to allow heat load measurement at the chamber at different axial directions	ROD	Sys
[HL-3]	The thruster shall have a minimum impulse bit (MIB) of 250 ms	T	Sys
[HL-4]	As a goal, the thruster may be designed to sustain steady-state firing	T	Sys
[HL-5]	The thruster shall use nitrous-oxide as the oxidizer	I	Sys
[HL-6]	The thruster shall be used in bi-propellant configuration	I	Sys
[HL-7]	The thruster shall be manufactured within the allocated budget	A	Proj
[HL-8]	The thruster shall be optimized for firing in atmospheric conditions	A	Sys
[HL-9]	The thruster shall not exceed a thrust of 25 N	T	Sys
Interface Requirements			
[3.2.2-1]	The thruster shall have propellant connections compatible with 1/8" NPT fittings	I	Eq
[3.2.2-2]	The thruster shall include eight thermocouples and pressure sensor ports at the thrust chamber, manifold and both propellant valve interfaces	I	Eq
[3.2.2-3]	The thruster assembly shall mechanically interface with the thrust plate	I/ROD	Eq
[3.2.2-4]	All measurement equipment used for acceptance testing (pressure, temperature, thrust, mass flow) shall be calibrated	ROD	GSE
[3.2.2-5]	All test tolerances values shall be according to the guidelines from the ECSS-E-10-03A standard	A/ROD	Proj
[3.2.2-6]	The combustion chamber shall accommodate a high-frequency pressure transducer	T	Eq
Thrust Chamber - Functional Requirements			
[3.3.1-1]	The combustion chamber inner wall shall withstand a temperature of maximum 1100 K	T/A	Eq
[3.3.1-2]	The engine shall be designed in such a way so that the temperature will not exceed 900 K during steady-state operations	T/A	Eq

Continued on next page...

Req. ID	Requirement Description	Method	Level
[3.3.1-3]	The thrust chamber material shall be compatible with nitrous-oxide, ethane, propylene, propane, ethylene, and methane	A	Comp
[3.3.1-4]	The thrust chamber material shall not be reactive with a catalyst for nitrous-oxide decomposition	A	Comp
[3.3.1-5]	The thruster shall be fired for 60 seconds or longer at least once without failure	T	Sys
[3.3.1-6]	The thruster shall deliver a total impulse across its lifetime of at least 20 000 N s	T	Sys
[3.3.1-7]	The thruster shall be fired at least 10000 times across its lifetime	T	Sys
Thrust Chamber - Performance Requirements			
[3.3.2-1]	The combustion chamber MEOP shall be 7.5 ± 0.5 bar	T	Eq
[3.3.2-2]	The thruster shall have a specific impulse at sea-level of at least 170 ± 5 s	T	Eq
[3.3.2-3]	Steady state thrust (or chamber pressure) oscillations shall not exceed more than 5% (3% as a goal) of the local average thrust (or chamber pressure) at all frequencies at the trim point	T	Eq
[3.3.2-4]	For the whole pressure box, the steady state thrust (or chamber pressure) oscillations shall not exceed more than 12% at all frequencies	T	Eq
[3.3.2-5]	The thrust shall be 20 ± 1 N at sea-level conditions	T	Eq
[3.3.2-6]	The thrust chamber shall be designed such that the combustion gases expand into atmospheric pressure (101 325 Pa)	A	Eq
Thrust Chamber - Structural Requirements			
[3.3.3-1]	The thrust chamber shall meet the requirements of this document after being subjected to a proof pressure of 1.5 times the maximum expected operating pressure (MEOP)	T	Eq
[3.3.3-2]	The thrust chamber shall withstand a pressure of 2.5xMEOP without rupture	T/A	Eq
[3.3.3-3]	The thrust chamber shall be manufacturable by means of additive manufacturing methods	ROD	Comp
[3.3.3-4]	The combustion chamber contraction ratio shall be in the range 1:4 to 1:11	I	Eq
[3.3.3-5]	The thrust chamber shall have a non-permanent interface connection with the injector plate	I	Eq
[3.3.3-6]	The maximum hoop stress in the thrust chamber shall be less than half of the yield strength of the thrust chamber material at the location of maximum wall temperature	A	Comp
[3.3.3-7]	The thrust chamber shall not exceed the maximum amount of cycles specified by the material supplier corresponding to the maximum wall stress	A	Comp
[3.3.3-8]	The thrust chamber roughness inside the cooling channels shall be less than 20 µm	I	Comp
Injector - Functional Requirements			
[3.4.1-1]	The injector material shall be compatible with nitrous-oxide (N2O)	A	Comp
[3.4.1-2]	The injector material shall be compatible with various hydrocarbons (C2H6, CH4, C3H8, C2H4 and C3H6)	A	Comp
[3.4.1-3]	The external leak rate (before and after operation) shall not exceed 1×10^{-6} scc s^{-1} with the propellant equipment pressurised at MEOP1 with Helium	T	Comp

Continued on next page...

Req. ID	Requirement Description	Method	Level
[3.4.1-4]	The manifold/injector shall either have an M10 or M8 female thread to house a glow plug or a 1/4x32 thread to house a spark plug	I	Comp
Injector - Performance Requirements			
[3.4.2-1]	The injector shall allow for an oxidizer mass flow rate of $0.01042\,kg\,s^{-1}$	T	Eq
[3.4.2-2]	The injector shall allow for a fuel mass flow rate of $0.00116\,kg\,s^{-1}$	T	Eq
[3.4.2-3]	The injector shall allow for a minimum pressure drop of 1 ± 0.5 bar	T	Eq
[3.4.2-4]	The igniter shall demonstrate repeatable ignition over the defined operating envelope, with a minimum ignition success rate to be agreed for acceptance testing	T	Eq
Injector - Structural Requirements			
[3.4.3-1]	The material of the injector shall stay below a temperature of 1000 K	A/T	Comp
[3.4.3-2]	The injector shall be manufacturable using conventional machining methods or additive manufacturing	ROD	Comp
[3.4.3-3]	The injector shall interface with the injector manifold	I	Comp
Igniter - Functional Requirements			
[3.5.1-1]	The igniter shall cause auto-ignition of the two propellants when initiated at operational pressure and temperature	T	Eq
[3.5.1-2]	The igniter shall not cause decomposition and ignition of the propellants in their separate injector zones	T	Eq
[3.5.1-3]	The external leak rate (before and after operation) shall not exceed $1 \times 10^{-6}\,scc\,s^{-1}$ with the propellant equipment pressurised at MEOP1 with Helium	T	Comp
Igniter - Performance Requirements			
[3.5.2-1]	The igniter shall heat up to a temperature of at least 1200 K	T	Comp
[3.5.2-2]	The igniter shall have a thread compatible with the injector/manifold	I	Comp
[3.5.2-3]	The diameter of the igniter tip (heating element) shall not be more than 5.5 mm	I	Comp
Igniter - Structural Requirements			
[3.5.3-1]	The igniter body shall stay below its melting temperature	A	Comp
Valves - Functional Requirements			
[3.6.1-1]	The external leak rate (before and after operation) shall not exceed $1 \times 10^{-6}\,scc\,s^{-1}$ with the propellant equipment pressurized at MEOP1 with Helium	T	Comp
[3.6.1-2]	The internal leak rate (before and after operation) shall not exceed $1 \times 10^{-4}\,scc\,s^{-1}$ with the propellant equipment pressurized at MEOP1 with Helium	T	Comp
[3.6.1-3]	The proof pressure (1.5xMEOP) shall be sustained for a min. period of time of 5 minutes	T	Comp
[3.6.1-4]	The burst pressure (4xMEOP) shall be sustained for a min. period of time of 1 minute	T/A	Comp
[3.6.1-5]	The valve shall either open or close within 15 ms	T	Comp
Valves - Performance Requirements			

Continued on next page...

Req. ID	Requirement Description	Method	Level
[3.6.2-1]	The ethane valve shall allow for a mass flow of $0.001\,16\,\mathrm{kg\,s^{-1}}$	T	Comp
[3.6.2-2]	The nitrous oxide valve shall allow for a mass flow of $0.010\,42\,\mathrm{kg\,s^{-1}}$	T	Comp
[3.6.2-3]	The pressure drop of the valve at a mass flow rate of $0.010\,42\,\mathrm{kg\,s^{-1}}$ of nitrous oxide shall not exceed 0.5 bar	T/A	Comp